Wesleyan University

Searching for Exoplanets Around the Brightest Stars in K2

by

Ismael Mireles
Class of 2019

A thesis submitted to the
faculty of Wesleyan University
in partial fulfillment of the requirements for the
Degree of Master of Arts

Middletown, Connecticut April, 2019

Contents

Chapter 1

Introduction

The field of exoplanet research is a relatively new one, but the existence of planets orbiting other stars has been speculated for centuries. After Nicolaus Copernicus formulated his heliocentric model and removed Earth from a special place in the center of the universe, many began to speculate about the possibility of planets orbiting other stars. One such person was Giordano Bruno, a Dominican friar and philosopher (Aquilecchia 2019). Bruno expanded the heliocentric model and applied to other stars, arguing in favor of the existence of countless Earths orbiting other stars in the sky. For this and other reasons, Bruno was tried for heresy by the Catholic Church and burned at the stake in 1600.

It would take centuries before the first exoplanet would be detected. The radial velocity method (see Sec. 1.1.1) was proposed as a potential technique to detect exoplanets Struve (1952). A few years later, van de Kamp (1963) claimed to have detected multiple Jupiter mass planets orbiting Barnard's star using the astrometry method (see Sec. 1.1.3). Other astronomers were unable to verify this claim (Gatewood, & Eichhorn 1973), but Van de Kamp continued to claim their existence. While it is now thought that this erroneous claim was due to instrumental artifacts, there is now evidence that a planet is orbiting the star (Ribas et al. 2018). This planet is much smaller and closer in than those Van de Kamp thought existed.

The first scientific evidence of an exoplanet was obtained in 1988 with radial velocity measurements of the binary star γ Cephei (Campbell et al. 1988). The authors inferred a mass between 1 and 9 Jupiter masses, but were hesistant to claim a detection due to the quality of the data. Later observations of the system would confirm the presence of a planet (Hatzes et al. 2003).

The first confirmed detection of an exoplanet came in 1992 when Aleksander Wolszczan and Dale Frail detected multiple planets around the pulsar PSR1257+12 (Wolszczan, & Frail 1992). A pulsar is a rapidly rotating neutron star that pulsates regularly. By measuring the changes in timing of pulsations, the astronomers were able to infer the presence of 3 planets orbiting the pulsar.

In less than 30 years since the first detection, almost 4,000 additional exoplanets have been detected, according to NASA's Exoplanet Archive (Akeson et al. 2013). These planets range in radii from smaller than Mercury (Barclay et al. 2013) to larger than Jupiter (Hartman et al. 2011). They can be found closer in than Mercury and further out than Neptune. They have been detected through a variety of techniques, some of which are discussed in the next section.

1.1 Detection Techniques

1.1.1 Radial Velocity

The first exoplanet around a main-sequence star, 51 Pegasi b, was detected using a technique known as the radial velocity (RV) method, or Doppler spectroscopy (Mayor, & Queloz 1995). This technique detects planets by measuring the gravitational pull they exert on their host stars. The planet and star orbit around their common center of mass with the same orbital period. This movement of the star can be detected by measuring the Doppler shift in spectral lines.

When the star is moving towards the observer, the lines are blueshifted and when it is moving away, they are redshifted. The magnitude of the shift is determined by the radial velocity of the star and is given by the equation

$$\frac{\Delta\,\lambda}{\lambda_0} = \frac{v}{c},$$

where $\Delta\,\lambda$ is the shift of a spectral line, λ_0 is the rest wavelength of the line, v is the radial velocity of the star, and c is the speed of light.

By taking multiple observations, we can see how velocity changes over time and from this, derive orbital and planetary parameters including the orbital period, eccentricity, and lower limit on the planet's mass. The radial velocity curve for 51 Pegasi b is shown in Figure 1.1. From the shape alone, some information is revealed. A planet in a perfectly circular orbit would result in a sinusoidal radial velocity curve. The symmetry in the radial velocity curve of 51 Peg b indicates that the eccentricity is very low. The amplitude of the curve also reveals information about the mass.

An important measured value is the radial velocity semi-amplitude, which is given by

$$K = \sqrt{\frac{G}{1-e^2}}\, m_2\, sin\, i\, (m_1 + m_2)^{-1/2}\, a^{-1/2},$$

where G is the gravitational constant, e is eccentricity, m_2 is the secondary or planetary mass, m_1 is the primary or stellar mass, i is the orbital inclination, and a is the semi-major axis of the orbit. The semi-major axis can be obtained by using the orbital period P and Kepler's third law. An important thing to note is that this method gives you the lower bound of planet's mass ($m_2\, sin\, i$) and

not the true mass due to the difficulty in determining the inclination through RV measurements alone.

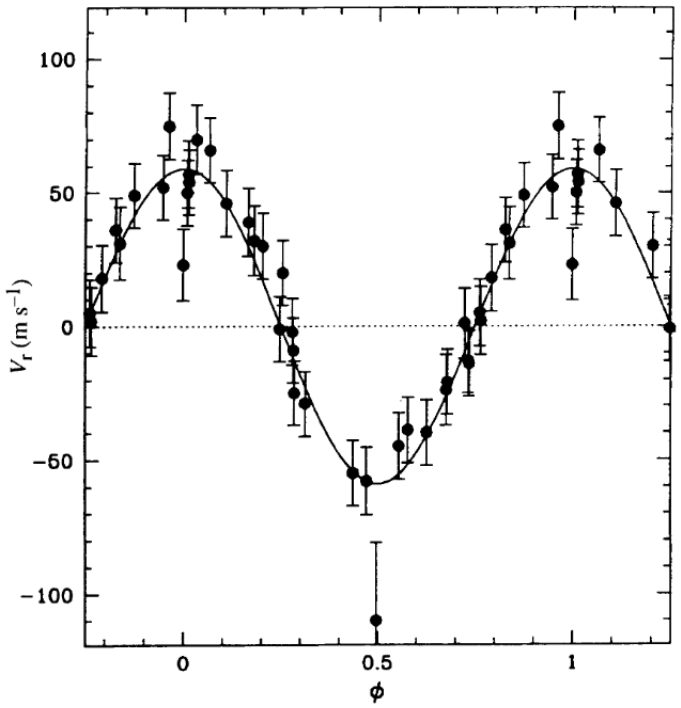

Figure 1.1: Radial velocity curve for 51 Pegasi b, from Mayor, & Queloz (1995).

This technique suffers from several biases and limitations. This method favors massive, close-in planets in order to maximize the signal and data obtained, as the equation for the semi-amplitude demonstrates. It also disfavors massive early-type stars due to the increased stellar mass weakening the signal and also the relative scarcity of absorption lines in their spectra. On the other hand, M dwarfs are also less optimal targets due the fact that they are intrinsically fainter than other stars, which decreases the ratio of the signal to noise, or SNR. They also have an increased jitter due to increased stellar activity.

This technique, like most others, favors brighter stars as the signal-to-noise

ratio generally increases as magnitude decreases (Plavchan et al. 2015; Carleo et al. 2016).

1.1.2 Transit

For years the radial velocity method was the most successful technique for detecting planets (Figure 1.2). With the launch of dedicated survey missions such as *CoRoT* (Convection, Rotation and planetary Transits) and *Kepler*, the transit method would become the most successful detection technique. The first exoplanet to have been observed transiting its host star is HD 209458b, which was first detected using the radial velocity method (Charbonneau et al. 2000).

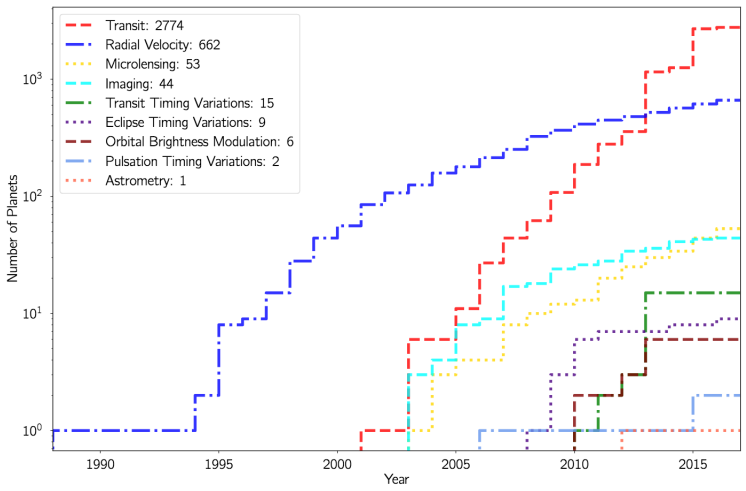

Figure 1.2: Cumulative number of exoplanets detected over time, by technique used. The radial velocity method had the most planets detected until 2012 when it was surpassed by the transit method. From Niraula (2018).

This technique works by measuring changes in the brightness, or flux, of a star as a planet crosses between us and the star (Figure 1.3). The amount of light blocked by the planet is simply the ratio of its area to the star's, or

$$\delta = \left(\frac{R_p}{R_\star}\right)^2$$

The transit method reveals the size of the planet relative to star. If the stellar radius is known, then it gives the physical size of the planet. A more detailed discussion about the transit method can be found in Chapter 4. Multiple transit detection survey missions have searched and will search for planets. Three such missions are discussed next: *CoRoT*, *Kepler* (and *K2*), and *TESS*.

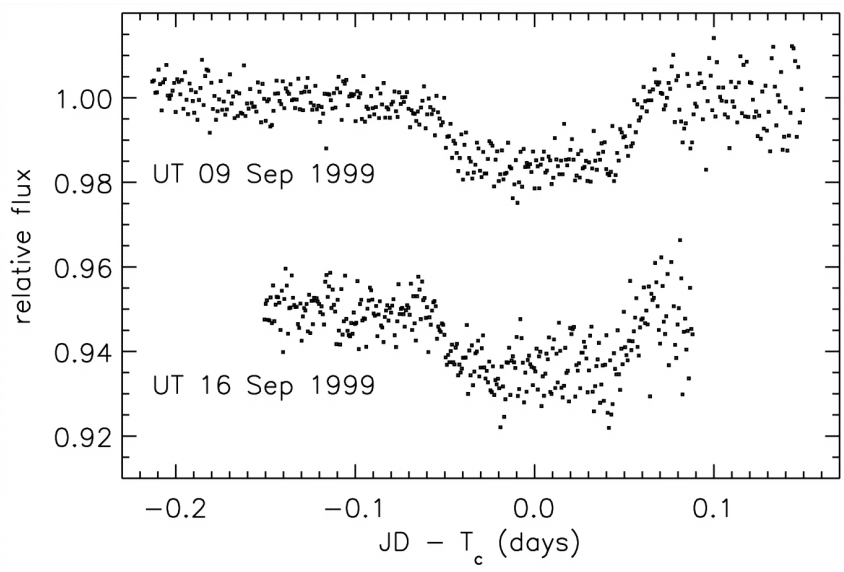

Figure 1.3: Two transit events of the HD 209458b, from Charbonneau et al. (2000)

CoRoT

The *CoRoT*, or *Convection, Rotation and planetary Transits*, mission was launched in 2006 to search for short period exoplanets (Auvergne et al. 2009). The first spacecraft dedicated largely to search for transiting planets, it led to the detection of 30 exoplanets (Moutou et al. 2013). Among the planets detected is CoRoT-7b, the first rocky exoplanet to have its radius determined (Léger et al. 2009). It has a radius of 1.58 $R_\oplus$ and orbits its parent star every 20.5 hour. It is similar to Mercury in that it has a high dayside temperature and very low nightside temperature Léger et al. (2011), and is thought to have a very thin atmosphere, if any at all.

Kepler/K2

NASA's *Kepler* mission was launched in 2009 to observe one region of the sky in search of Earth-like exoplanets around Sun-like stars. In 2012, two reaction wheels failed, bringing the mission to an end. Scientists were able to repurpose the telescope as the *K2* mission, which observed fields along the ecliptic for over 6 years until it ran out of fuel. Together, *Kepler* and *K2* have detected nearly 2500 exoplanets. A more detailed discussion of these missions can be found in Chapter 2.

TESS

NASA's *TESS*, or *Transiting Exoplanet Survey Satellite*, is a successor to the *Kepler*/*K2* missions. Launched in April 2018 and beginning science observations a few months after, it plans to observe 500,000 stars in search of planets (Ricker et al. 2014). Whereas *Kepler* was focused on finding Earth-Sun analogs, *TESS* is

focused on surveying the brightest and nearest stars. Unlike *K2*, it will completely avoid the ecliptic, instead observing the rest of the sky in sectors (Figure 1.4). The first detections have already been made, including the detection of a planet around the bright (V = 5.65) star, π Mensae (Gandolfi et al. 2018). While a 10 Jupiter mass planet had been previously detected using the radial velocity method, this new planet is 4 Earth masses and has a 6.26 day orbital period. Its discovery makes π Mensae the brightest star with a transiting exoplanet, slightly brighter than the previous brightest star 55 Cnc (Winn et al. 2011).

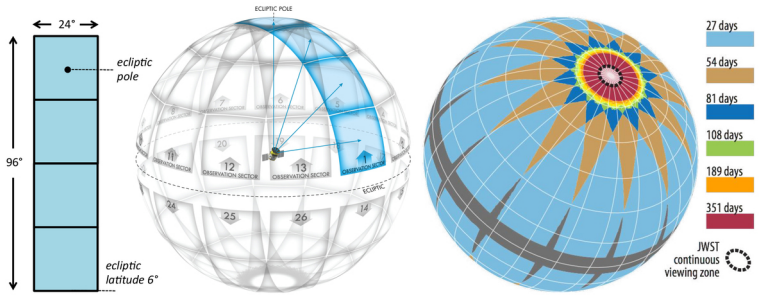

Figure 1.4: *TESS* observation sectors. Sectors overlap at different points, with the ecliptic poles having continuous coverage for 351 days. From `https://en.wikipedia.org/wiki/Transiting_Exoplanet_Survey_Satellite`

1.1.3 Astrometry and Direct Imaging

Another technique that has been used to search for exoplanets is astrometry, as used by Peter Van de Kamp on Barnard's star in 1963. Conceptually, it is a similar concept to the radial velocity method as it seeks to detect a star's change in position in the sky due to the planet orbiting around it. Instead of measuring shifts in spectral features, it measures deviations in the star's position in sky. The deviation, θ is given by

$$\theta = \frac{m_2}{m_1} \frac{1+e}{d} \left(\frac{G\, m_1\, P^2}{4\,\pi} \right)^{1/3},$$

where m_2 is the planet's mass, m_1 is the star's mass, e is the eccentricity, d is the physical distance to the star, and P is the orbital period. Although no planet has yet been discovered using this technique, the *Gaia* mission is predicted to be able to detect multiple planets. This method is biased towards massive distant planets unlike the radial velocity and transit techniques which are biased towards massive close-in planets. It is better-suited for bright stars, as astrometric precision decreases as stars become fainter (Gaia Collaboration et al. 2016).

Unlike astrometry, direct imaging has been successfully used to detect planets. This technique works by blocking out the central star and looking for faint sources of light surrounding the star. It is most effective when observing in the infrared, where planets are brightest. One of the earliest detections was made around HR 8799, a young star found to have 3 Jupiter size planets orbiting around it (Marois et al. 2008). This technique is biased towards young massive distant planets they have to be far enough from their host stars to not be blocked out by the coronagraph or residual starlight (Figure 1.5). They also must be young enough to still be contracting and emitting enough energy to be detected. For a given system, the brighter the host star is, the brighter the planet will be, making it easier to make out from the background.

There are more detection methods being used to search for exoplanets that are not discussed here, including microlensing, polarimetry, and various timing variation methods.

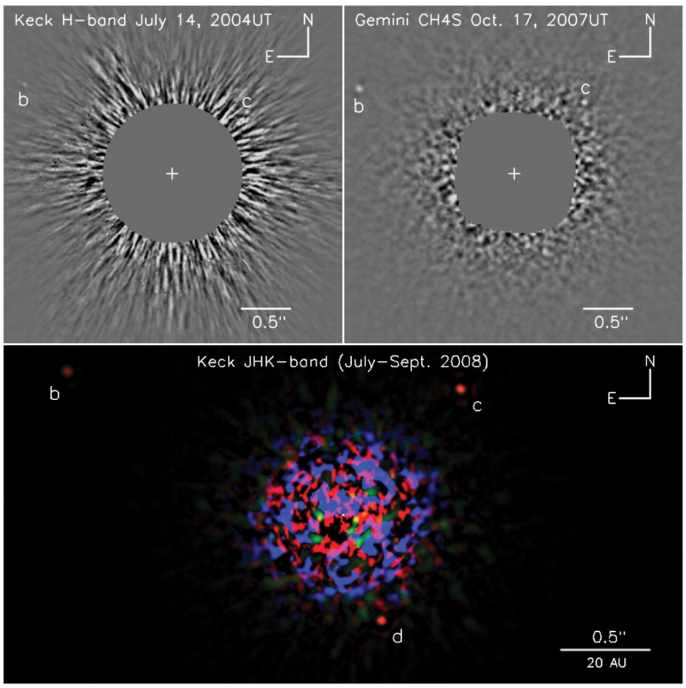

Figure 1.5: Keck and Gemini observations of HR 8799. The three planets appear as small dots.

1.2 Exoplanet Characterization

Once detected, follow-up observations can be made to further study an exoplanet. The radial velocity method can be used in tandem with the transit method to determine the bulk density. The former provides $m \sin i$, while the latter provides i and the planet radius.

It is also possible to learn about the spin-orbit alignment of a planetary system through the study of the Rossiter-McLaughlin effect. When a planet transits its host star, it will block different regions of the star (Gaudi, & Winn 2007). When we consider that the star is rotating and different regions of the star will have different radial velocities, this means different velocities will be obscured by the planet as it transits, resulting in an effective velocity shift of the spectral line

observed. By determining which velocities are obscured when, it is possible to determine the spin-orbit alignment (Figure 1.6). The orbits of hot Jupiters are often misaligned with the spin of their host stars, and can even be retrograde (Albrecht et al. 2012).

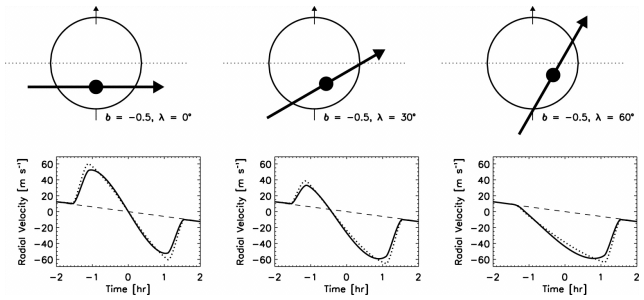

Figure 1.6: Schematic of the Rossiter-McLaughlin effect, from Gaudi, & Winn (2007)

Using the transit method, it is possible to study the composition and structure of an exoplanet atmosphere in a technique known as transit spectroscopy. This technique measures how the apparent size of the planet changes with wavelength, as different components of the atmosphere absorb and scatter starlight (Figure 1.7). The first detection of an exoplanetary atmosphere was made when Charbonneau et al. (2002) detected sodium in the atmosphere of HD 209458b. Many interesting discoveries have been made since then, including the detection of escaping atmospheres (Vidal-Madjar et al. 2003; Linsky et al. 2010; Jensen et al. 2012), water and methane in atmospheres (Tinetti et al. 2007; Swain et al. 2008), and clouds (Kreidberg et al. 2014). For large, very close-in planets, it is also possible to detect the starlight reflected by the dayside region of a planet, revealing information about atmospheric structure and circulation (Charbonneau et al. 2005).

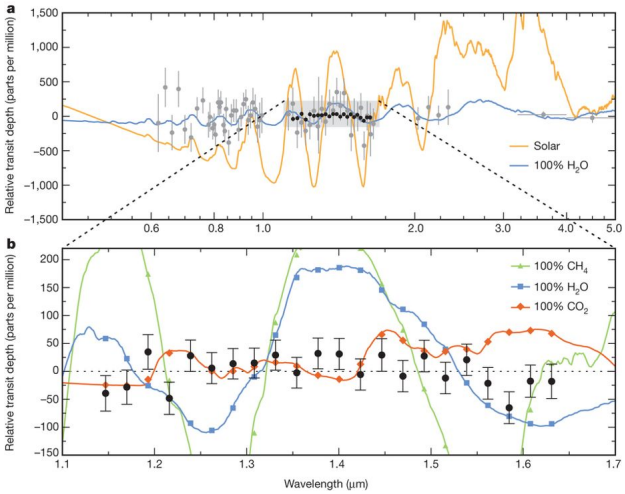

Figure 1.7: Transmission spectrum of the super-Earth GJ 1214b, from Kreidberg et al. (2014). The flat nature of the spectrum is thought to be indicative of clouds.

1.2.1 Bright Stars

Bright stars are best suited for follow-up due to inherently larger signal to noise ratios. Metrics developed to prioritize exoplanets for follow-up all favor brighter stars. Two such metrics are introduced by Kempton et al. (2018) for both transmission spectroscopy and emission spectroscopy. For the former, the metric has the form

$$TSM \sim \frac{R_p^3 \, T_{eq}}{M_p \, R_\star^2} \times 10^{-m_J/5},$$

where R_p and M_p are planet radius and mass, T_{eq} is the equilibrium temperature of the planet, $R_\star$ is the stellar radius, and m_J is the apparent stellar magnitude in J band.

For emission spectroscopy, the metric has the form

$$ESM = 4.29 \times 10^6 \times \frac{B_{7.5}(T_{day})}{B_{7.5}(T_\star)} \times \left(\frac{R_p}{R_\star}\right)^2 \times 10^{-m_K/5},$$

where $B_{7.5}(T_{day})$ is the Planck function evaluated at 7.5 microns and the dayside temperature of the planet (T_{day}), $B_{7.5}(T_\star)$ is the Planck function evaluated at the stellar effective temperature, and m_K is the apparent stellar magnitude in K band.

We look at approximately 1000 of the brightest stars observed by the *K2* mission in order to search for any transiting exoplanets orbiting around them. While they are ideal for follow-up, there are multiple challenges when it comes to analyzing these targets as observed by *K2*. Two of the most significant ones are pixel saturation and bleeding as well as contamination from field stars. A more in-depth discussion can be found in Chapter 4.

Chapter 2

Observations

2.1 Kepler

Launched in March 2009, the *Kepler* mission sought to detect Earth-sized exoplanets in the habitable zones of Sun-like stars (Huber et al. 2014) over a period of 3.5 years with precision up to 10 ppm (Borucki et al. 2010). It was placed into orbit around the Sun instead of the Earth in an Earth-trailing orbit. Its primary mirror is 1.4 meters in diameter and it uses 21 CCD modules, each covering ~ 5 deg^2 of the sky. The Kepler bandpass is wider than typical photometric filters, spanning a range from 400 to 900 nm. Its field of view (FOV) allowed it to observe over 150,000 mostly Sun-like and smaller stars (Figure 2.1), while its four reaction wheels allowed it to stay pointed at the same region of the sky for the entire mission (Figure 2.2). *Kepler* pointed at a region of space above the galactic plane near the Cygnus and Lyra constellations, with the region being chosen to have very few bright stars in order to avoid saturating the detector and causing column bleeding (Koch et al. 2010). Over the nearly 4 years of observations, the mission has led to the detection of over 2300 confirmed exoplanets, per NASA's Exoplanet Archive (Figure 2.3). In terms of planetary statistics, it was determined that 16.5%$\pm$3.6% of FGK stars have at least one planet with radius between 0.8 and 1.25 $R_\oplus$ and orbital period under 85 days (Fressin et al. 2013).

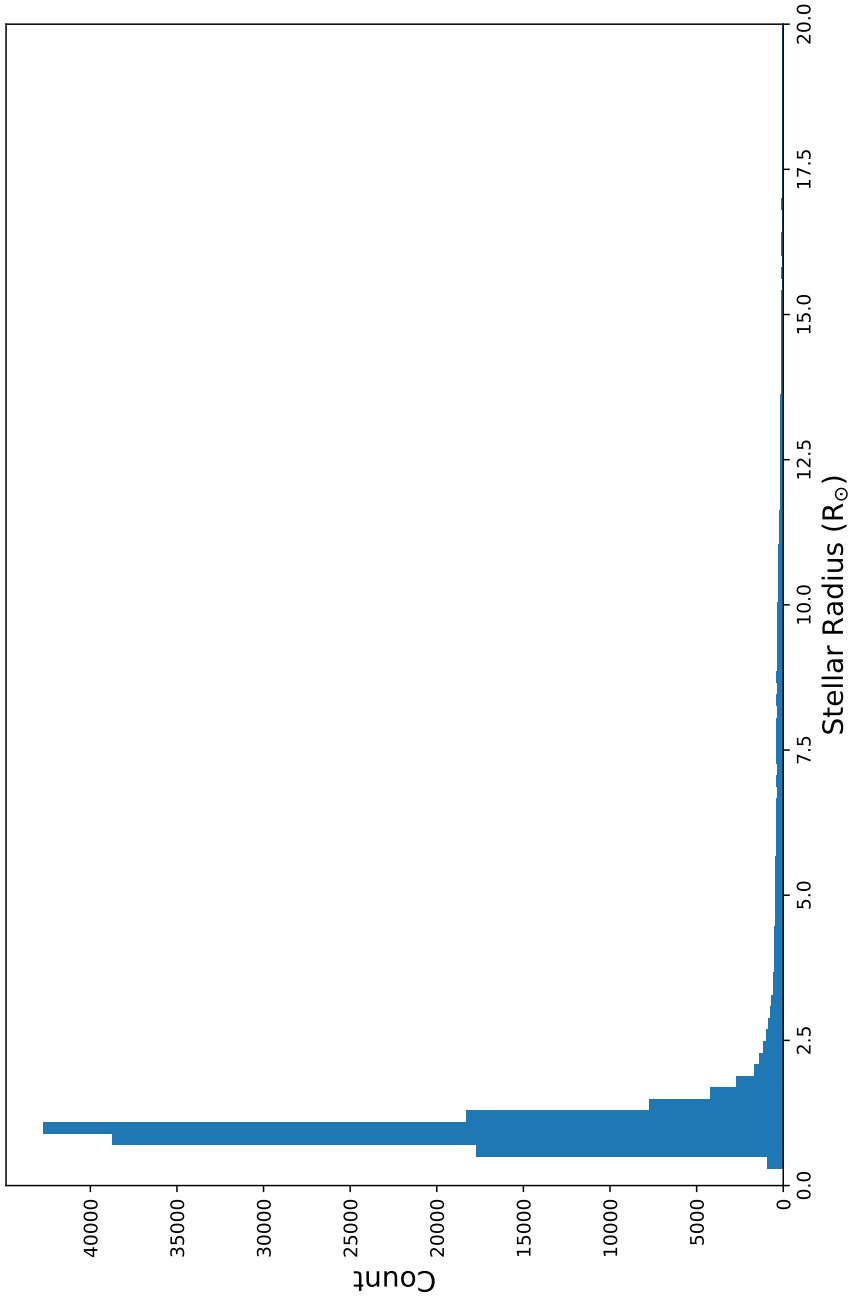

Figure 2.1: Histogram of stellar radii less than 20 $R_{\odot}$ for all targets observed by the original *Kepler* mission. The vast majority of targets are under 2 $R_{\odot}$, ideal for planet searches.

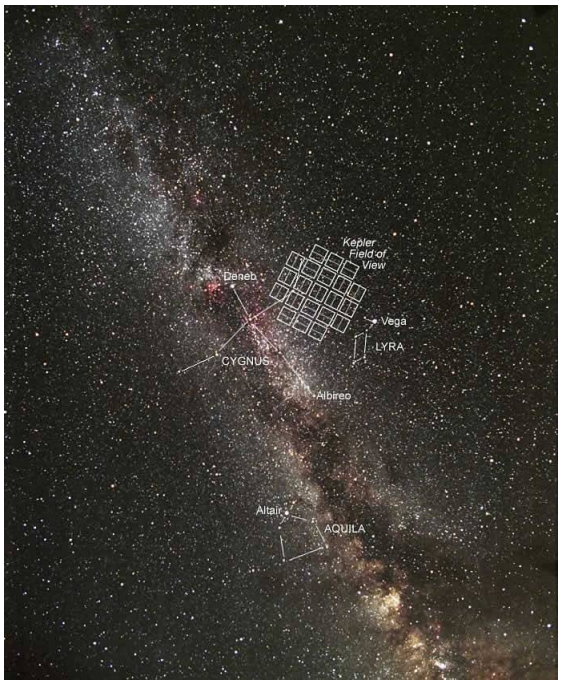

Figure 2.2: Field of view of the original *Kepler* mission. (Source: `https://www.nasa.gov/mission_pages/kepler/multimedia/images/kepler-field-of-view-photo.html`)

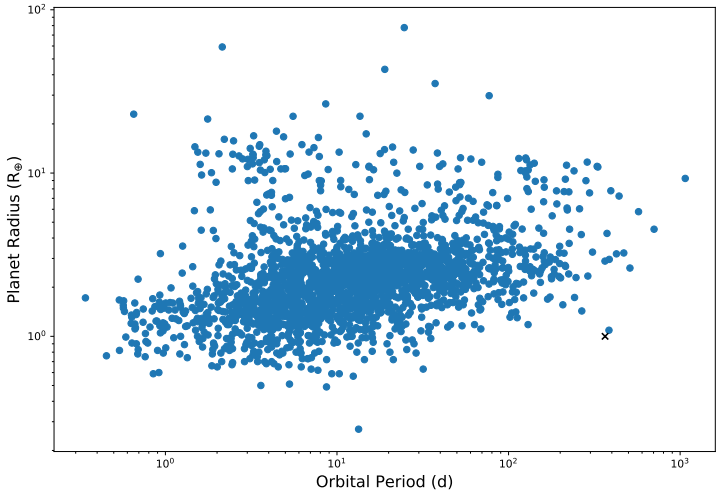

Figure 2.3: Orbital periods and radii of confirmed planet detections made by *Kepler*, with the values for Earth shown as the black ×.

2.2 *K2*

The *Kepler* spacecraft was equipped with 4 reaction wheels that allowed it to stay pointed at a specific region of the sky. In June 2012, one of the reaction wheels failed. The failure of one wheel was not disastrous, as it was designed to still function with three reaction wheels. In May 2013, however, a second reaction wheel failed, putting the future of the mission in jeopardy. *Kepler* would no longer be able to maintain pointing, as it would drift off target. To mitigate this issue, the *Kepler* team devised a plan to use the miniscule pressure exerted by sunlight incident on the spacecraft to help balance it. The spacecraft would drift away from its target, but by a much smaller amount and in a way that it could use its thrusters to reset its position. Thus the *K2* mission was started in June 2014. The use of sunlight to balance the spacecraft meant it could only look at one region for around 80 days before sunlight would start to enter the telescope. These 80 day periods of observing one region were each designated as campaigns and 20 campaigns were planned in total. The regions all lie along the ecliptic plane as a result of the mission setup (Figure 2.4). It has led to the detection of over 1000 candidate and confirmed exoplanets (Figure 2.5) The *K2* mission includes more bright targets than the original *Kepler* mission as it was felt that more liberties could be taken with the repurposed mission (Figure 2.6). Although it was feared that the precision of *K2* would be an order of magnitude worse than *Kepler's*, it was shown that the precision could be brought to within a factor of two of *Kepler's* (Vanderburg, & Johnson 2014).

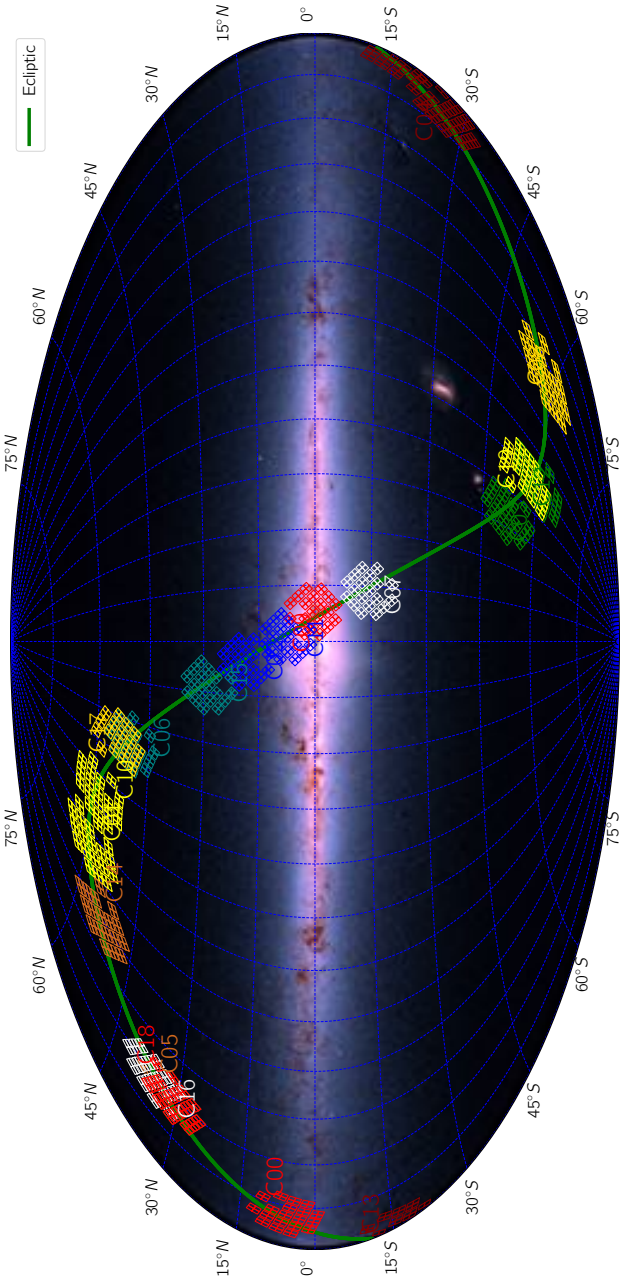

Figure 2.4: Field of view of the various campaigns of the *K2* mission. The green line denotes the ecliptic. Note the overlap between some campaigns. From Niraula (2018).

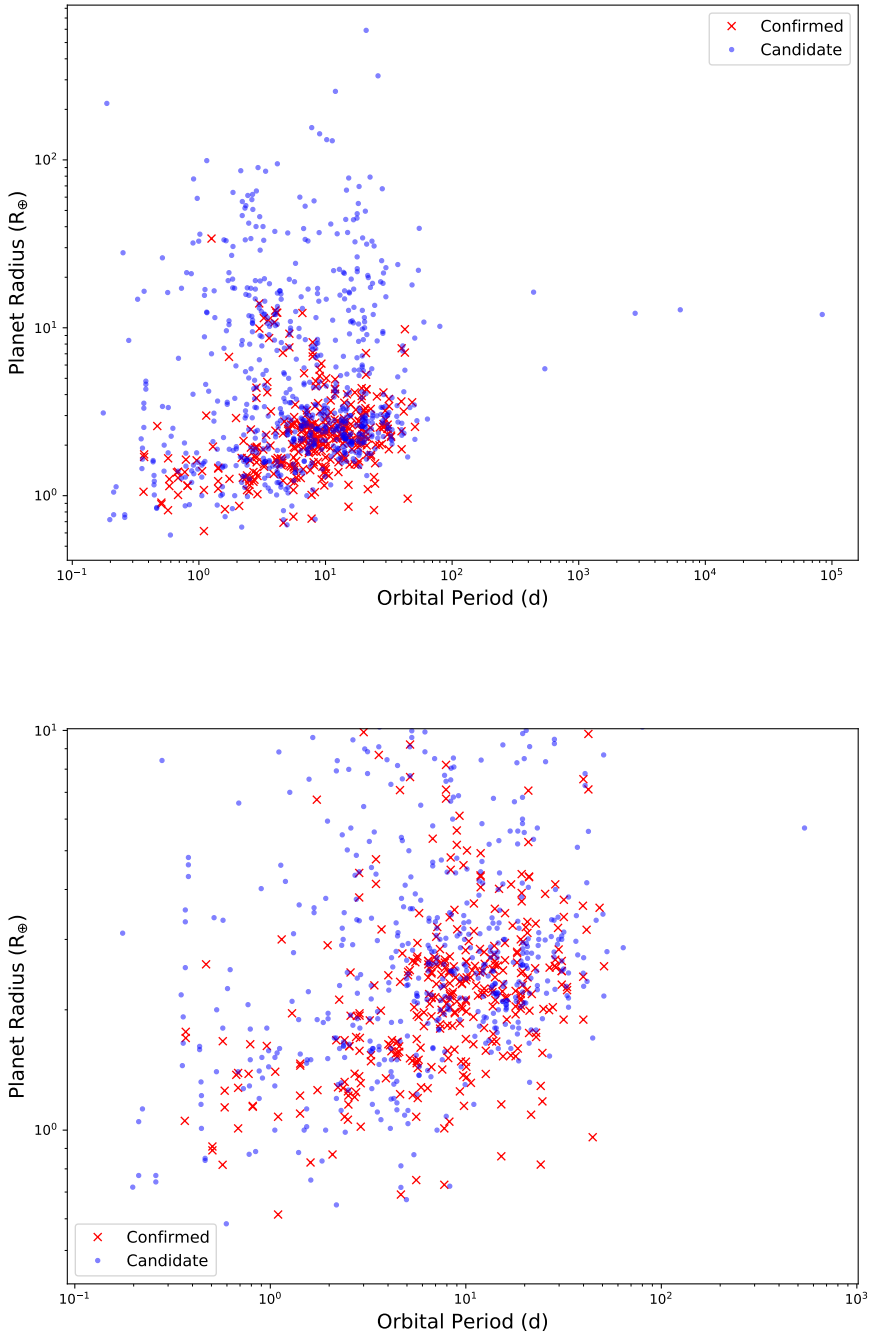

Figure 2.5: Orbital periods and radii of all candidate and confirmed exoplanet detections by *K2* (top) and planets under 10 $R_{\odot}$ (bottom).

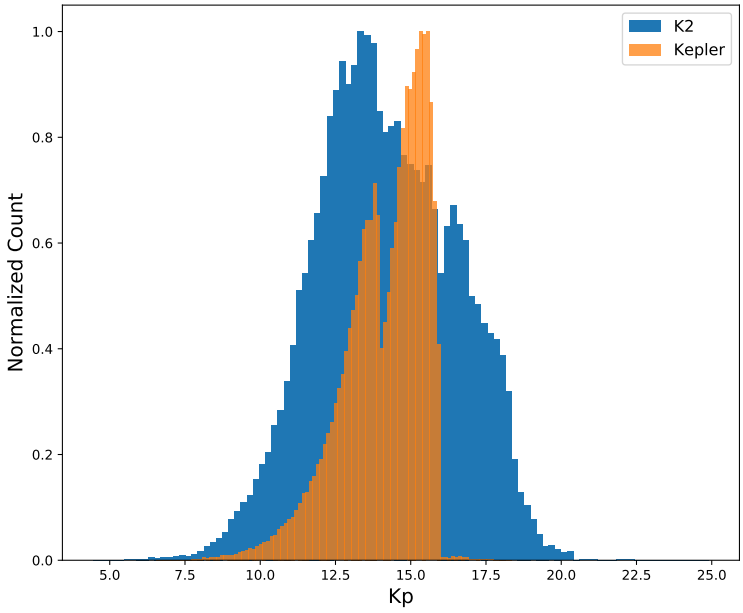

Figure 2.6: Normalized histograms of the Kp values of the targets observed by the *Kepler* and *K2* missions. *K2* targets span a wider range of magnitudes than *Kepler*.

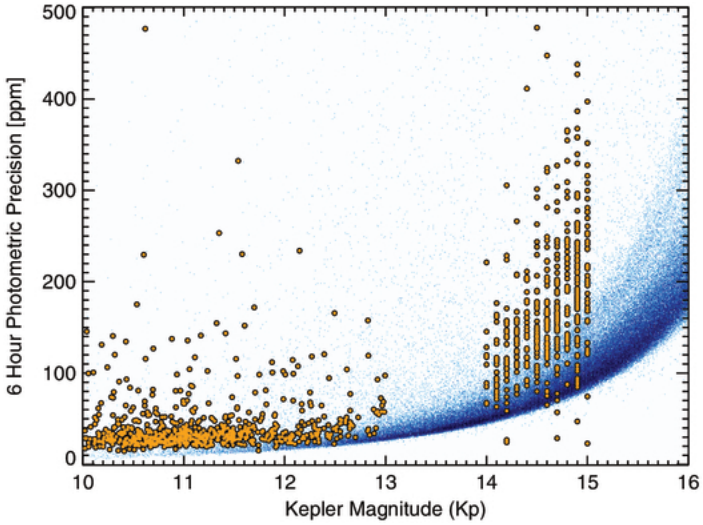

Figure 2.7: 6 hour precision values for *K2* (orange) and *Kepler* targets. From Vanderburg, & Johnson (2014).

2.3 *K2* Data Reduction

2.3.1 Quality Flags

As with any telescope, *K2* has to deal with data quality issues, both from itself and from external sources. These issues include, but are not limited to, cosmic rays striking the detector as well as the spacecraft's thrusters firing while the data is being collected. In their processing of the data, the *K2* team includes quality flags with values that correspond to the issues present in each frame of data. A value of 0 corresponds to no issues while nonzero values correspond to different issues. These include, but are not limited to, a value of 128 for cosmic rays, 256 for manual exclusions, and 1048576 for thruster firing events.

The raw data released before processing does not include quality flags, thus we have to include frames where the data is not optimal. One issue that can be dealt with is when a thruster firing event and rolling bands occur in the same frame. This issue can be detected manually and removed. This is done by taking the sum of each data frame and plotting the sums over time. As demonstrated in Figure 2.8, the outliers are readily apparent as decreases in the total number of counts. This effect is most obvious for bright targets and significantly affects our ability to analyze their raw data. We change the quality values in the FITS files of these outlier frames to nonzero values such that those frames are not used in the reduction process.

The light curves generated from the raw data are useful for identifying interesting targets to focus on when the reduced data are released. However, there are differences between the light curves of the raw and reduced data, as can be seen in Figure 2.9. This can result in false positives where instrumental effects

can be interpreted as transit events, as well as false negatives where real transit events are diluted by instrumental effects. Some interesting Campaign 18 targets identified from the analysis of the raw data are presented and discussed in Sec. 3.4.

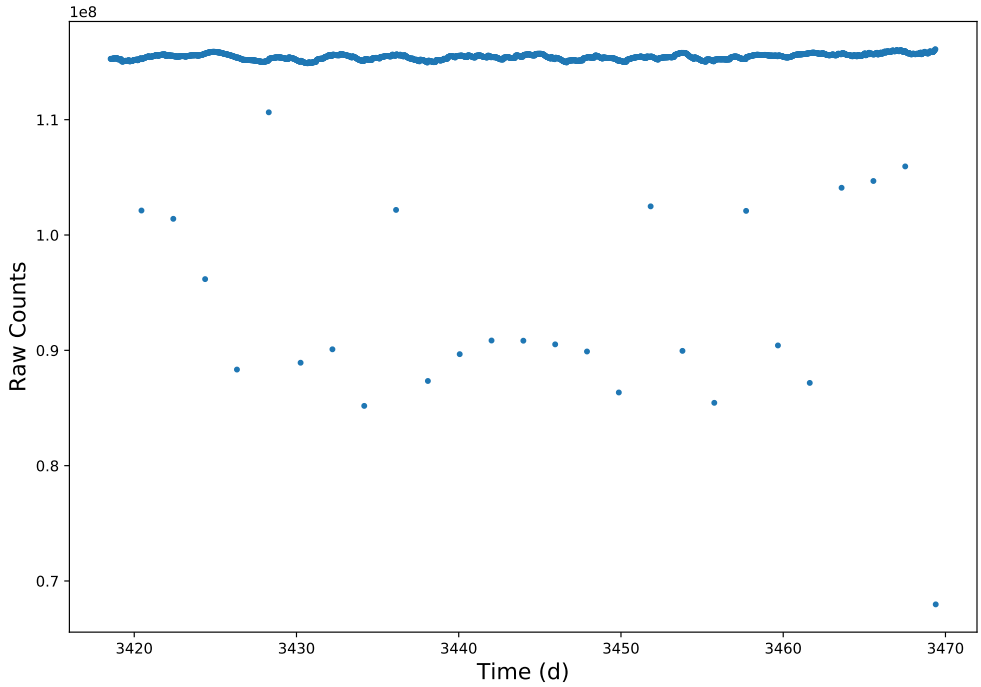

Figure 2.8: Raw sums over time for EPIC 211399051, a bright (Kp = 5.141) target observed in Campaign 18. The large decreases in counts occur when combined thruster and firing band events occur.

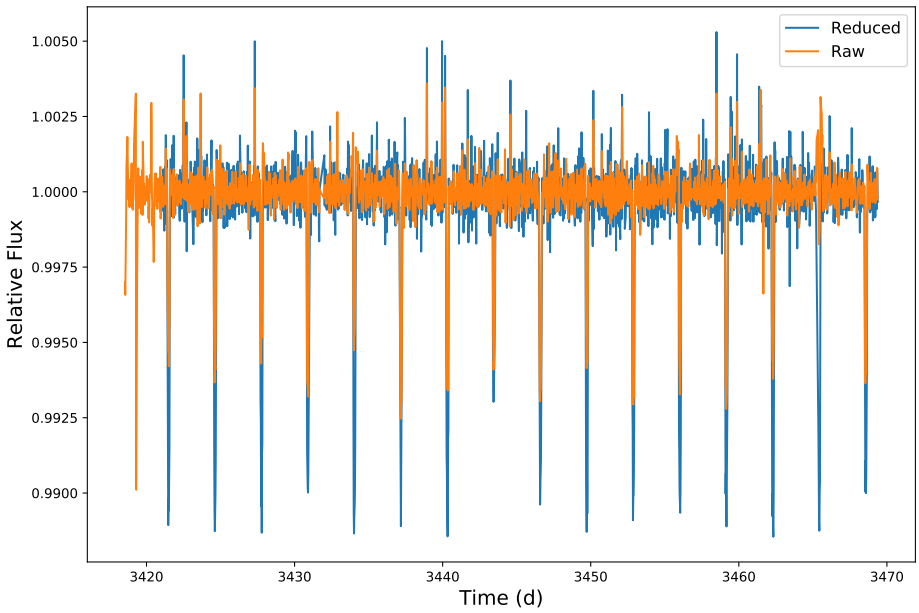

Figure 2.9: Raw and reduced light curves for EPIC 211309648, a target observed in Campaign 18. While the raw data appears to feature less noise out of transit, its depths are smaller than those of the reduced data.

2.3.2 Aperture Selection

K2 returns postage stamps that contain pixels corresponding to the target star as well as pixels corresponding to the sky background and occasionally other nearby stars. In order to best analyze the target star, it is necessary to create apertures that contain only the target star, avoiding neighboring stars and omitting as much background as possible (see Sec. 3.4). There are various ways to choose apertures. The simplest way is to make the aperture a circle centered on the center of the star, having the radius be a function of magnitude. A more robust method for choosing an aperture is to choose pixels whose flux values are above a

predetermined cutoff, for example, 1.05 times the median background value as is used in Van Eylen et al. (2016). Although less rigorous than the aforementioned method, a circular aperture is typically preferred for bright targets (Vanderburg, & Johnson 2014).

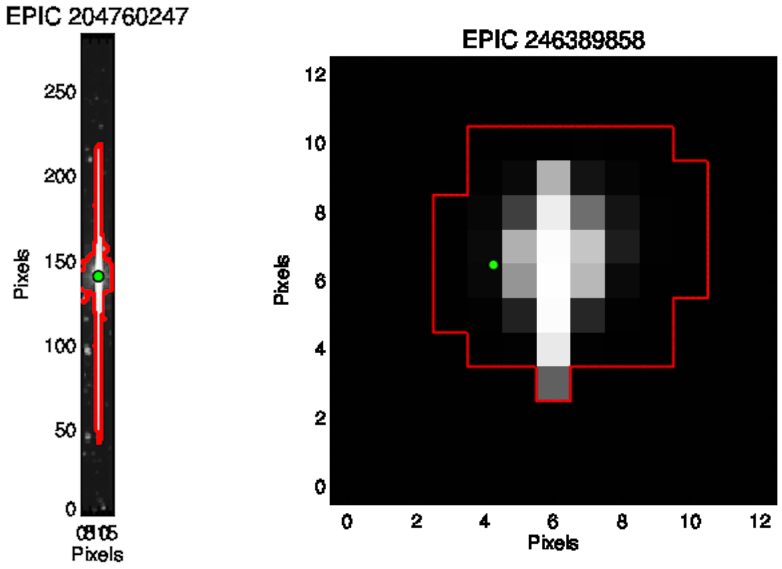

Figure 2.10: Apertures selected by the *K2SFF* reduction pipeline for a Kp = 5.954 (left) and Kp = 10.277 (right) target.

2.3.3 Detrending and Flattening

Perhaps the most significant issue affecting *K2* light curves is the drift of the spacecraft due to the failure of two reaction wheels. This issue manifests itself as a steady increase/decrease in flux over the span of ∼6 hours, followed by thrusters firing to reset the cycle. This signal typically dominates signal from either transiting planets or the star. This signal can be removed in a variety of ways. One method, used by *K2SFF* (Vanderburg, & Johnson 2014), is to model the loss of flux in an aperture as the star drifts across. For stars that do not vary significantly over the time between thruster events, the loss of flux

takes on a functional form that can be modeled and removed. When stars do vary significantly, this technique struggles to detrend the data without removing stellar signal. Another method, developed for *K2photometry* (Van Eylen et al. 2016), models the multi-dimensional dependency of the centroids of the star. Other detrending methods have been developed, but are not discussed.

While the detrending process removes the effects of the spacecraft's drift, it does not remove variability due to other systematics or the star itself. Thus, it is necessary to flatten the light curve before searching for planetary signals. One common flattening technique is a Savitzky-Golay filter, as used by the official *Kepler* pipeline. This process uses a sliding filter which leaves the short term features such as transit or flares unchanged, while filtering out the longer period trends such as stellar modulation due to rotation. Another flattening technique is to use an iterative spline fit for the light curve. Here, low order polynomials are iteratively fit to sections of the light curve until it is flattened enough to satisfy a predetermined condition.

Figure 2.11 shows the change in the light curve after each step in the reduction process. The top panel shows the raw sums in the aperture. While some transits are apparent, the signal is dominated by the sawtooth pattern caused by the spacecraft drift. The middle panel shows the detrended, but unflattened light curve, with the spline model shown in red. Finally, the bottom panel shows the flattened light curve that will be analyzed for transit signals.

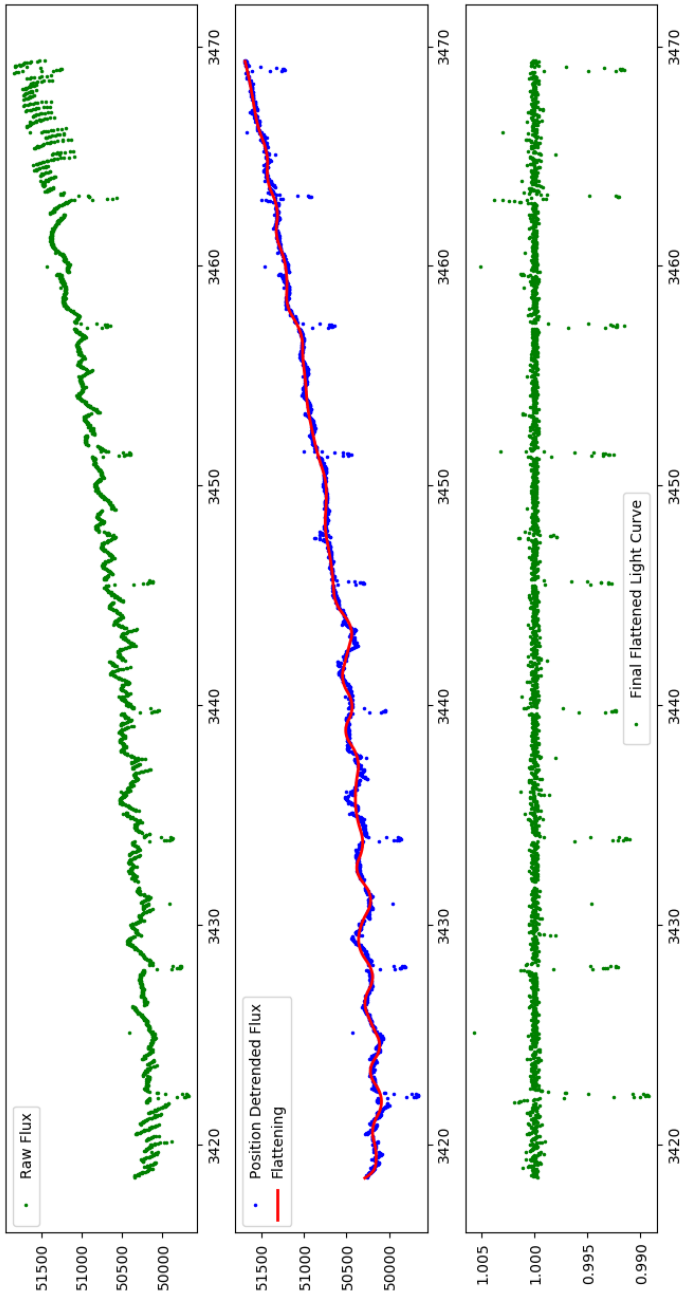

Figure 2.11: Detrending and flattening for EPIC 211962097 using the *K2SFF* reduction pipeline. x-axis and y-axis are time (in days) and flux, respectively.

2.3.4 Reduction Pipelines

Multiple pipelines have been developed to automate the data reduction process. Among them are the aforementioned *K2SFF* and *K2photometry*, as well as *Everest* (Luger et al. 2016) and *K2SC* (Aigrain et al. 2016). The differences between them lie in the different ways each of the steps in the reduction process are handled. In Figure 2.12, we can see the differences between the *K2SFF* and *Everest* reduction pipelines for the three super-Earth system GJ 9827 (Niraula et al. 2017). We use two of these pipelines for reducing *K2photometry* for the reduction of non-bright targets.

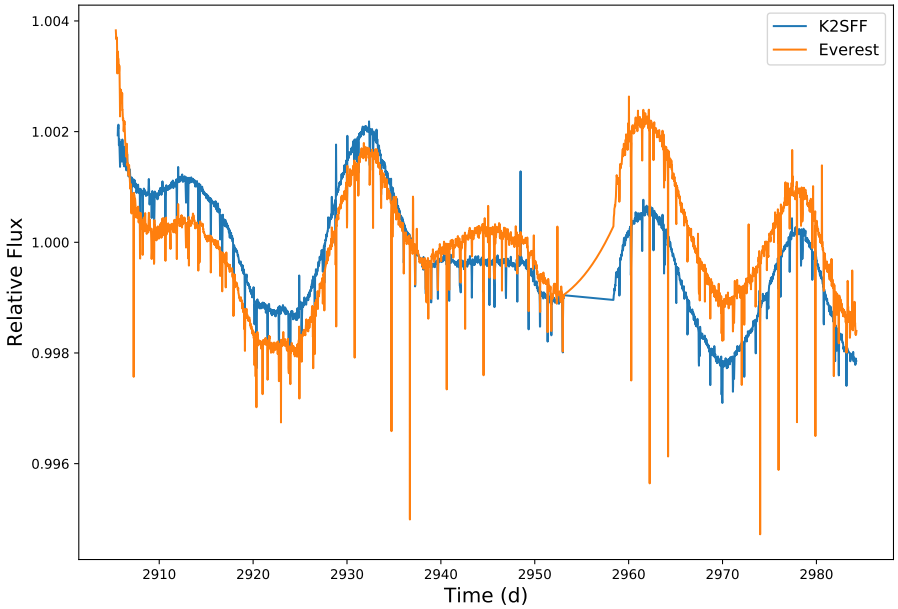

Figure 2.12: Unflattened light curve for GJ 9827 using the K2SFF and Everest reduction pipelines. The depths of some transits differ significantly.

2.4 Transit Search

Once the data are reduced and we have the final light curves, we then search for transit signals. A typical step taken before searching for transit signals is the removal of flaring events and unmarked cosmic ray strikes. This is accomplished using a sigma clipping technique where flux values 3σ above the median value are removed. While there are many methods to search for transit signals, we use a box least squares algorithm (BLS) proposed by Kovács et al. (2002). A simple box or trapezoid is used to model the transits in the light curve. The algorithm finds the best-fit period by sampling various frequencies. The results returned are the phase folded light curves for the four periods with the highest signal-to-noise ratios (Figure 2.13). The top panel shows the flattened light curve generated by our pipeline. The middle panel shows the power spectrum of the sampled frequencies. From left to right, the fourth row shows the light curve folded to the best period, half of the best period, and twice the best period, respectively. Finally, the last row shows phase-folded light curves for the next three periods with the highest SNR. One of these best-fit periods will correspond to the orbital period of the planet when such a signal can be detected. Integer multiples of the period are also strong peaks in the periodogram, since they are harmonics of the true period.

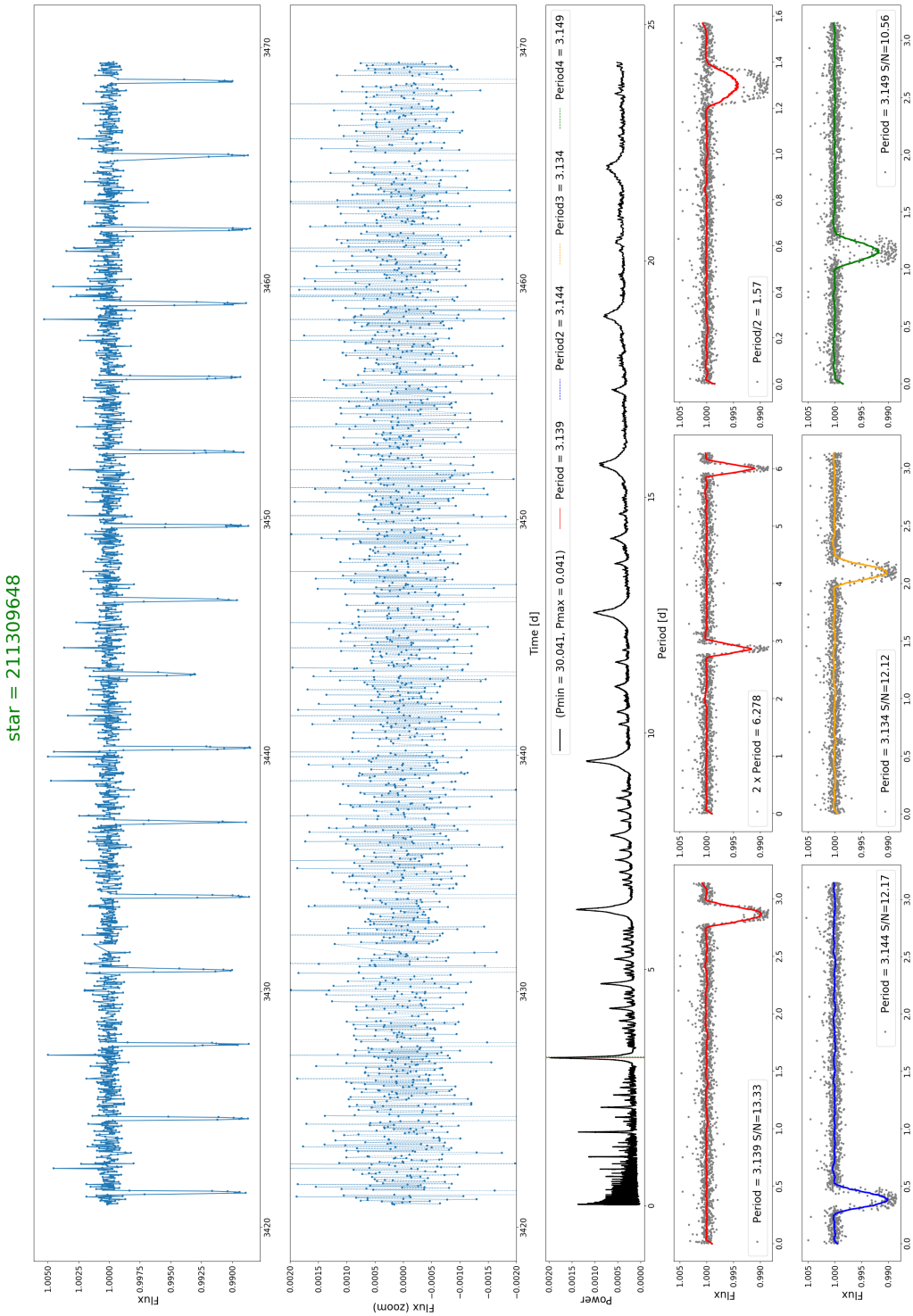

Figure 2.13: BLS results for EPIC 211309648. The four periods with the highest S/N are all within 0.018 days of each other.

2.5 Vetting Potential Candidates

Potential candidates are determined through a manual inspection of the BLS results. We look for results like those shown in Figure 2.13, where the transit signal is readily apparent. When we have such a result, we performing a vetting process to confirm the validity of the presumed detection. The first step is to determine whether the object of interest is already known to have transiting planets with periods similar to those of the BLS results. If so, then we make note of this and de-prioritize the target. If the target does not have a previously detected planet, then we check the literature to see if it is a known eclipsing binary system. If it is and the orbital period is similar to our BLS results, we can reject the results as a non-planet. Even if the target is not listed as an eclipsing binary, it could still turn out to be one. If the transit depth is large ($\gtrsim 10\%$ for a Sun-like star), then the transiting object is too large to be considered a planet. Another method to determine if the system is an eclipsing binary is to test the even and odd transits separately. If the depths are different, then the system is likely an eclipsing binary. If we still have not rejected the target as potentially having a planet, then we can perform more rigorous tests and attempt to fit a model to the light curve in order to retrieve orbital and planetary parameters. This is discussed in more detail in the following chapter.

Chapter 3

Transit Method

3.1 Model

The light curve of a transiting exoplanet can be modelled analytically, as described in the paper by Mandel, & Agol (2002). The transit light curve is a function of planetary, orbital, and stellar parameters. The planetary parameter required is the radius of the planet, which is normally presented as the scaled radius, $R_P/R_\star$, because stellar radii are not always known. The orbital parameters are the orbital period, scaled semi-major axis $a/R_\star$, time of midtransit t_0, inclination i, eccentricity e, and longitude of the periapsis ω. The stellar parameters needed are the stellar radius $R_\star$, stellar mass $M_\star$, and limb darkening coefficients μ_1 and μ_2. Using the data obtained from *K2* observations, we can determine the parameters that generate the best-fit model to the data.

3.1.1 Limb Darkening

A star is not uniformly bright; it is brightest at the center and becomes fainter towards the edge due to the effect known as limb darkening (Figure 3.1). This is due to the fact that different altitudes of the stellar photosphere are being probed at the center and edges (Winn 2010). The "surface" of a star is typically defined to be where the optical depth is 1. To reach an optical depth of 1, one must probe

deeper into the photosphere at the center than the edges. As a result, a hotter and brighter region of the photosphere is observed at the center compared to the edges.

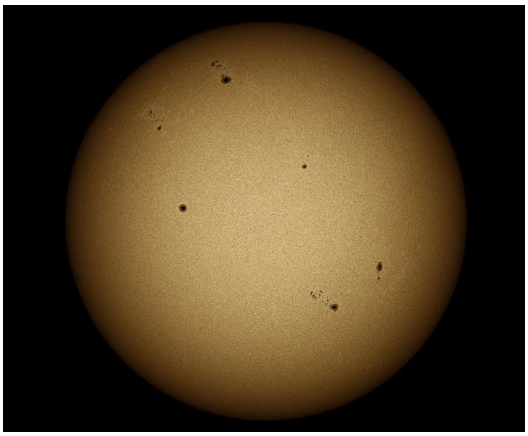

Figure 3.1: The Sun appears brightest at the center and faintest at the edges. Sunspots are present as black spots on the surface. Source: `https://astronomyconnect.com`

Limb darkening can be modelled multiple ways, including with a linear model, quadratic model, or exponential model. We use a quadratic form given as

$$I(\mu) = I_0 \left[1 - \mu_1(1-\mu) - \mu_2(1-\mu)^2\right],$$

where I_0 is the central brightness, μ is a normalized radial coordinate $\sqrt{1-(\frac{r}{R_\star})^2}$, and μ_1 and μ_2 are the limb darkening coefficients. The coefficients are dependent on stellar properties and wavelength of observation. The dependence on wavelength can be seen in Figure 3.2. The bottom of the transit light curve is flatter at longer wavelengths than shorter wavelengths.

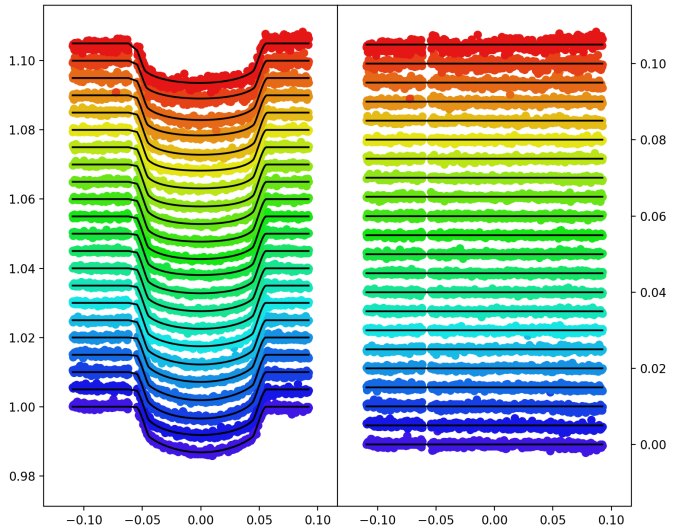

Figure 3.2: Wavelength-binned light curves (left) and residuals (right) from GMOS-N observations of the hot Jupiter XO-2b (Burke et al. 2007). The wavelengths of observations range from $\sim 0.5\,\mu m$ (blue) to $\sim 1\,\mu m$ (red).

3.1.2 Transit Depth

The transit depth is the parameter that holds information about the planet itself, namely its radius. To first order, the transit depth, δ is given by $(R_p/R_\star)^2$. In actuality, the depth can be less than this due to the effects of limb darkening. If the planet's orbit is inclined relative to the observer, then it will not cross the center of the star (i.e., the brightest part). Instead it will cross and block out dimmer regions of the star (Figure 3.3). This effect can be quantified using what is known as the impact parameter, b, which is given by the equation

$$b = \frac{R_\star}{a} \cos i,$$

where $\frac{R_\star}{a}$ is the inverse scaled semi-major axis and i is the orbital inclination.

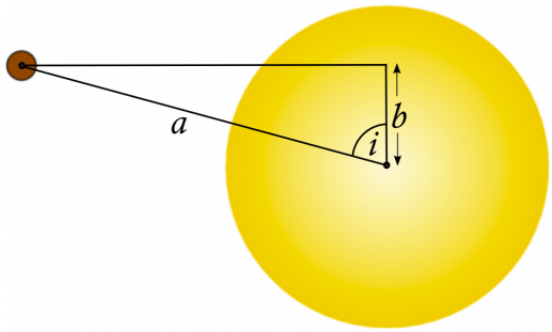

Figure 3.3: Diagram showing impact parameter of a transiting exoplanet.

3.1.3 Transit Duration

The duration of transit is dependent on the period (P), scaled semi-major axis ($a/R_\star$), scaled planet radius ($R_p/R_\star$)and impact parameter (b). It is given by the equation,

$$T = \frac{P}{\pi} \sin^{-1}\left[\frac{R_\star}{a}\frac{\sqrt{(1+\frac{R_p}{R_\star})^2 - b^2}}{\sin i}\right].$$

For a planet, the transit duration is typically a small fraction of the orbital period, from a fraction of a percent for planets with large orbital periods to a few percent for the closest-in planets. An abnormally large duration signifies a non-planetary event, most likely a stellar companion transiting. A short duration is usually indicative of a grazing event (Figure 3.4).

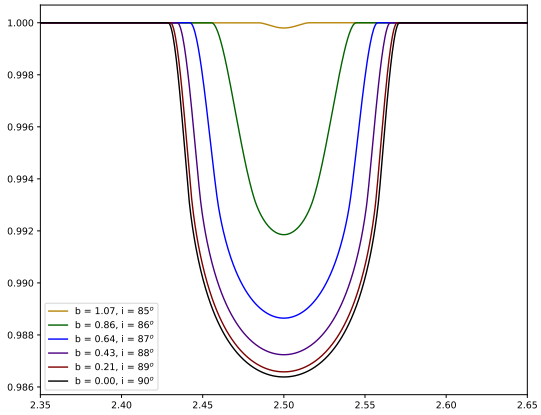

Figure 3.4: Transit light curves of an Earth-Sun analog system, for different orbital inclinations. For inclinations less than 85°, the planet will no longer transit.

3.1.4 Eccentricity and Longitude of the Periapsis

The eccentricity and longitude of the periapsis are two orbital parameters that are poorly constrained by the light curve. To constrain these values, radial velocity measurements are needed. For our model, we hold both of these values fixed. The eccentricity is set to 0, while the longitude of the periapsis is set to 90^o. For short period planets, like those normally found by *K2*, zero eccentricity is a reasonable assumption due to the circularization of the orbit due to tidal interactions with the host star (Udry, & Santos 2007). For a circular orbit, the longitude of the periapsis is degenerate since a circular orbit has no periapsis.

3.2 Fitting

We generate the model light curve using BATMAN (Kreidberg 2015) and use an Markov Chain Monte Carlo (MCMC) algorithm to find the best-fit free parameters. In our model, the free parameters are: mid-transit time (t_0), orbital period

(P), scaled planet radius ($R_p/R_\star$), scaled semimajor axis ($a/R_\star$), orbital inclination (i), and limb darkening coefficients (μ_1, μ_2). We initialize the parameter values through a variety of methods. For the orbital period, we use the suggested period from the BLS results as an initial guess. For the mid-transit time and scaled planet radius, we use the phase-folded light curve. The initial guess for the scaled semimajor axis is determined using Kepler's third law and the stellar mass and radius. We naively set the orbital inclination to a value near 90^o. For the limb-darkening coefficients, we use the table from Sing (2010).

We use the MCMC algorithms from the *emcee* package (Foreman-Mackey et al. 2013) to determine the best-fit parameters. We work in a Bayesian framework and use 50 walkers, each taking 5000 steps, to sample parameter space. The walkers probe different parameters in order to determine where the likelihood of the model is maximized. The best-fit parameters are the median values of the parameters sampled.

3.3 HAT-P-43

HAT-P-43 (also known as EPIC 211317649) is a $K_P = 13.2$ star observed by *K2* in Campaign 18. An exoplanet was detected around the star by Boisse et al. (2013) as part of the Hungarian Automated Telescope Network (HATNet) project (Bakos et al. 2004). The planet, known as HAT-P-43b, is a hot Jupiter orbiting the star, which is slightly larger and older than the Sun (Table 3.1).

We processed the data for this target through our data reduction pipeline and fit the transit light curve to recover planetary and orbital parameters, using the parameters from the detection paper to set initial guesses and bounds on the parameters being fitted. Table 3.2 compares the best-fit parameters to those from

Table 3.1: Stellar parameters.

Parameter	Boisse et al. (2013)
$M_\star\,(M_\odot)$	$1.048^{+0.031}_{-0.042}$
$R_\star\,(R_\odot)$	$1.103^{+0.041}_{-0.021}$
T_{eff} (K)	5645 ± 74
log $g_\star$ (cgs)	4.37 ± 0.02
[Fe/H]	0.23 ± 0.08
Distance (pc)	542^{+22}_{-16}
Age (Gyr)	$5.7^{+1.9}_{-1.1}$

the literature.

Table 3.2: Comparison of MCMC results to literature.

Parameter	This work	Boisse et al. (2013)
Period (days)	3.332688 ± 0.000008	3.332687 ± 0.000015
$a/R_\star$	$6.778^{+0.023}_{-0.022}$	$8.64^{+0.12}_{-0.28}$
$R_p/R_\star$	$0.12017^{+0.00012}_{-0.00013}$	0.1193 ± 0.0018
i (deg)	$84.554^{+0.046}_{-0.043}$	88.7 ± 0.7

The period matches very closely as should be expected. The scaled planet radius is within 1-σ of the literature value. The best-fit semi-major axis and inclination are not within 3-σ of the literature values (Figure 3.6). The transit

duration from the best-fit model is 14 minutes longer than the literature value and the stellar density, which is given by

$$\rho_\star = \frac{3\,\pi}{P^2\,G}\left(\frac{a}{R_\star}\right)^3,$$

is a factor of 2 smaller than that from the literature. The discrepancy between our values and those from the literature arises from not considering this constraint. Our best-fit values are degenerate with those from the literature, but the stellar density breaks that degeneracy.

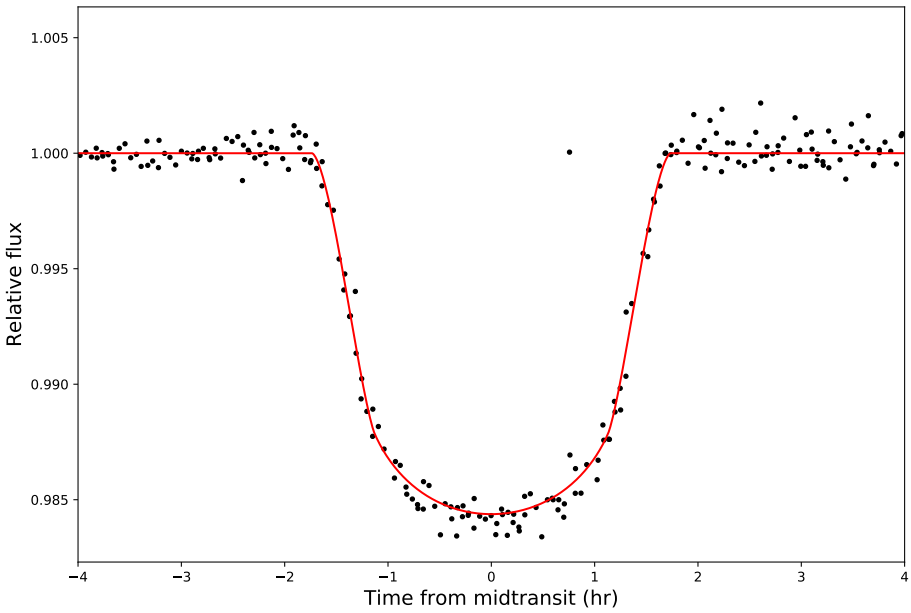

Figure 3.5: Phase-folded data and best-fit model for EPIC 211317649, zoomed in at mid-transit.

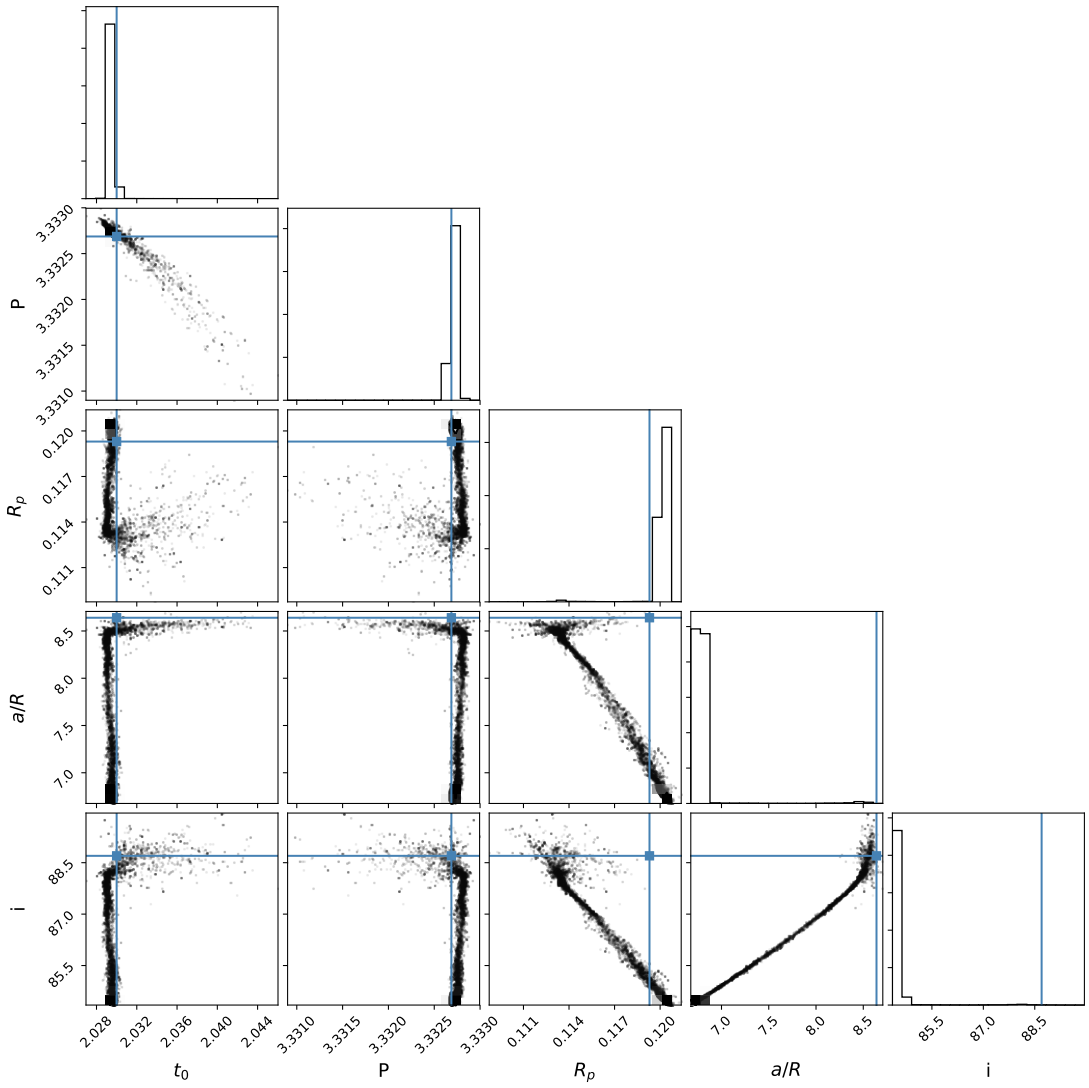

Figure 3.6: Corner plot of the parameters sampled, with literature values shown as the blue lines.

3.4 Campaign 18 Planetary Candidates

In addition to searching for planets around bright stars, I have also been searching for planets around stars in the newest data releases. The last campaign with usable data was Campaign 18, which observed the same general region of the sky as Campaigns 5 and 16. In order to avoid searching for planets that have already been flagged as candidates, I only analyzed targets that had not been observed in the two previous campaigns. Of the over 6,000 unique targets, there were 11 targets that showed some sort of transit signal. These 11 were not known binaries nor did they show different depths in the even/odd test. I fit for the best-fit parameters of each light curve and show the best-fit light curves in Figure 3.7.

The preliminary results indicate that these planets range in size from 2.2 to 10 $R_{\oplus}$. The best-fit light curves also revealed that some of the transits are V-shaped. This occurs when the orbital inclination is small enough that the transiting body only grazes the star. This type of shape is often indicative of a stellar companion, although planets with grazing transits have been detected before (Hellier et al. 2012). BLS results for the reduced data of EPIC 212039291 and EPIC 211681054 did not return the same periods as the raw data, and the transit signal was not apparent when the data were phase-folded. This suggests that the signal seen in the raw data was an instrumental artifact.

The brightest of these candidates is EPIC 211480861, which has a Kp magnitude of 9.96 (Table 3.3. *K2* has observed thousands of stars brighter than this. For the brightest of these stars, we cannot use the same reduction technique as we did here. Instead, we use a completely different and novel method to deal with the complexity of observing bright stars with *K2*.

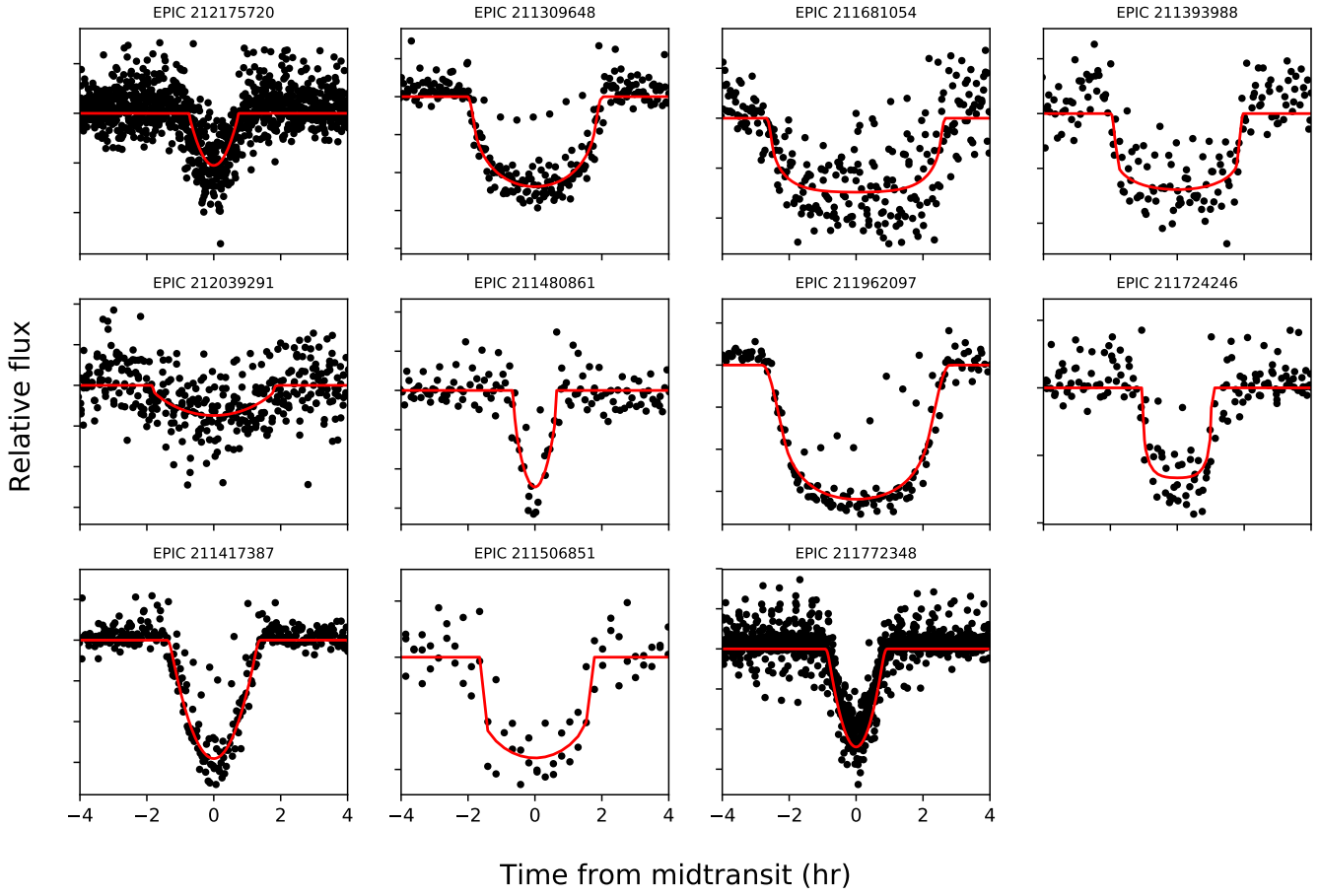

Figure 3.7: Phase-folded, zoomed-in light curves and best-fit light curve for the 11 new planetary candidates from Campaign 18.

EPIC	RA	Dec	Kp	Log g	T_{eff} (K)	$R_\star$ ($R_\odot$)	$M_\star$ ($M_\odot$)	d (pc)	Period (d)	BLS period (d)	$R_p/R_\star$	R_p ($R_\oplus$)	$a/R_\star$	b
211309648	08 55 27.985	10 02 43.04	13.848	4.071	5865	1.551	1.1	957	3.21	3.14	0.05892	9.971	6.6712	0.155
211393988	08 55 13.611	11 32 55.94	13.862	4.234	6280	1.305	1.09	994	4.55	4.87	0.05045	7.183	7.8452	0.495
211417387	08 28 58.837	11 54 10.21	13.051	4.168	6391	1.457	1.216	774	1.815	2.456	0.04646	7.385	5.2328	0.155
211480861	08 18 10.504	12 51 45.66	9.961	3.89	6434	2.221	1.506	308	5.029	6.35	0.0386	9.353	26.2402	0.361
211506851	08 37 01.386	13 14 09.62	13.453	4.492	5498	0.906	0.939	394	10.775	10.533	0.02772	2.74	24.0926	0.447
211681054	08 56 48.457	15 39 38.45	13.497	4.091	5840	1.457	1.041	805	4.136	3.144	0.03469	5.51	6.1199	0.109
211724246	08 44 45.932	16 14 37.25	13.242	4.199	5989	1.296	1.065	702	4.934	4.745	0.03298	4.66	18.0003	0.224
211772348	08 19 46.331	16 55 27.13	13.731	4.517	5485	0.837	0.863	543	0.5209	0.651	0.08686	7.93	2.2965	0.493
211962097	08 53 36.859	19 39 26.19	13.57	4.062	6113	1.554	1.084	1000	4.9373	5.84	0.08424	14.28	5.9242	0.648
212039291	08 32 40.685	20 54 45.03	13.206	4.202	6139	1.327	1.085	733	2.5136	2.23	0.0153	2.214	5.2375	0.162
212175720	08 51 11.938	23 37 36.31	13.503	4.305	5972	1.133	1.008	683	0.7813	0.703	0.0239	2.953	4.1269	0.127

Table 3.3: Stellar, orbital, and planetary values of the Campaign 18 candidates from the literature and our best-fit.

Chapter 4

Bright Stars

4.1 Sample

The *K2* mission tended to avoid observing bright stars because of the issue of pixel saturation and bleeding. To date, the brightest star with a confirmed exoplanet discovered by *K2* is K2-167, a Kp = 8.22 star with a super-Earth orbiting it every 9.98 days (Vanderburg et al. 2016). The *K2* mission has observed over 1000 stars brighter than K2-167 and we perform a systematic search for exoplanets orbiting these stars. This includes 957 stars with explicit Kp magnitudes less than 8.22 and approximately 159 additional bright stars with no listed Kp magnitudes observed as part of bright star programs by Daniel Huber. The faintest of these stars has V = 7.02.

Stellar classification was performed for approximately 138,000 of the stars observed by *K2* (Huber et al. 2016). A combination of colors, proper motions, spectroscopy, parallaxes, and galactic population synthesis models were used to classify targets and derive stellar parameters. We use the classifications and stellar parameters of the bright star sample to construct the Hertzsprung-Russell diagram shown in Figure 4.1. The 150 bright stars from the bright star programs by Huber were not classified and are thus not shown in the HR diagram.

It is readily apparent that our sample of bright stars is heavily biased towards

the physically larger early-type and post-MS stars. As a result, the sample of smaller, later-type dwarf stars that are ideal for planet detection by *K2* number around 250 (Figure 4.2).

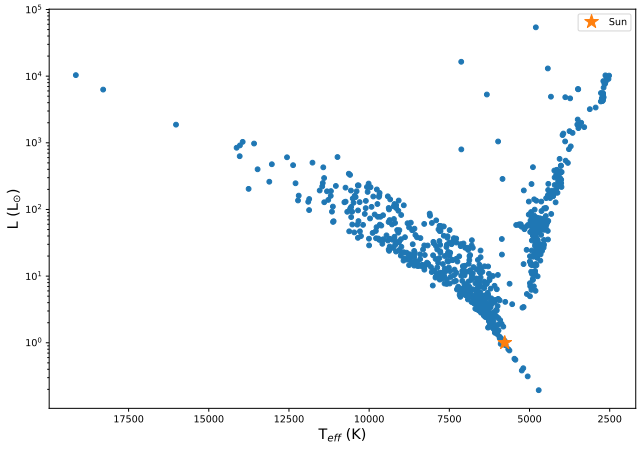

Figure 4.1: HR diagram of bright stars observed with *K2* with available data.

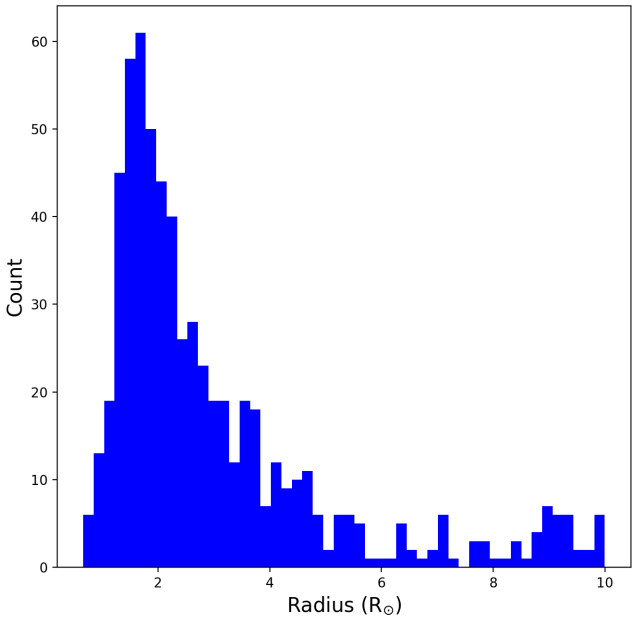

Figure 4.2: Histogram of the radii of bright stars observed with *K2*.

4.2 Issues

The main issue with observing bright stars is that they quickly saturate the detector at Kp ≈ 11.3 (Gilliland et al. 2010), which leads to column bleeding. The FITS files for these stars are on the order of 1 GB. Due to *K2*'s bandwidth constraints, recording and downloading the entire flux of bright stars was not very practical. The FITS files for fainter, non-saturated stars are on the order of only 10-100 MB.

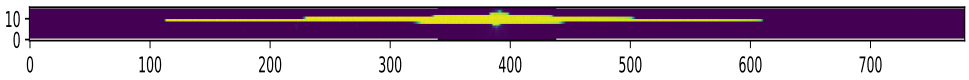

Figure 4.3: An example of a bright star observed by *K2*. The image has been rotated 90° and stretched to better show the bleeding. Bleeding stretches for hundreds of rows.

Another issue that affects many of the bright stars observed by *K2* is contamination by nearby, fainter stars in the field of view. Since brighter stars require a large field of view to fully capture their flux, field stars are often present in the images. When generating the light curve of a bright star, the flux from these field stars can alter the true light curve. This issue is discussed further in Section 4.4.

There have been multiple techniques developed to analyze *K2*'s bright stars. One such technique uses "smear" data (Pope et al. 2016). This technique uses engineering data taken during CCD readout, which features far less column bleeding than the science data. Another technique was developed as part of updated Everest data reduction pipeline, Everest 2.0, which collapses the saturated columns (Luger et al. 2018).

4.3 *Halophot*

The developers of the smear technique later developed another technique to study bright stars known as *halophot* (White et al. 2017). Instead of using the entire image with bleeding columns, their new technique looks at only the immediate halo surrounding the bright star. By using a much smaller aperture, the FITS files are only 10 MB, a factor of 100 smaller than if the entire image were used. It also uses a weighted flux instead of the usual unweighted simple photometry. The total weighted flux of a single frame, f_i, is given by the equation

$$f_i = \sum_{j=1}^{M} w_j \, p_{ij}.$$

The weights w_j are determined by minimizing the variation of the flux from frame to frame. The total variation of N exposures, TV, is given by

$$TV = \frac{\sum_{i=1}^{N} |f_i - f_{i-1}|}{\sum_{i=1}^{N} f_i}$$

The optimal weights are calculated by minimizing the TV function using sequential least squares as implemented in the *scipy.optimize.minimize* function. The weights are constrained to be positive and sum to unity. Saturated pixels are masked out and not weighted through the use of a threshold filter.

This method removes the pointing drift signal and jumps of the telescope as part of the calculation of the weights. The drift is anti-correlated with the roll while the stellar signal is correlated. The jumps are suppressed through the correct combination of weights as the jumps cause larger, sudden changes in flux and thus contribute significantly to the TV function. The authors claim that the true stellar signal is difficult to suppress because the signal is present in all pixels

(Figure 4.4). We investigate this further in Chapter 6.

4.3.1 Applications

White et al. (2017) applied this technique to study the 7 brightest stars in the Pleiades. They found that 6 of them showed pulsations with periods under a day. They also found that the 7th star, Maia, varied over a period of 10 days (Figure 4.4). Follow-up spectroscopic observations found a 10 day period variation in the equivalent width of a Mn II absorption line at 4756 Angstroms. This finding suggested that the variation from *K2* observations is a true signal and is the result of rotational modulation. In a bit of irony, it also showed that Maia itself was not a Maia type variable star.

This technique has also been used to perform asteroseismology on two planet-hosting red giant stars - Aldebaran (Farr et al. 2018) and ϵ Tauri (Arentoft et al. 2019). These measurements were used to determine stellar mass and in turn, constrain the masses of orbiting exoplanets. With periods of over 500 days, neither planet would likely be detected using *K2*.

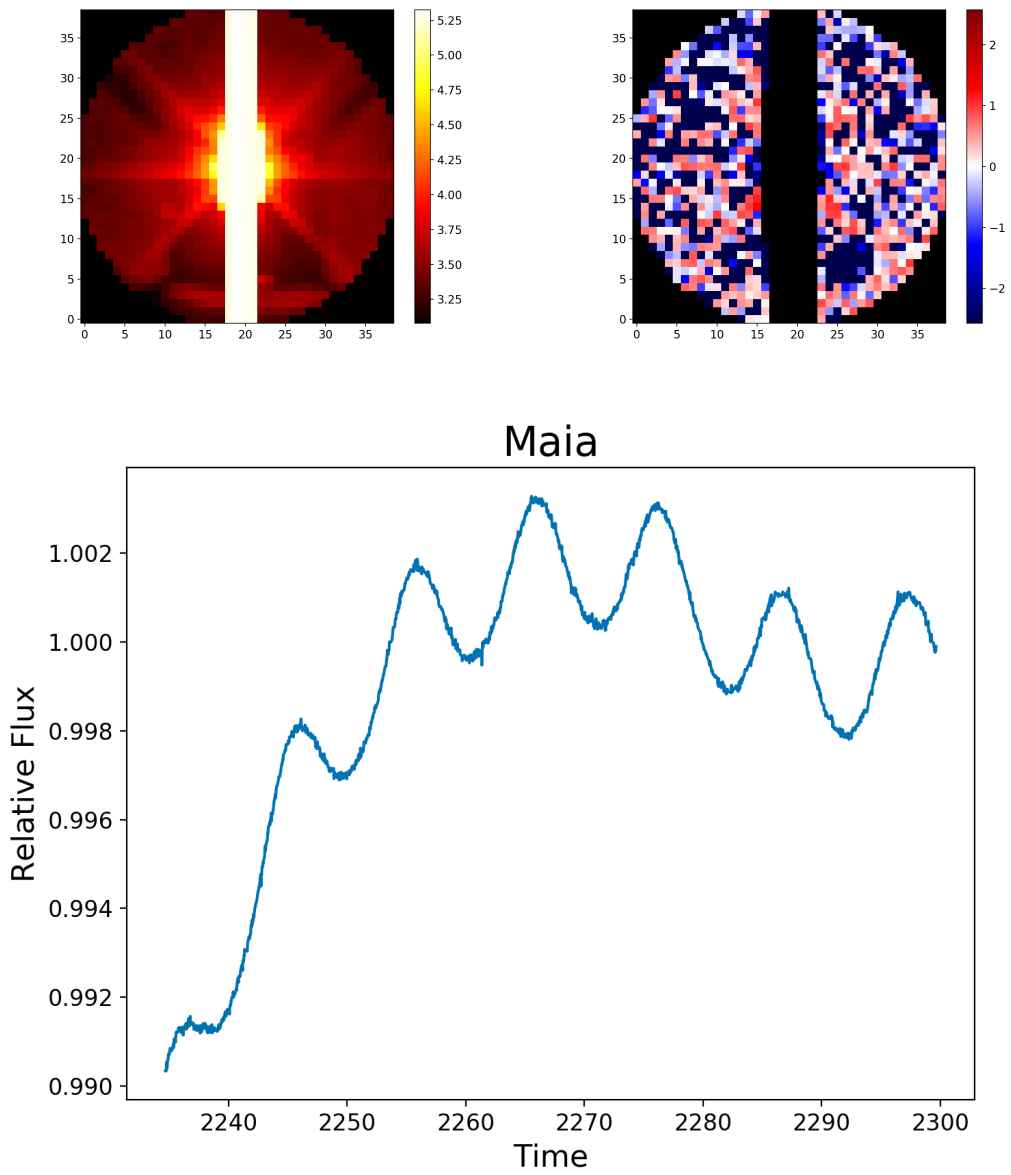

Figure 4.4: Flux (left), weightmap (right), and unflattened light curve (bottom) for Maia, a bright member of the Pleiades observed in Campaign 4.

4.4 Field Stars

Of the sample of 1061 bright stars, 360 are contaminated by fainter field stars in and around the bright star's halo. When calculating weights, less variable field stars can be weighted more heavily than a variable bright star (Figure 4.5). This causes the light curve to be contaminated by the heavily weighted flux of the field stars, which dilutes the signal of the bright star of interest. In Chapter 5, I examine this effect in more detail.

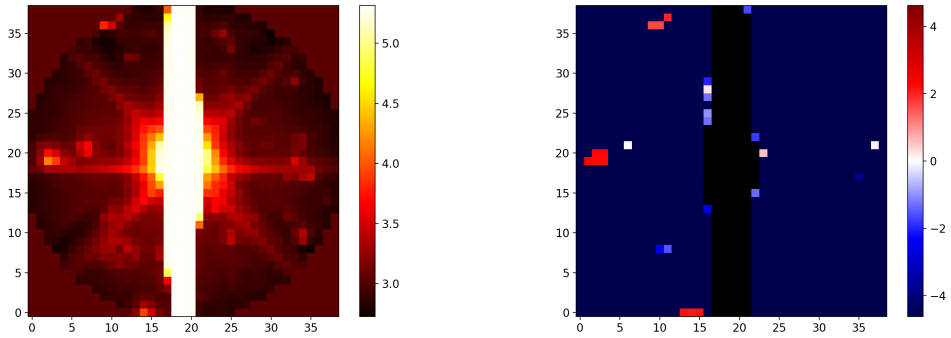

Figure 4.5: Flux map and weightmap of EPIC 20062584, a bright target observed in Campaign 7. Multiple field stars in the field of view are weighted in favor of the bright star.

4.4.1 Catalog Search

When considering how to deal with contaminating field stars, it is necessary to locate all of the stars in the field of view. We query the *Gaia* Data Release 2 catalog (Gaia Collaboration et al. 2018) to find all of the sources within a 100 arcsecond radius of a bright star, as this corresponds to a 25 pixel radius around the bright star. We then limit the results to sources brighter than G = 18 and convert the coordinates to pixel values using astropy's *wcs* module (Figure 4.6).

We choose G = 18, because sources fainter than this blend in with the halo. *Gaia*'s G band and *Kepler/K2*'s Kp band cover a similar range of the spectrum (Figure 4.7).

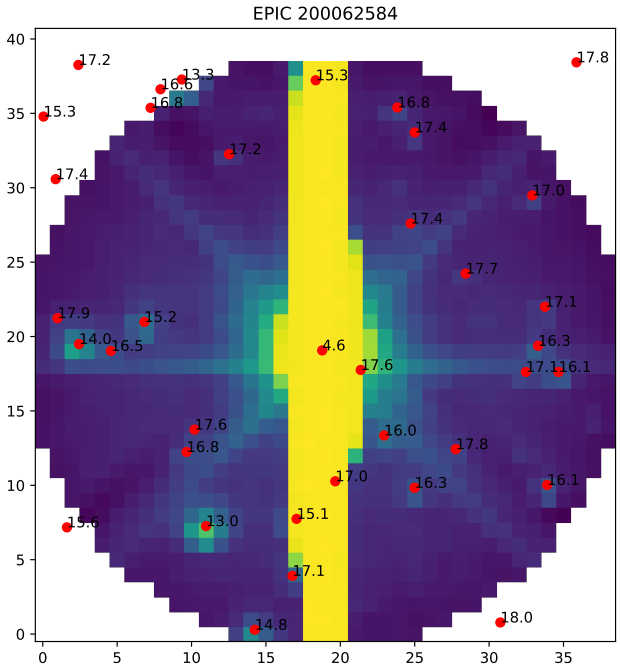

Figure 4.6: An example of a contaminated bright star, with all sources in the FOV with G $<$ 18 shown as red dots.

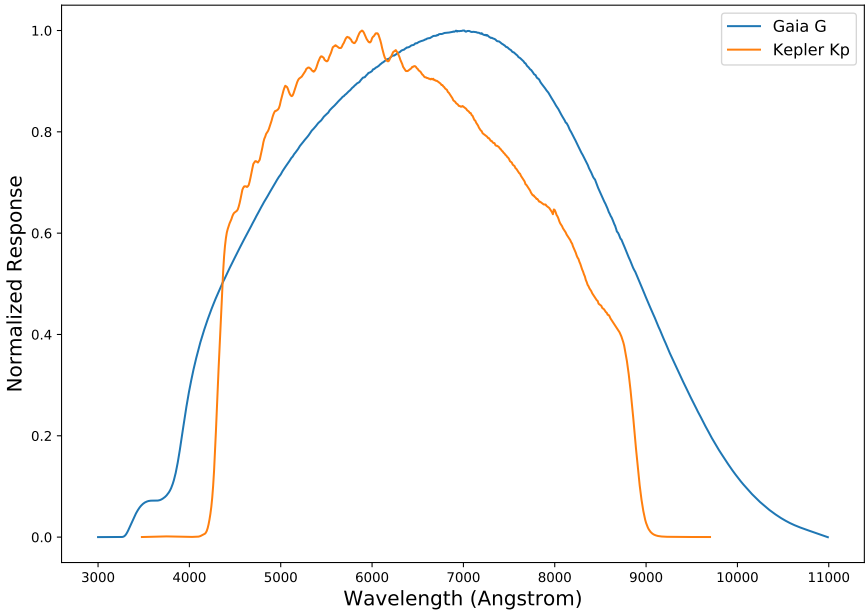

Figure 4.7: Normalized response functions for *Gaia* G band and *Kepler* Kp band.

4.4.2 PSF Fitting and Removal

Once the positions of the sufficiently bright field stars are known, we can then attempt to fit and subtract them from the image. While other models have been used to model the point spread function, or PSF, (Libralato et al. 2016,?; Nardiello et al. 2016) we use a two-dimensional Gaussian given by

$$f(x, y) = A \exp[-(a\,(x - x_0)^2 + 2\,b\,(x - x_0)\,(y - y_0) + c\,(y - y_0)^2)] + k,$$

where A is the peak flux at the center of the star x_0, y_0, and k is the background flux. a, b, and c are constants dependent on the widths (σ_x, σ_y) and orientation angle (θ). The relation is given by

$$a = \frac{cos^2\theta}{2\sigma_x^2} + \frac{sin^2\theta}{2\sigma_y^2},$$

$$b = -\frac{sin2\theta}{4\sigma_x^2} + \frac{sin2\theta}{4\sigma_y^2},$$

$$c = \frac{sin^2\theta}{2\sigma_x^2} + \frac{cos^2\theta}{2\sigma_y^2}.$$

In Chapter 6, we examine the validity of using a two-dimensional Gaussian to model the PSF of the field stars. Some of the field stars are bright, meaning saturation and bleeding effects come into play. Field stars can also sit on diffraction spikes, which causes significant deviations from the assumptions made to fit the Gaussian.

EPIC 211719918

The ideal case in which to use a two-dimensional Gaussian is with a faint, isolated star. Here, we choose EPIC 211719918 (EGGR 904), a faint (Kp = 15.733) white dwarf observed in Campaign 18 that is known to be variable (Brinkworth et al. 2013). It was also observed in Campaigns 5 and 16, and was found to have rotational period of 5.7 hours (Hermes et al. 2017). We fit a Gaussian to the data and generate a new FITS file using the modelled flux as the data. We then process the original and Gaussian-fit files using our standard data reduction pipeline to generate flattened light curves (Figure 4.8). Figures 4.9 and 4.10 show the BLS results of the two light curves and we find that they have the same four best periods. None of them match the period from the literature, but one of them is twice the period, showing that the Gaussian PSF can recover the stellar signal.

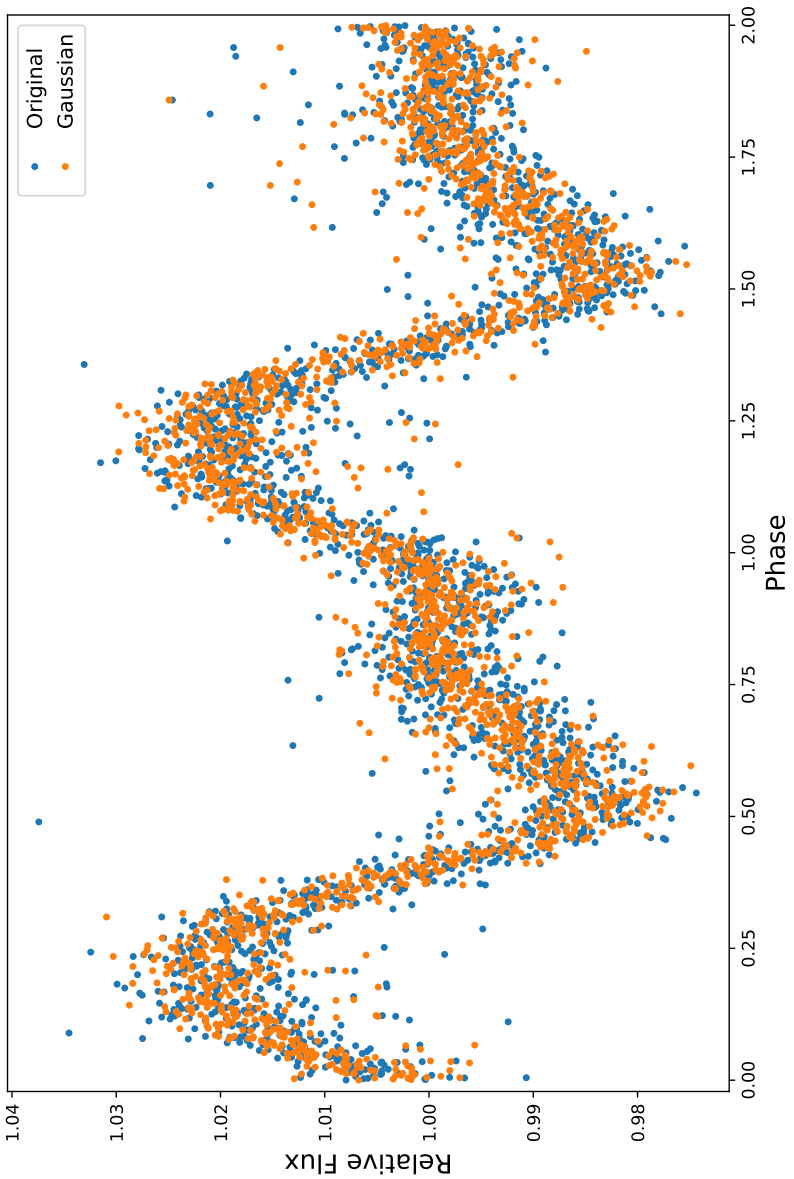

Figure 4.8: Original and Gaussian flattened light curves, phase-folded to show 2 cycles.

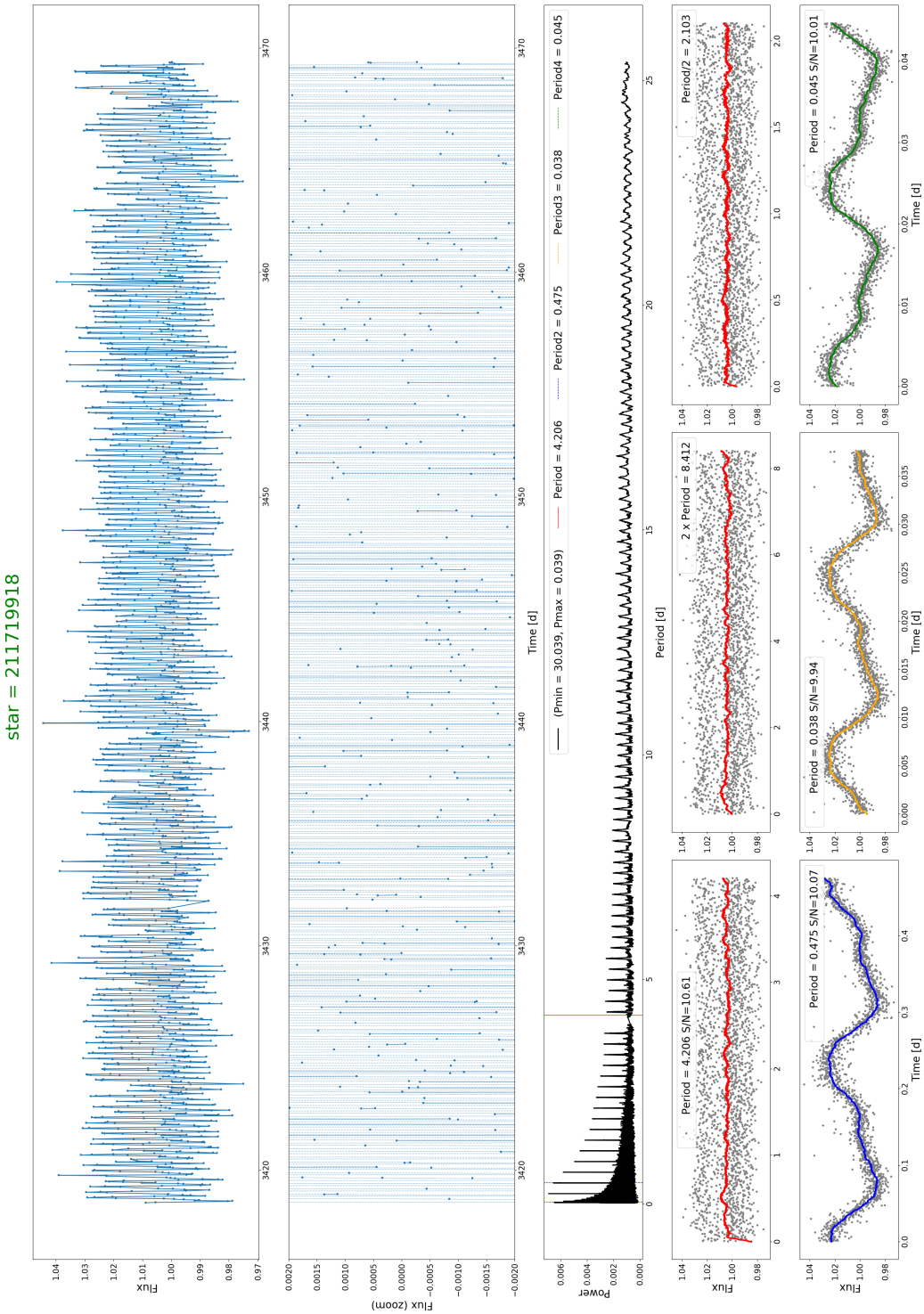

Figure 4.9: BLS results using the original stellar flux. The bottom left panel contains the phase-folded light curve for twice the literature period.

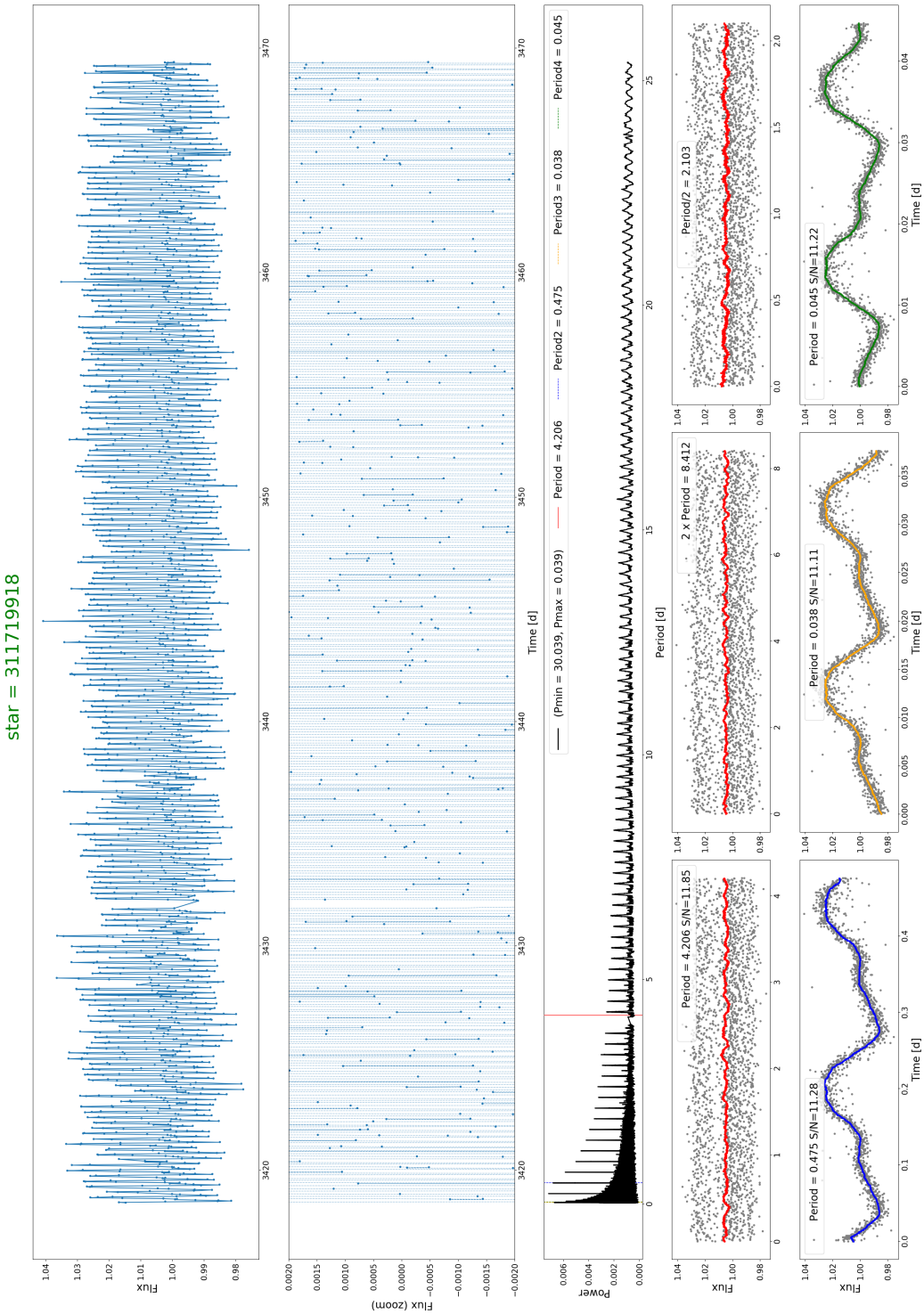

Figure 4.10: BLS results using the Gaussian fitted flux. The four best periods of this light curve are the same as for the original data.

4.4.3 Exoplanet Search

While these field stars are not the focus of our exoplanet search, they represent a promising group of targets to study. In some ways, the sample of field stars is more conducive for planet search, as these field stars are fainter and not as biased towards large early-type or post main-sequence stars. This sample has been overlooked, as they are either not identified as targets in the *K2* data archive, or if they are, they do not have their own postage stamps.

4.5 Target Prioritization

When considering that a large fraction of the bright star sample is contaminated by field stars, it becomes necessary to prioritize targets for the search of transiting exoplanets. The sample can be divided into two groups - stars that are uncontaminated and stars that are contaminated (Figure 4.11). We consider uncontaminated stars to be those with no field stars within a 20 pixel radius of the star's center, as the halo never extends past $\sim$ 15 pixels. We are able to process these stars immediately using *halophot*, then flatten the light curve and search for periodicity in the final light curve.

The contaminated star sample can be broken down further in terms of the perceived difficulty of the PSF fitting and removal process. The criteria for determining the perceived difficulty are the number of stars and their locations relative to the halo. Bright targets with only one or two field stars outside of the halo are prioritized over bright targets with multiple field stars in the halo, especially those sitting on diffraction spikes.

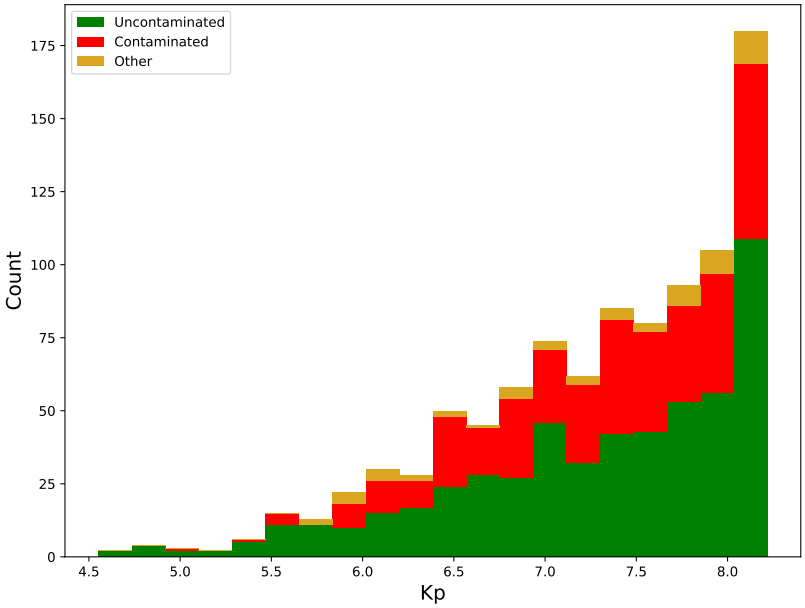

Figure 4.11: Histogram of bright targets observed by *K2*, separated into the three main classifications. Other are targets that appear to be erroneously listed as bright targets after examining their flux maps. 58 targets are classified as this.

Chapter 5

Results

I have processed the 603 uncontaminated bright stars using *halophot* and searched for transit signals in the flattened light curves using BLS. A review of the light curves and results from BLS does not reveal any promising planetary candidates. The processing of the uncontaminated targets does reveal a rich set of data for variable stars. I present an example, EPIC 245469764, as well as a variable contaminated star, EPIC 204760247, in Section 5.2.

In order to demonstrate the effectiveness of this technique in terms of detecting exoplanets, I apply it to a fainter target with a confirmed exoplanet detection. The target, EPIC 201498078, is a relatively bright G type star observed in Campaign 14. I discuss the planetary system, the reduction and fitting process, and results in more detail in the next section.

5.1 EPIC 201498078

With a Kp = 9.8, EPIC 201498078 is one of the brightest K2 targets with a confirmed exoplanet detection. The detection of an inflated super-Neptune ($R_P \sim 0.85 R_J$, $M_P \sim 0.2 M_J$) orbiting the star every 11.63 days was reported by both Johnson et al. (2018) and Brahm et al. (2019). The former group processed the data using *SFF* while the latter used the *EVEREST* pipeline. The planet orbits an 8.8 Gyr old star slightly more massive than the Sun (1.1 $M_\odot$), placing

the star at the boundary of the main-sequence and sub-giant branch. Independent follow-up radial velocity measurements from both teams revealed that the planet is in a highly eccentric orbit, with reported eccentricities of 0.39 ± 0.15 (Johnson et al. 2018) and 0.42 ± 0.03 (Brahm et al. 2019)).

I process the target data using *halophot*, while disabling the maximum threshold filter due to the lack of column bleeding as shown in Figure 5.1. Transit-like events are evident in the unflattened light curve, with a period on the order of 10 days. To determine the periodicity of the transit signal, I flatten the light curve using a Savitzky-Golay filter and process the resulting light curve using BLS. The four periods with the highest signal-to-noise ratios are all clustered near the reported period of 11.63 days, ranging from 11.622 to 11.647 days as is shown in Figure 5.2.

I use the period with the fourth highest SNR (P = 11.634 d) to phase-fold the data, as it is the closest to the values reported in both detection papers. I then use the phase-folded light curve to determine the best-fit transit parameters. I model the light curve using BATMAN and fit for the parameters using MCMC as described in Chapter 4. I fit for the mid-transit time, period, scaled planet radius $R_P/R_\star$, scaled semi-major axis $a/R_\star$, and inclination while adopting fixed values for the eccentricity and longitude of periastron from the literature. As the period has been well-constrained, I only allow it to vary over a range of 0.001 days. Similarly, with the stellar mass and radius known, the scaled semi-major axis can be constrained somewhat tightly to between 9 and 15. The resulting best-fit light curve is plotted over the phase-folded data in Figure 5.3.

The best-fit period is in good agreement with the literature values, although the period was tightly constrained. The scaled semi-major axis is within 1-σ of the value from Johnson et al. (2018), but not within 3-σ of the value from Brahm

et al. (2019). Our best-fit value for $R_P/R_\star$ is not within 3-σ of either literature value, but our inclination is within 3-σ of the value from Johnson et al. (2018) (Figure 5.4). This does not mean our reduction technique is flawed however, as one can have the same transit depth even with different radius and inclination values. There exists a degeneracy between the two parameters and the transit depth that allows different combinations of radii and inclinations to give the same transit depth. Furthermore, this system is very eccentric and a transit light curve alone will not break the degeneracies between eccentricity and other parameters. It would require radial velocity measurements, and in fact, that is what was used in both groups.

Table 5.1: Comparison of best-fit parameters between this work and literature values

Parameter	This work	Johnson et al. (2018)	Brahm et al. (2019)
Period (days)	$11.63292^{+0.00020}_{-0.00018}$	11.63344 ± 0.00012	11.63365 ± 0.00010
$a/R_\star$	$10.75^{+0.24}_{-0.10}$	$13.3^{+2.4}_{-2.6}$	$13.38^{+0.16}_{-0.18}$
$R_p/R_\star$	$0.05495^{+0.00022}_{-0.00034}$	$0.05293^{+0.00096}_{-0.00051}$	$0.05178^{+0.0006}_{-0.0005}$
i (deg)	$85.16^{+0.30}_{-0.12}$	$88.4^{+1.1}_{-1.9}$	$89.20^{+0.57}_{-0.68}$

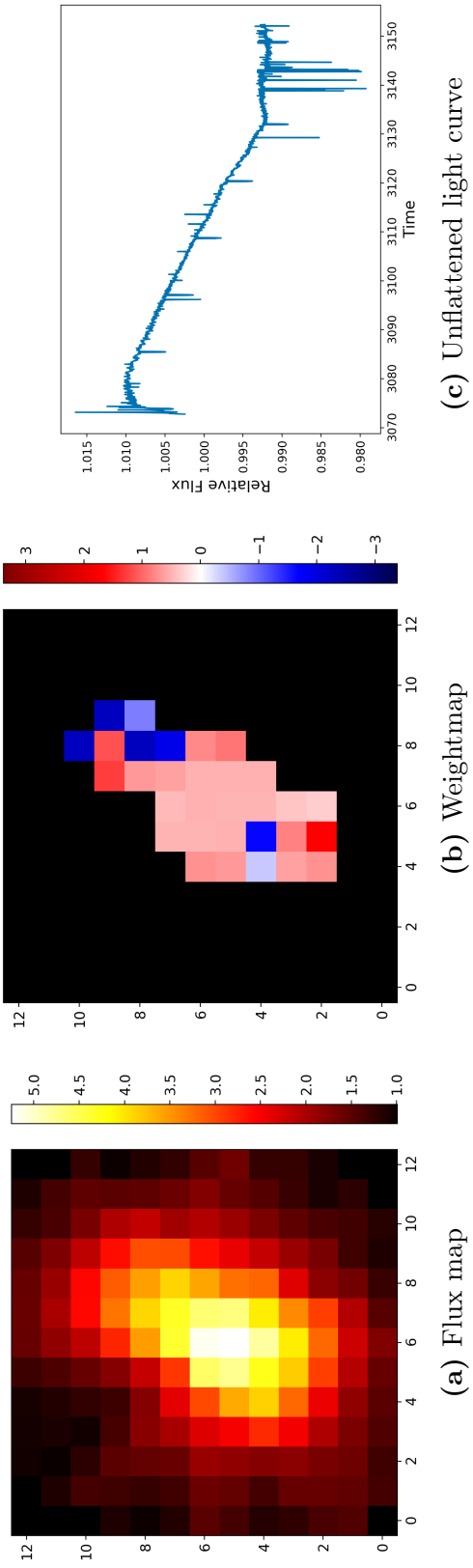

(a) Flux map **(b)** Weightmap **(c)** Unflattened light curve

Figure 5.1: *Halophot* results for EPIC 201498078

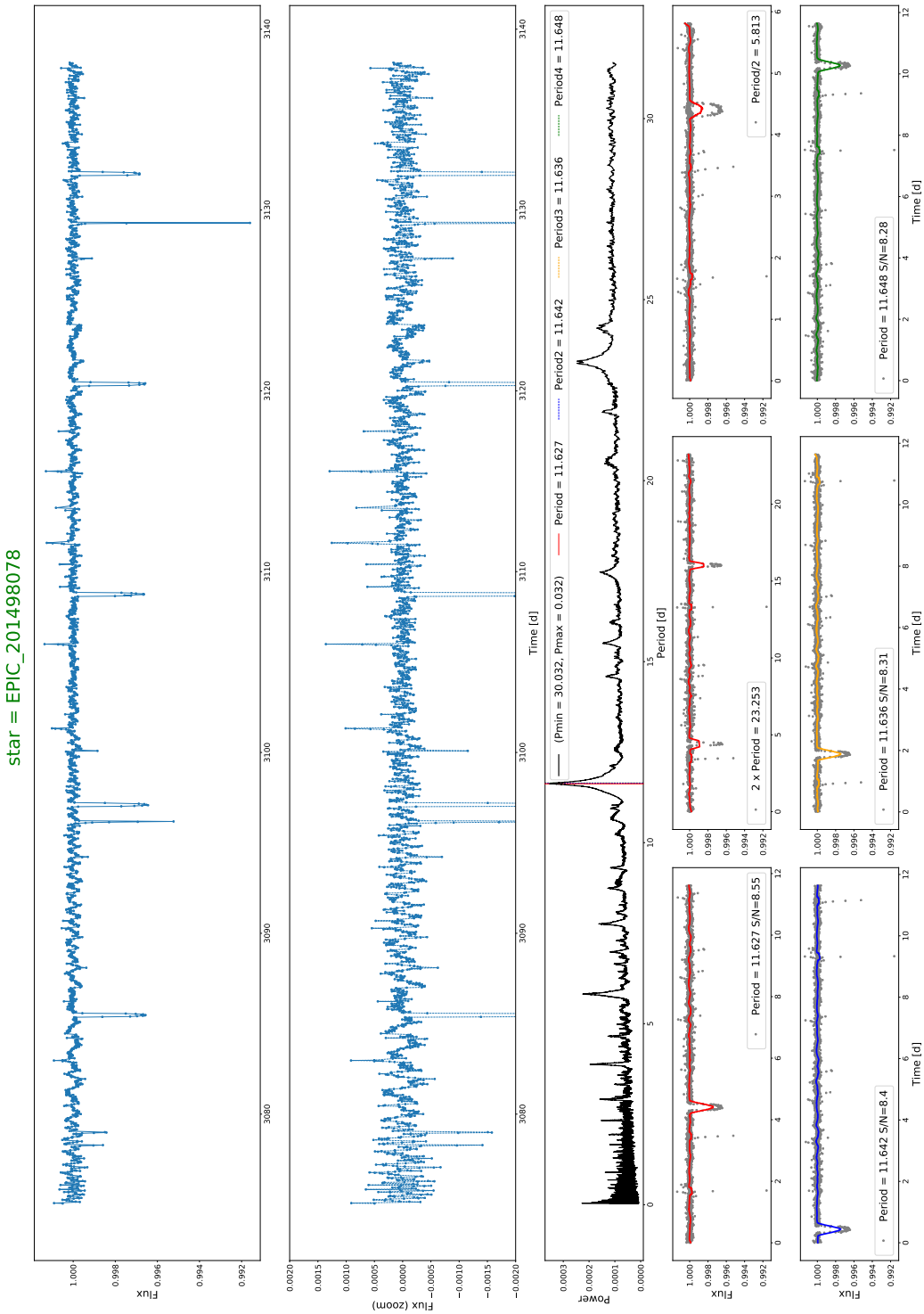

Figure 5.2: BLS results for EPIC 201498078.

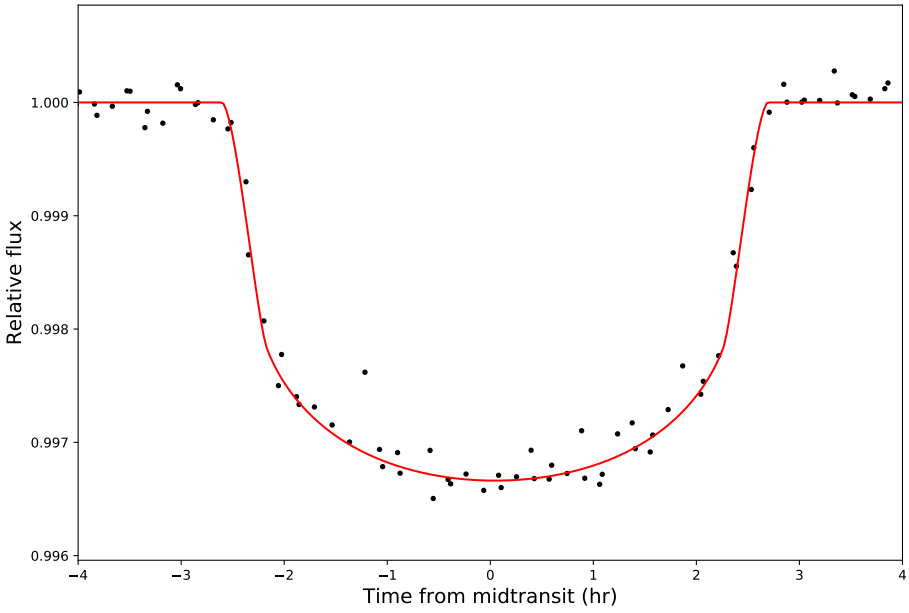

Figure 5.3: Phase-folded light curve, centered on mid-transit.

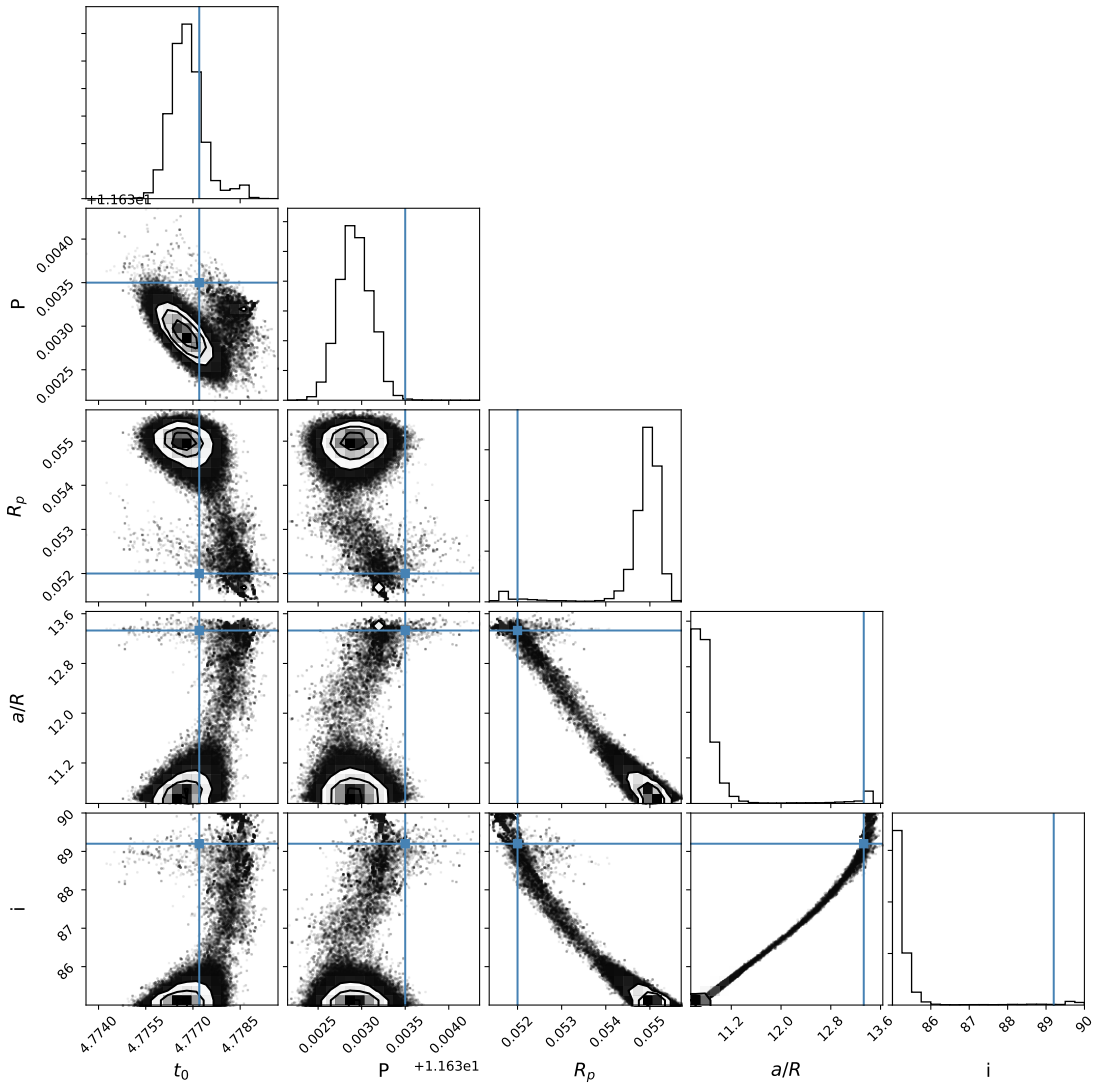

Figure 5.4: Corner plot for fitted parameters, with average literature values listed as blue lines.

5.2 Stellar Variability

K2 provides a rich observational data set for studying stellar variability (Armstrong et al. 2015). *K2* data have been used to study disk-bearing stars and stellar rotation in open clusters (Ansdell et al. 2016; Rebull et al. 2017) and well as O and B type stellar variability (Balona et al. 2015; Buysschaert et al. 2015). They have also been used to study RR Lyrae variable stars in the satellite dwarf galaxy Leo IV (Molnár et al. 2015). The sample of bright targets I analyze includes a large number of known variable stars. I query Simbad for information on stellar variability of the 603 uncontaminated bright targets and present some of the results in Table 5.2. Types of variability include but are not limited to eclipsing binaries, δ-Scuti variables, Cepheid variables, and long period variables.

5.2.1 EPIC 246469764

EPIC 246469764, or κ Piscium, is a bright (Kp = 5.018) A2V star observed in Campaign 12. It is classified as an α^2 Canum Venaticorum variable star (Samus' et al. 2017). It has a strong, variable magnetic field with peculiar lines in its spectra, including silicon, strontium, chromium, and uranium absorption lines. Rotational variability is the result of uneven distribution of metals in the photosphere (Muthsam, & Stepien 1980). I process this target using *halophot* (Figure 5.5) and use BLS to determine the period of the variability. The period with the highest SNR is 1.415 days (Figure 5.6). This period and strength of fluctuation ($\sim$ 0.01 mag) strongly agree with the literature. A search of the literature returns reported periods on the order of 0.58 days (Rakos 1962; van Genderen 1971) as well as 1.41 days (Kreidl, & Schneider 1989; Kerschbaum, & Maitzen 1991).

Table 5.2: Count of uncontaminated stars by selected variability type

Variability Type	Count
α^2 CVn	8
β Cepheid	3
BY Draconis	3
δ Cepheid	1
δ Scuti	21
Eclipsing Binary (incl. candidates)	5
Long Period (incl. candidates)	10
Spectroscopic Binary	24
T Tauri (incl. candidates)	4
Variable (no specification)	13

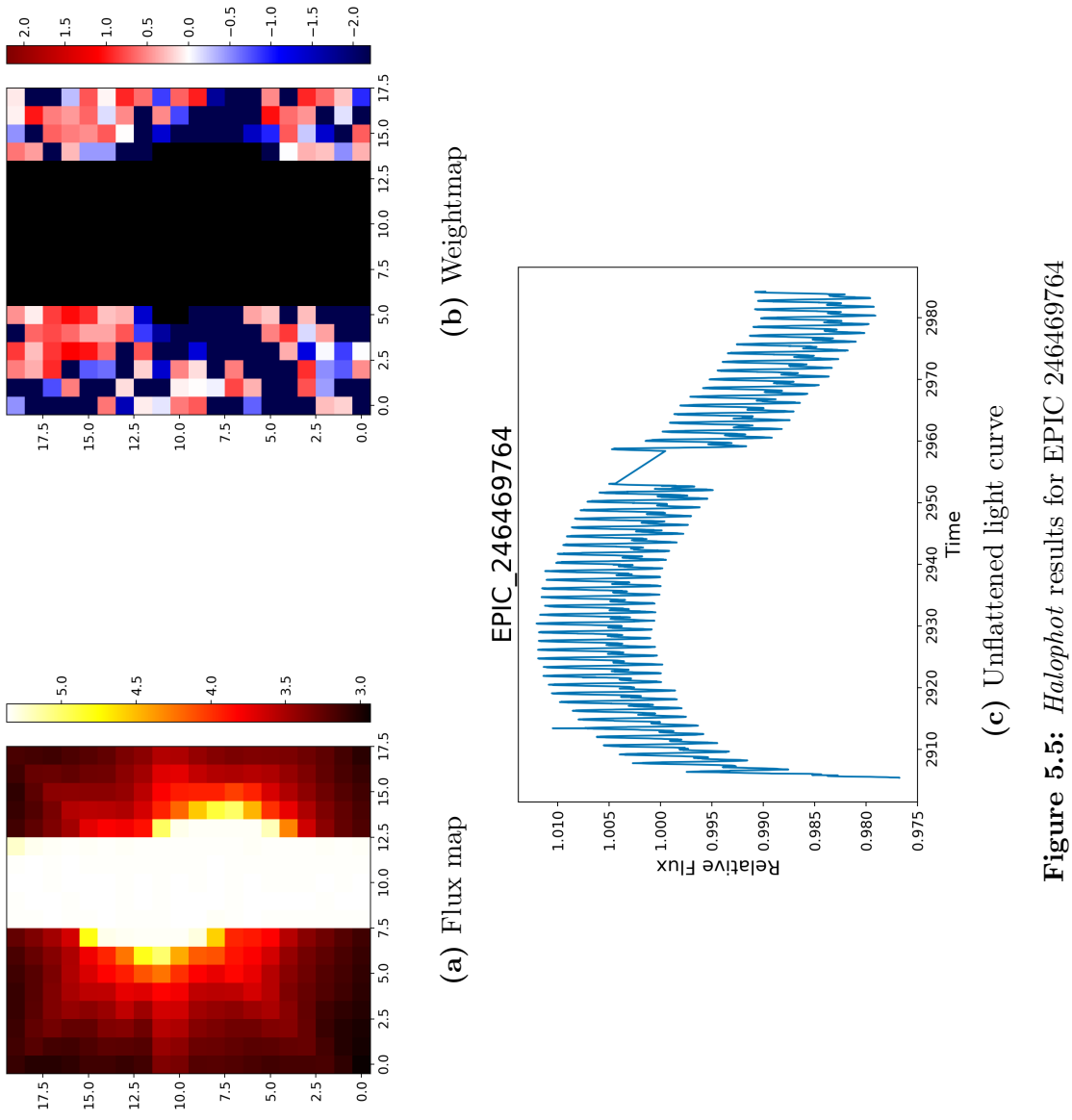

(a) Flux map **(b)** Weightmap **(c)** Unflattened light curve

Figure 5.5: *Halophot* results for EPIC 246469764

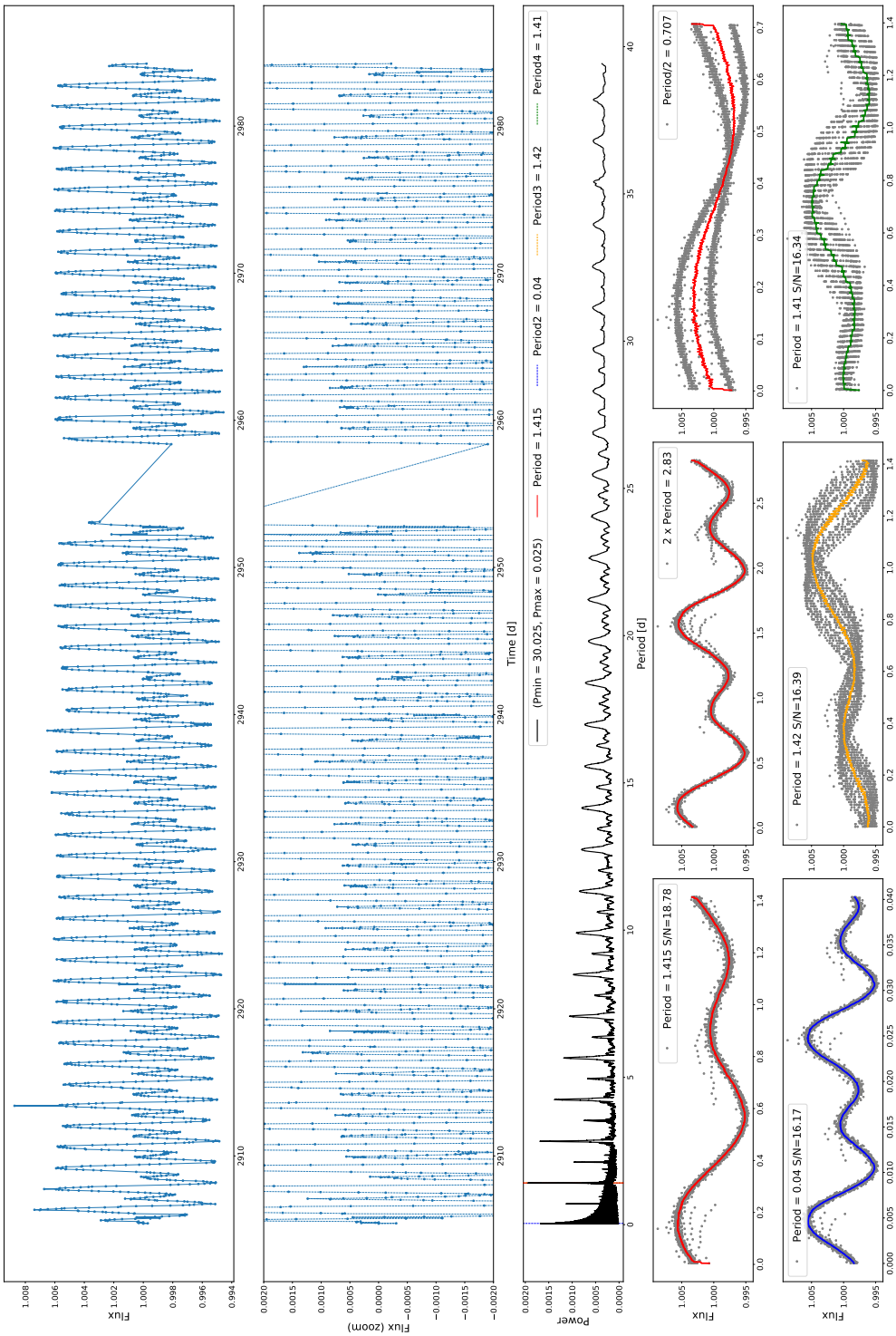

Figure 5.6: BLS results for EPIC 246469764.

5.2.2 EPIC 204760247

EPIC 204760247 is a bright (Kp = 5.95) B3V star that was observed in Campaign 2. It is a member of the Upper Sco Association (Madsen et al. 2002) and has previously been observed to be variable. Hill (1967) tentatively classified the star as a β Cepheid variable, and Andersen, & Nordstrom (1977) reported that the star was a double-lined spectroscopic binary. Further observations of the system revealed it was an eclipsing binary with a period of 9.2 days (Wraight et al. 2011).

K2 data for the star have been extensively analyzed (Barros et al. 2016; Rizzuto et al. 2017; Maxted, & Hutcheon 2018; Rebull et al. 2018; David et al. 2019). The *K2SFF* generated light curve is shown in Figure 5.7. All but Rizzuto et al. (2017) and Rebull et al. (2018) report a period of 9.2 days for the eclipsing binary component. Barros et al. (2016) reports a period of 4.59876 days, half of the other reported periods, while Rebull et al. (2018) do not report any period for the eclipsing binary. Both Rebull et al. (2018) and Maxted, & Hutcheon (2018) report a 0.9 day period for the pulsations of the bright component.

Maxted, & Hutcheon (2018) and David et al. (2019) report a primary eclipse depth of ~ 0.43 mag, while Rizzuto et al. (2017) report a depth of 0.174 mag and Barros et al. (2016) report a depth of 19.2%. The depths reported by Maxted, & Hutcheon (2018) and David et al. (2019) are in good agreement with the depth reported by (Wraight et al. 2011) and the *K2SFF* light curve, and so a primary eclipse depth of ~ 0.43 mag is taken to be the fiducial value. This value is equivalent to a depth of 32.7%.

The star is contaminated by one field star in the halo and two field stars just outside of the halo, all G $\sim$ 16 (Figure 5.8). This contamination makes it difficult to process with *halophot* as the strong variability of the bright target causes its

pixels to be heavily down-weighted compared to those of the contaminating field stars (Figure 5.9). The period of variability strongly agrees with the literature, but the primary eclipse depth is on the order of 5%, nowhere near the values from the literature and highlighting the significant dilution effects field stars can have when using this technique.

We next consider the case where we mask out the three contaminating stars and then process the target. The weights are now more strongly concentrated in the halo of the bright target as is normally the case with uncontaminated stars (Figure 5.10). The resulting light curve retains the same periodicity, but the depth is now on the order of 35%, in better agreement with the fiducial value.

We finally consider the case where we subtract out the two field stars outside of the halo by first fitting two-dimensional Gaussians using the process described in Chapter 3 (Figure 5.11). The residuals are evident in the resulting fluxmap and the weightmap indicates that the PSF removal was not entirely complete. The topmost field star is no longer weighted, but the bottom star is. Additionally, the contaminating field star embedded in the halo is now being weighted up where previously it was heavily down-weighted. The bright star itself is being weighted up now, but not to the extent that the masked version was. The resulting light curve is an improvement on the original, but the eclipse depth does not match the result of the literature. The depth here is on the order of 25%, suggesting that the halo field star and residuals from one of the PSF-subtracted field stars are still diluting the signal from the bright target. These issues with the PSF removal are discussed further in the next chapter.

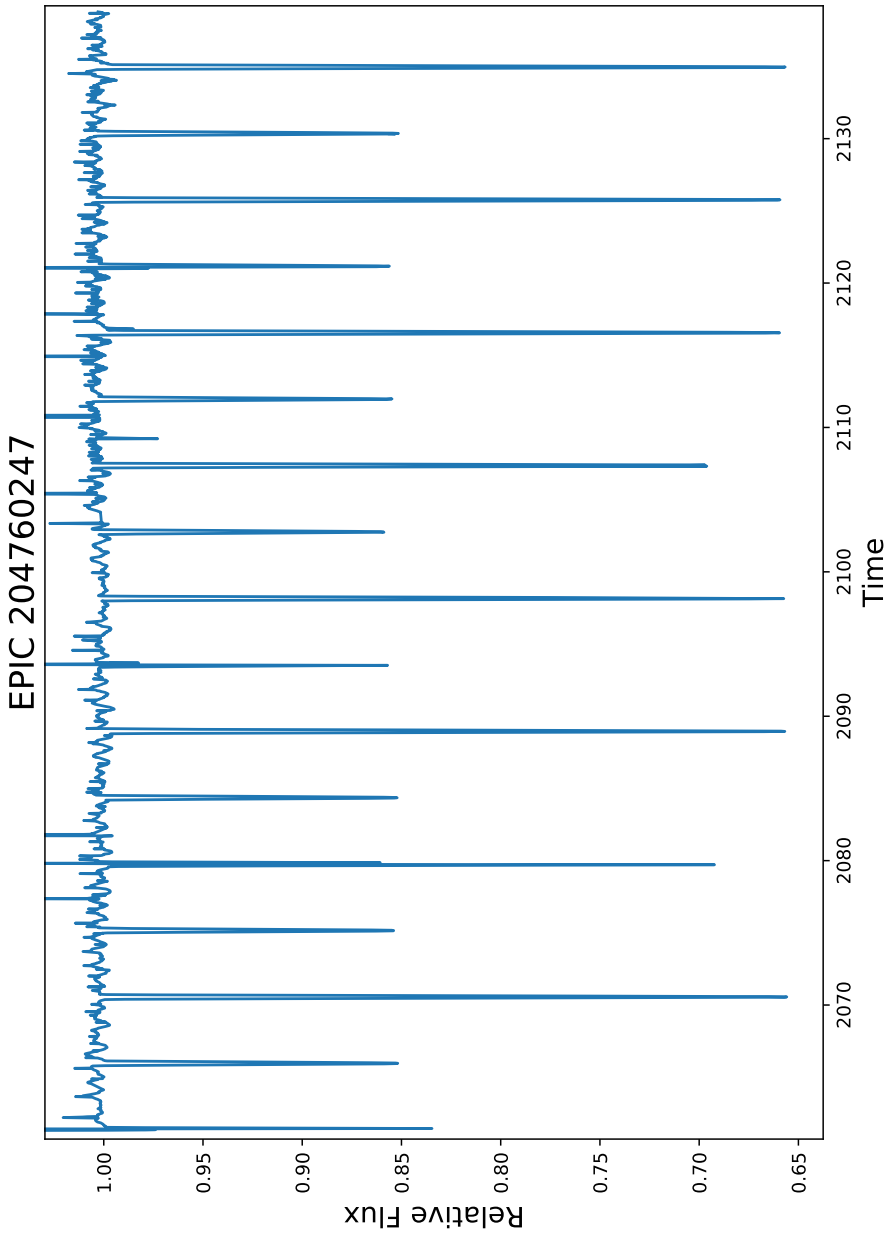

Figure 5.7: SFF light curve for EPIC 204760247

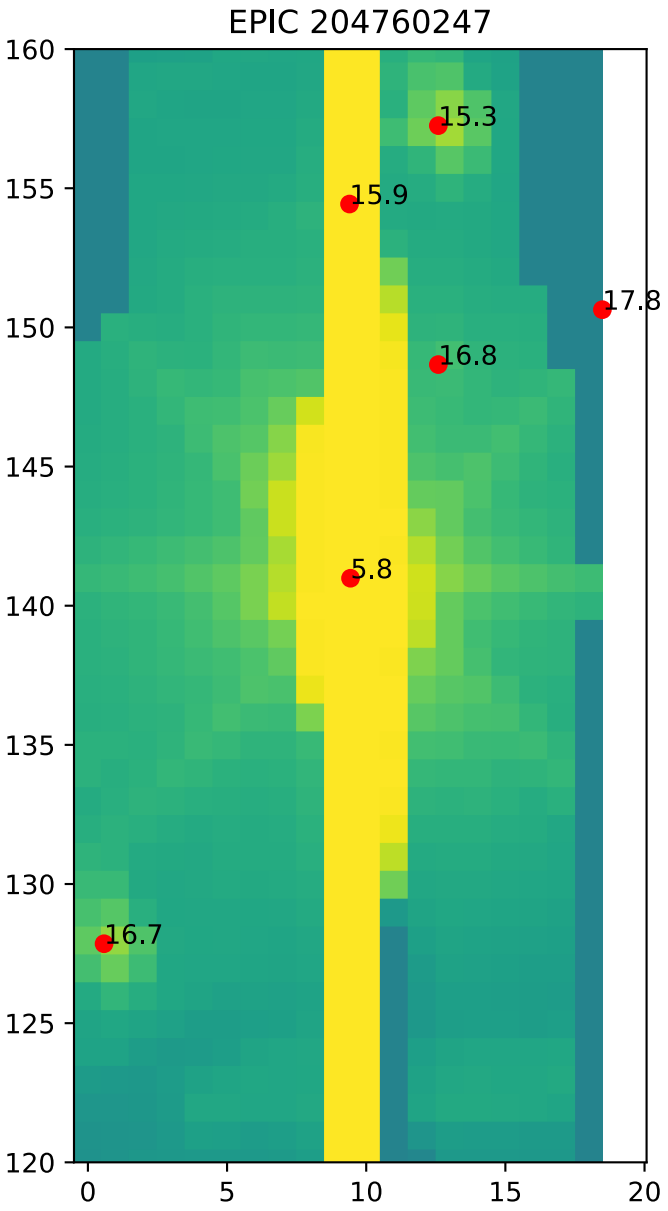

Figure 5.8: Gaia objects in and immediately around the halo. Darker green pixels are nan values reassigned to the median flux value

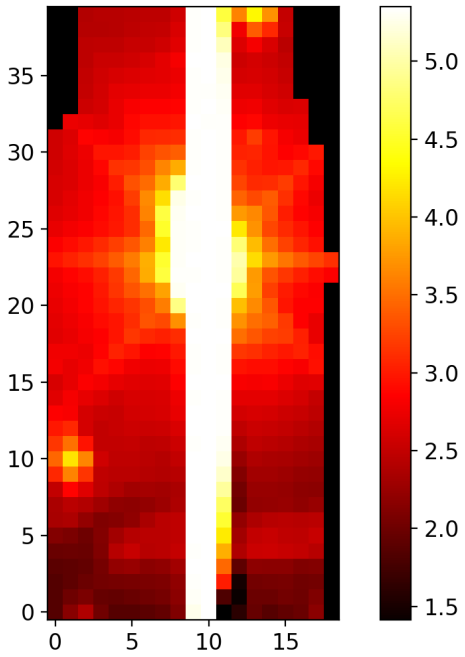

(a) Flux map

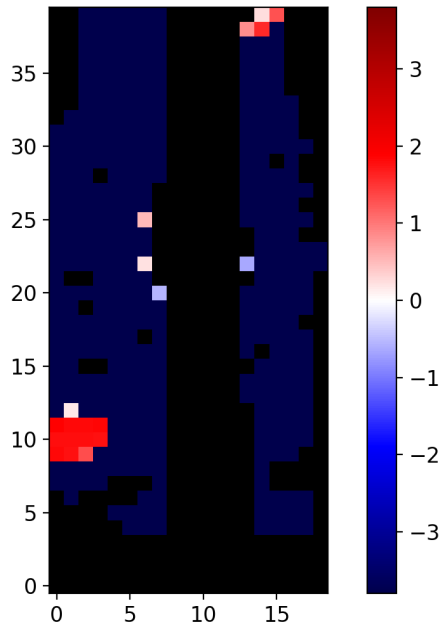

(b) Weightmap

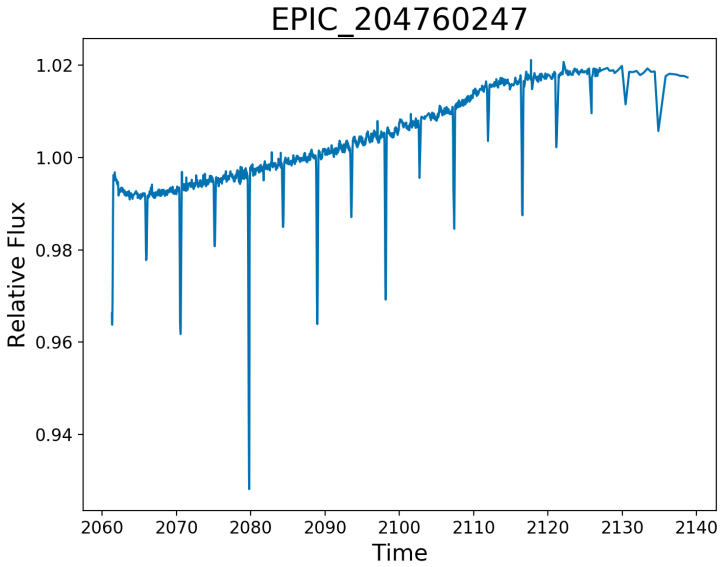

(c) Unflattened light curve

Figure 5.9: *Halophot* results for EPIC 204760247 with the contaminating field stars included

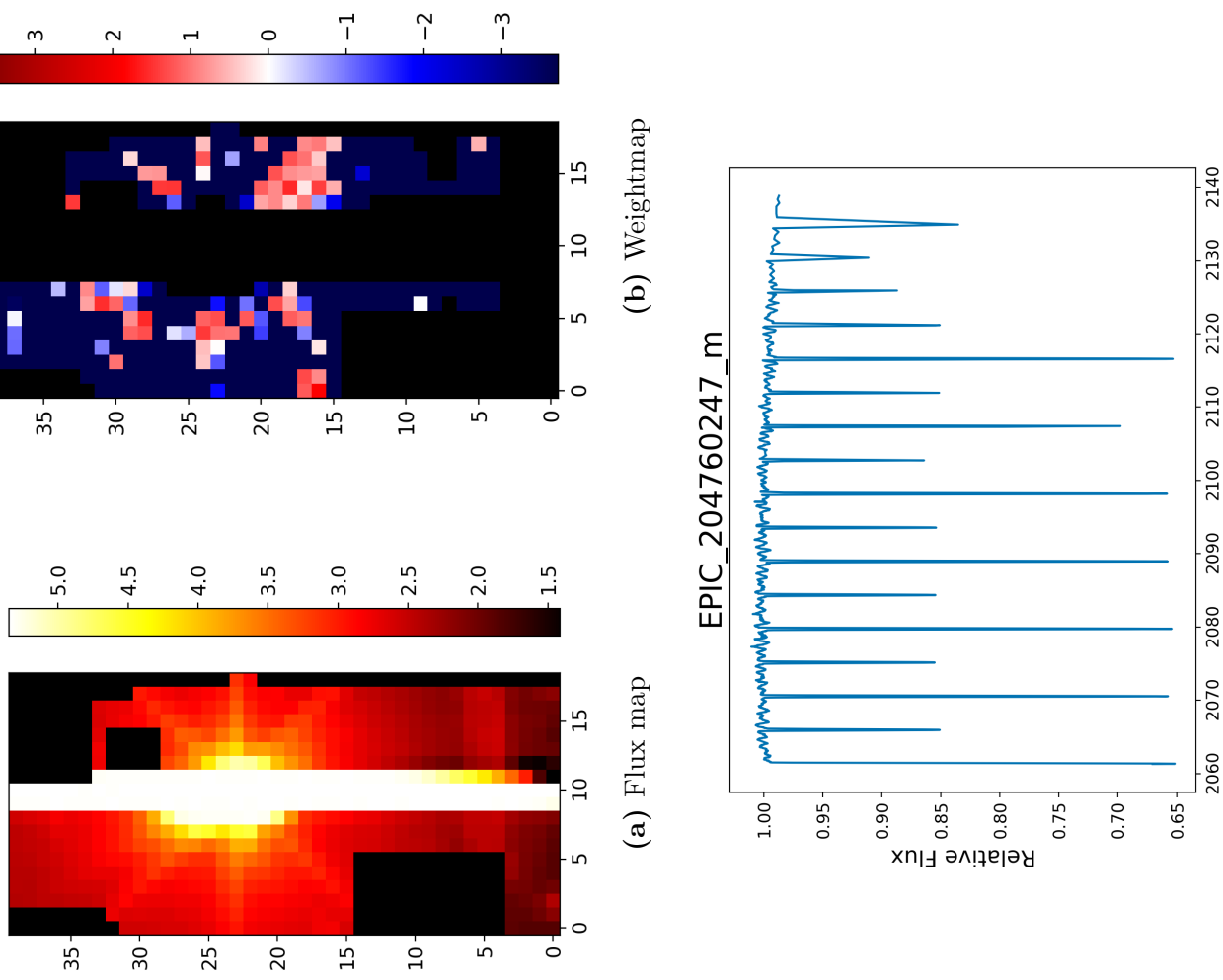

(a) Flux map **(b)** Weightmap **(c)** Unflattened light curve

Figure 5.10: *Halophot* results for EPIC 204760247 with contaminating field stars masked

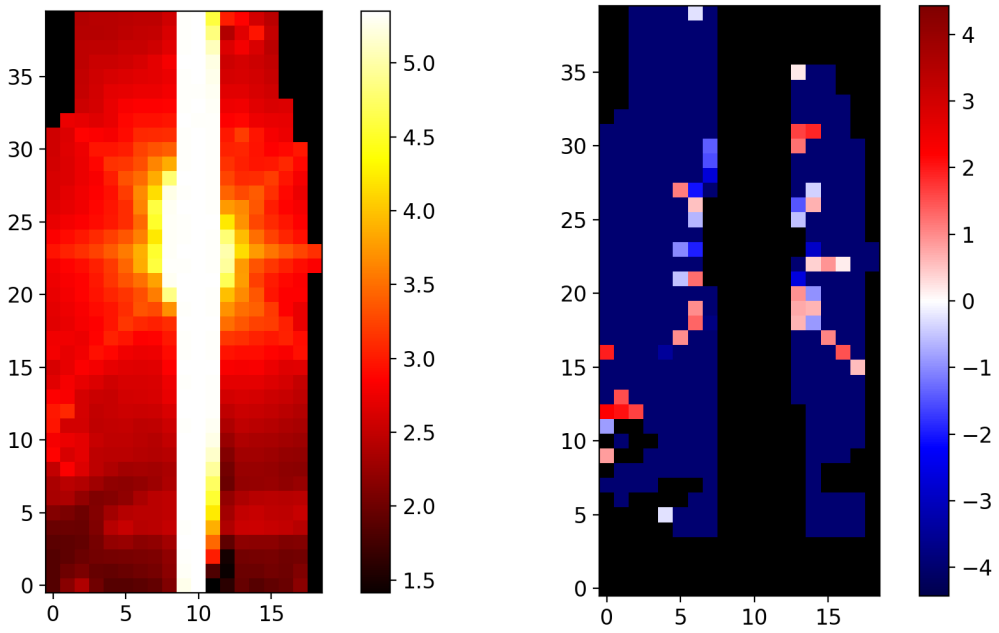

(a) Flux map

(b) Weightmap

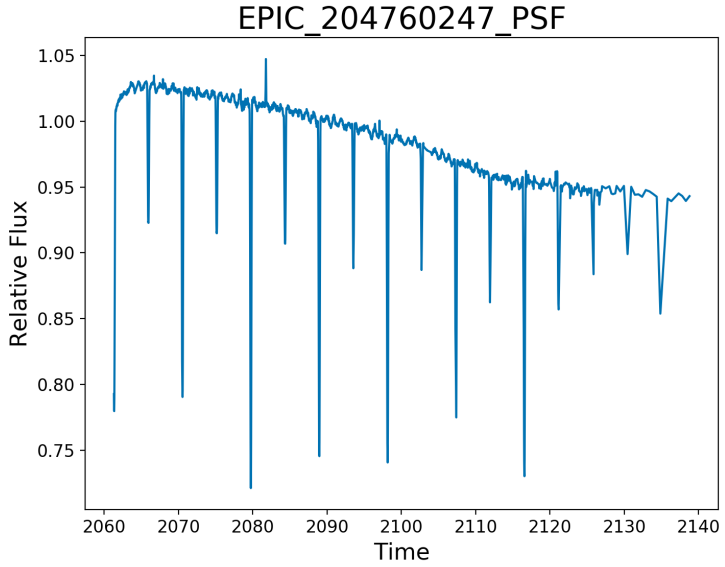

(c) Unflattened light curve

Figure 5.11: *Halophot* results for EPIC 204760247 with the two field stars outside of the halo PSF-subtracted

Chapter 6

Discussion

6.1 Finding Planets

As noted in the previous chapter, we do not detect any promising planetary candidates in the sample of 603 uncontaminated bright targets. We still have the sample of 360 contaminated bright targets to process, as well as potentially the thousands of field stars in the fields of view of those 360 targets.

The current result of no detections is disappointing but not entirely unexpected. According to NASA's Exoplanet Archive, the *K2* mission has led to the detection of 1737 candidate and confirmed exoplanets around 987 stars. These 987 planet-hosting stars are from a total of 210614 stars that have been observed and have data available according to VizieR catalog. If we apply this probability of a star hosting a detectable planetary system to a random sample of 603 stars, the expected number of detected planets is 2.82. However, our sample is not random, as it is biased towards early type and evolved stars. The majority of planets detected by *K2* orbit later type stars (Figure 6.1). As such, the expected number of detected planets will be lower.

This does not imply that detecting a planet around one of the bright stars in our sample is impossible. Planets are more common around early-type stars than later type (Johnson et al. 2010), but not more commonly detected. Nonetheless,

planets orbiting giant stars have been detected using *K2* (Grunblatt et al. 2016, 2017; Jones et al. 2018), as have planets around F dwarfs (Barragán et al. 2016; Rodriguez et al. 2017).

Planets have also been detected around stars as early as A0 using the Kilodegree Extremely Little Telescope (KELT), which uses two small ground-based robotic telescopes to search for planets orbiting bright stars (Pepper et al. 2007). KELT has detected two planets around A0 stars - KELT-9b (Gaudi et al. 2017) and KELT-20b (Lund et al. 2017), both of which are hot Jupiters.

Of the 360 contaminated stars in our sample, 106 are A0 dwarfs or later, with 74 being F0 or later. In the next section, I discuss the transit injection retrieval tests we use to determine the effectiveness of *halophot* for detecting exoplanets.

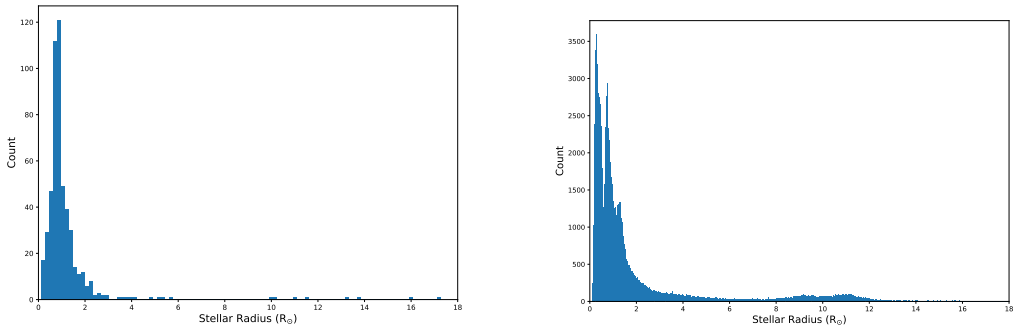

Figure 6.1: Histogram of stellar radius for candidate/confirmed host stars (left) and all K2 stars (right).

6.1.1 Transit Injection & Retrieval

In order to test *halophot's* transit detection capabilities, I inject transits into the targets at the pixel level. For the results shown here, I use the target EPIC 220429217 (HD 4628), a bright (Kp = 5.74) K2.5V star observed in Campaign 8. The star shows little variability (Figure 6.2) and has a stellar radius smaller than the Sun, making it ideal for transit injection retrievals. I use BATMAN to generate the transits, using the mean solar density to determine the scaled semi-major axis and Sun's quadratic limb darkening parameters. I sample periods of 0.5, 1, 2, 5, 10, and 20 days and $R_p/R_\star$ values of 0.01, 0.02, 0.03, 0.05, 0.1, and 0.2.

The results of the BLS search for transit signals of some of the injections are shown (Figures 6.3, 6.4, 6.5). The periods can be recovered consistently for $R_p/R_\star$ values greater than 0.03, and occasionally recovered for values less than or equal to that. For a sun-like star, a value of $R_p/R_\star = 0.03$ corresponds to a 3.3 $R_\oplus$ planet.

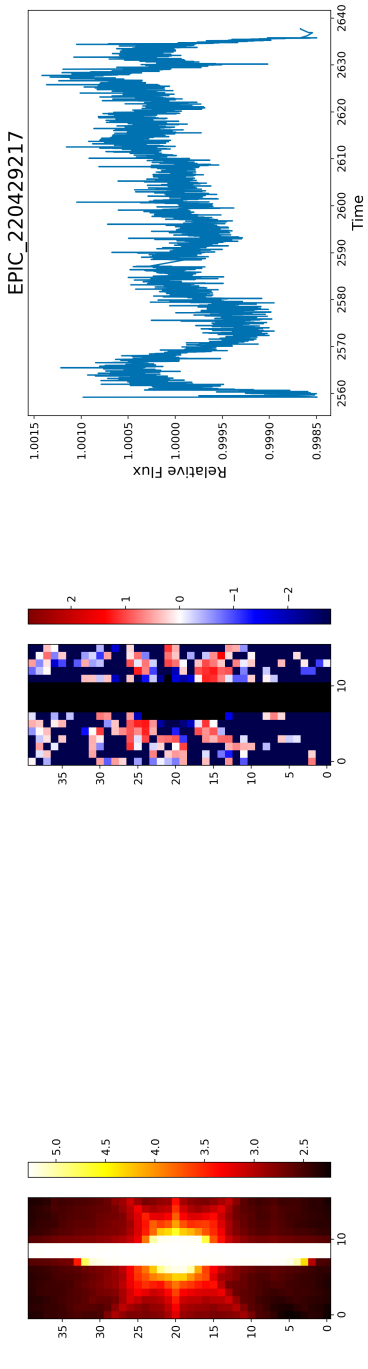

Figure 6.2: EPIC 220429217 flux map, weightmap, and unflattened light curve, pre-injection.

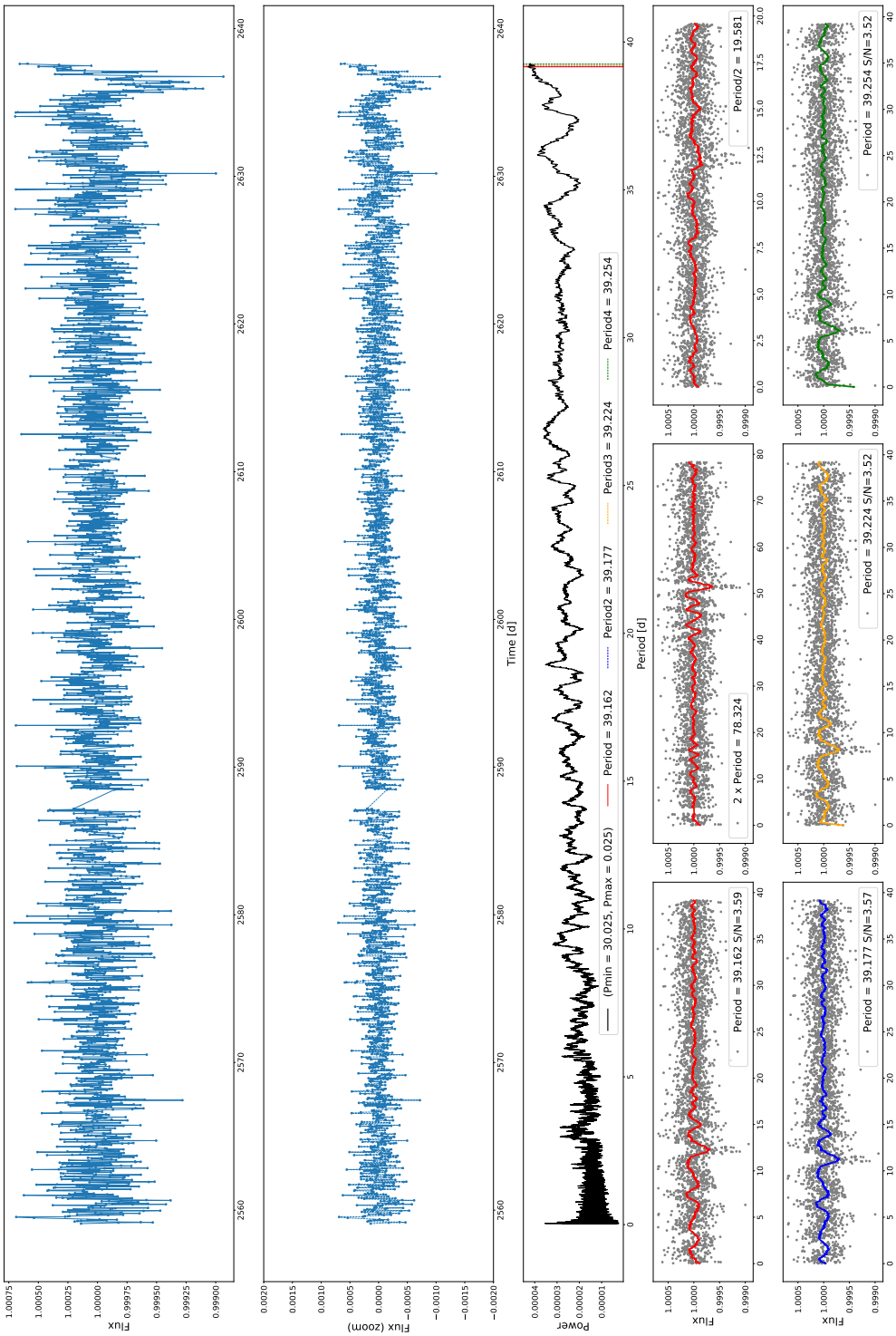

Figure 6.3: P = 10 days, $R_p/R_\star = 0.01$. Neither the period or depth are recovered.

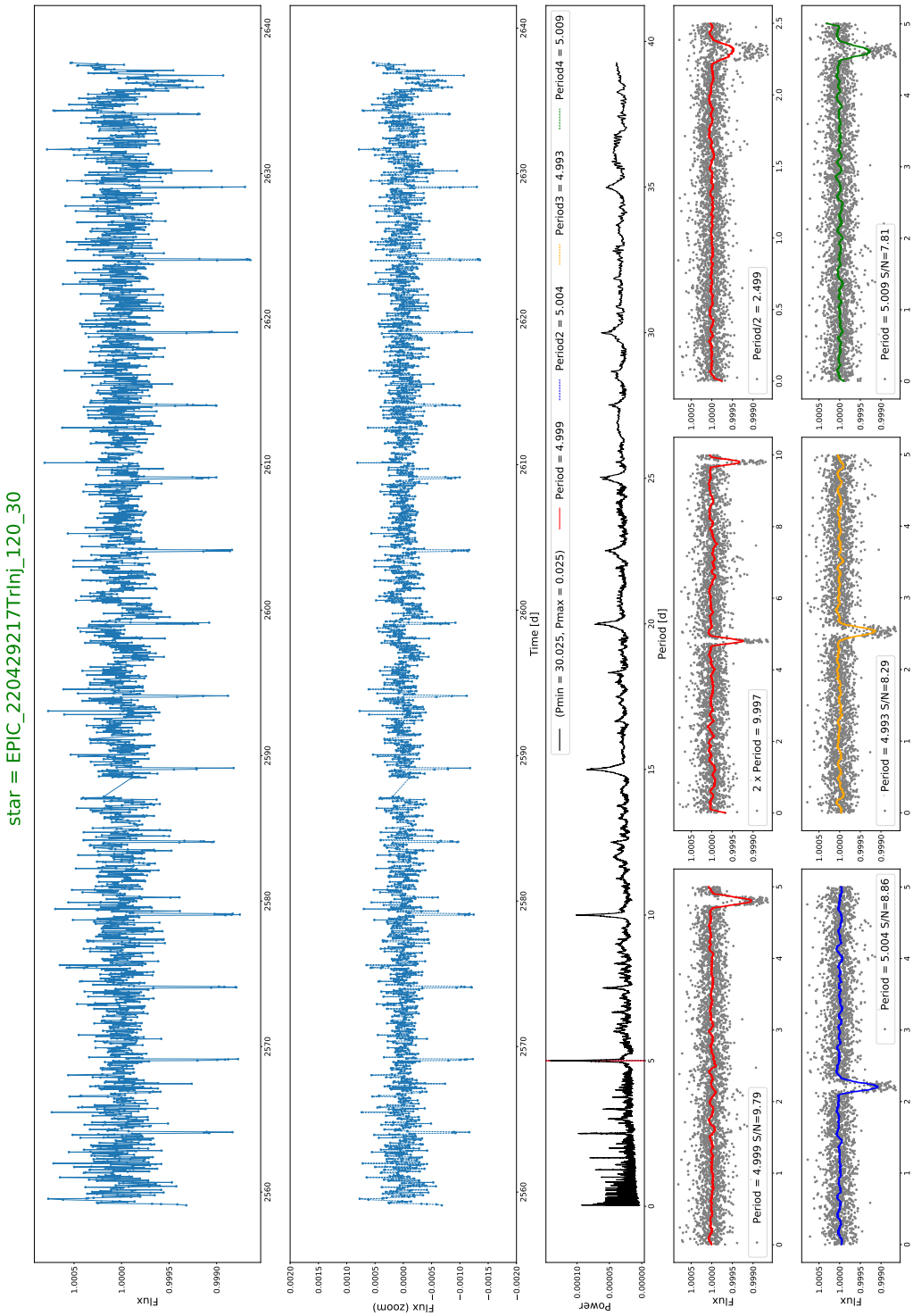

Figure 6.4: P = 5 days, $R_p/R_\star = 0.03$. Both the period and depth can be recovered.

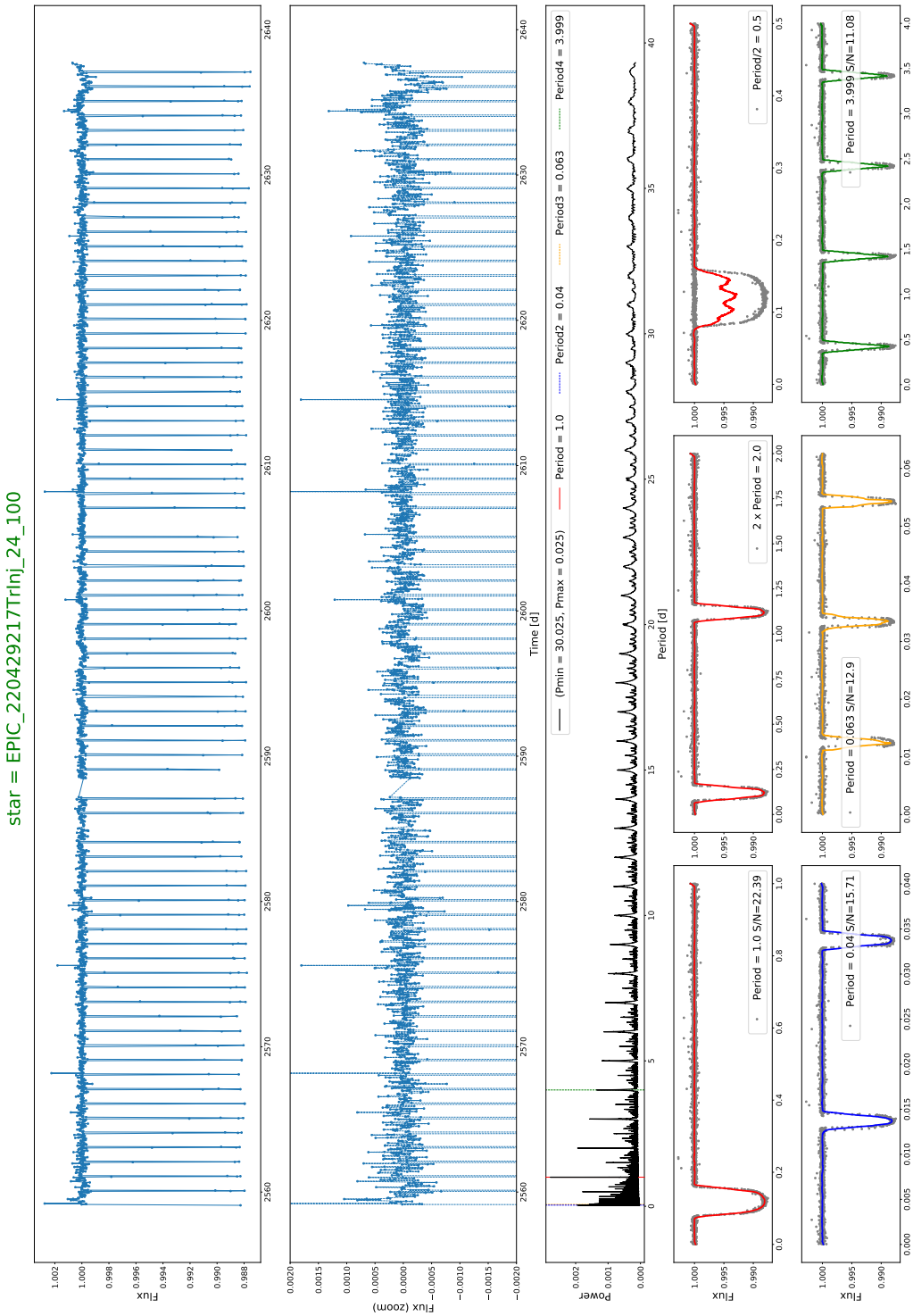

Figure 6.5: P = 1 day, $R_p/R_\star = 0.1$. Both the period and depth are easily recovered.

6.2 Ultra Short Period Variable Stars

As demonstrated in the previous chapter, *halophot* has proven effective for studying stellar variability. However, when examining results from the uncontaminated sample, a few targets took a noticeably longer time to be processed and produced anomalous weightmaps. The weightmaps of these targets were very similar to those of many of the contaminated bright targets, where the bright target's pixels are heavily downweighted. There were no nearby field stars however. When looking up these stars, I found that many of them were variable stars with very short periods, on the order of hours. Below, I discuss two classes of variable stars that exhibit these peculiar weight distributions - δ Scuti and β Cepheid stars.

6.2.1 δ Scuti Variables

δ Scuti variables are A0 to F5 members of the main sequence or giant branch that undergo very short period pulsations (Breger 2000). They lie in the instability strip, a region in the HR diagram where stars are unstable to changes in opacity and undergo pulsations (Figure 6.6). The pulsations are driven by the κ-mechanism of ionized helium. The periods of the pulsations are typically shorter than a day, and the amplitude can be as much as 0.1 mag. Their *Kepler* and *K2* light curves have been previously studied (Uytterhoeven et al. 2011; Paunzen et al. 2017) and planets have been found to be transiting them, including WASP-33b (Collier Cameron et al. 2010).

For the shortest period pulsations, the weightmaps are dominated by a few pixels split mostly evenly to the left and right of the saturated columns (Figure 6.7). Interestingly, for the longest period stars, the weightmaps are not dominated

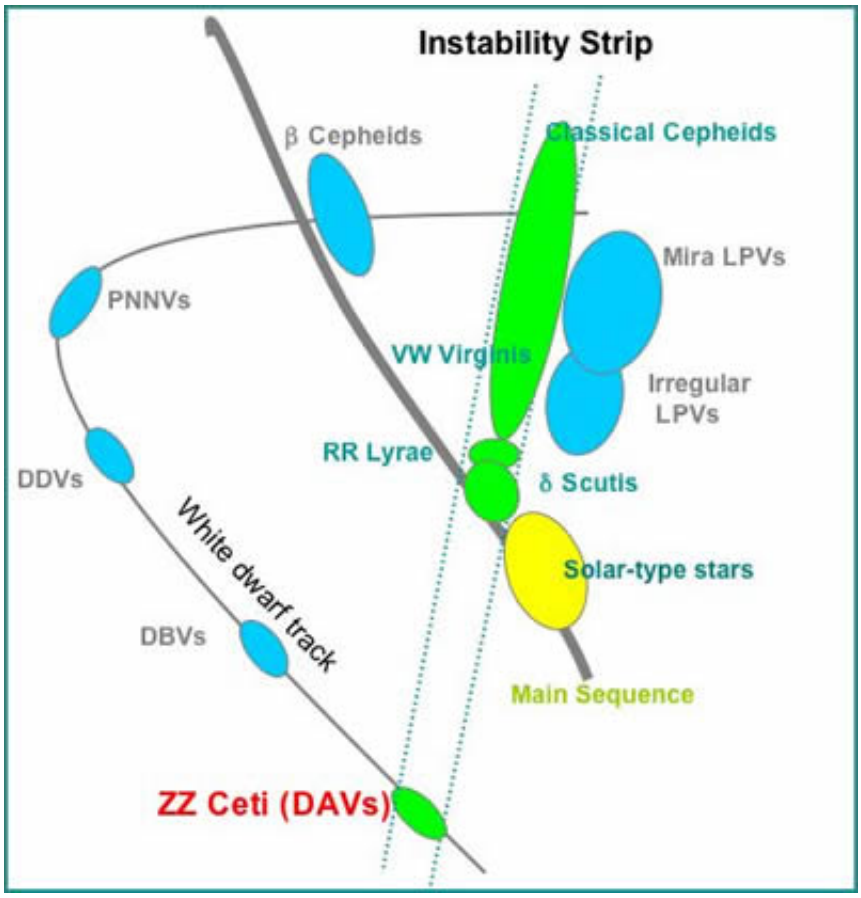

Figure 6.6: HR diagram showing the relative positions of different variable stars. Note β Cepheids lie outside of the instability strip, which is the region between the two dotted lines. Source: Swinburne University of Technology

by outliers and are instead more evenly distributed.

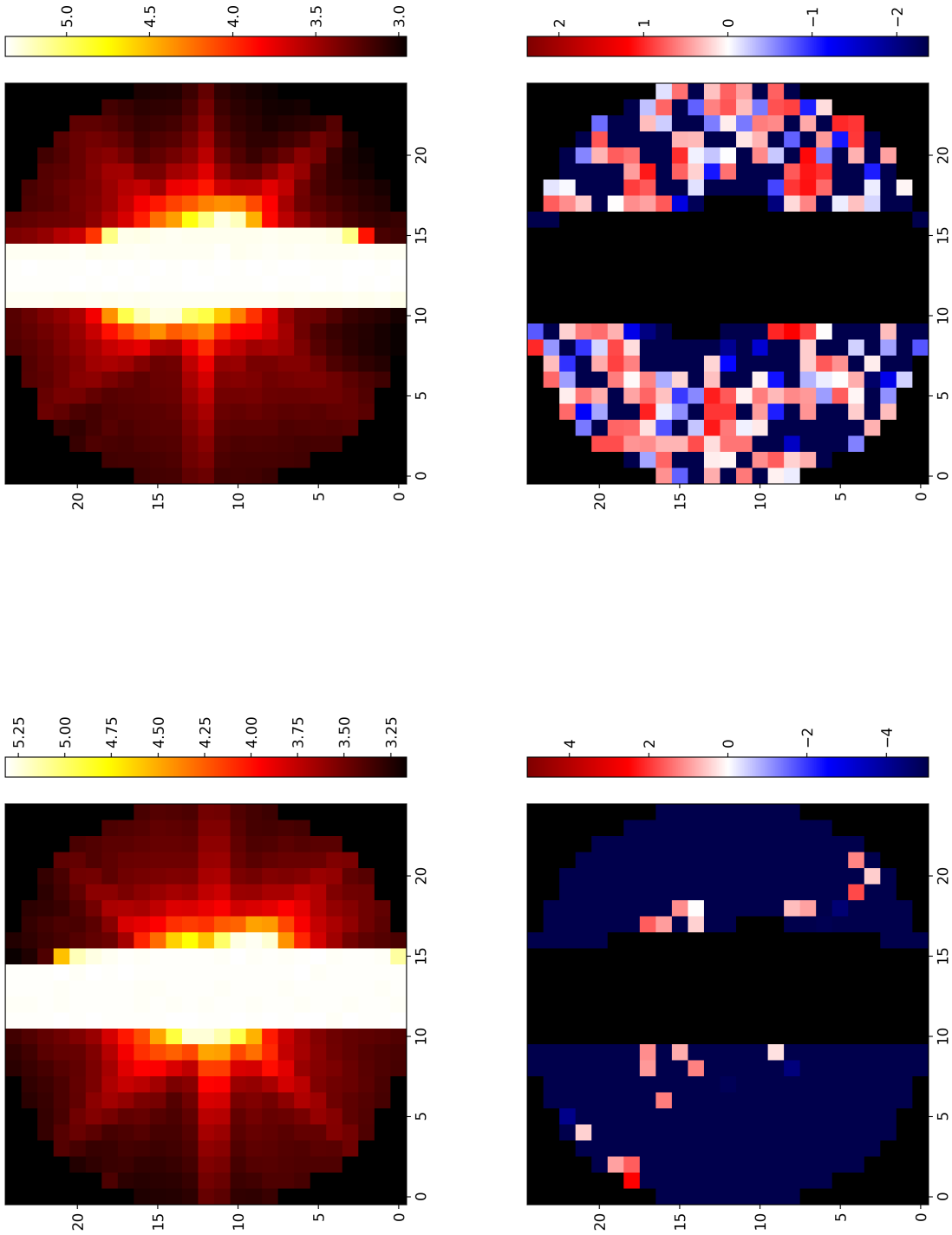

(a) P = 3 hours **(b)** P = 30 hours

Figure 6.7: *Halophot* results for two δ Scuti variable stars EPIC 200173880 (left) and 200173883 (right).

6.2.2 β Cepheid Variables

β Cepheid variables are B type stars that undergo pulsations like δ Scuti variables, in which the period of the pulsations is on the order of hours. Unlike δ Scuti variables, however, they do not lie in the instability strip and the pulsations are not driven by the opacity of ionized helium. Instead, they are driven by κ-mechanism of metals deep in the interior of the star (Moskalik, & Dziembowski 1992). The typical fluctuations are on the order of 0.01 to 0.3 mag.

Figure 6.8 shows the flux maps and weightmaps for two β Cepheids in our sample of uncontaminated bright targets - EPIC 200128906 (HD 157056) and EPIC 200213067 (Spica). A search of the literature lists the period of pulsation of EPIC 200128906 to be 3.4 hours (van Hoof 1957). The pulsation period of EPIC 200213067 is listed as 4.17 hours, although its variations were noted to have declined in the 1970s (Lomb 1978). Spica is also known to be part of a compact binary, showing ellipsoidal variations consistent with the orbital period of 4 days (Shobbrook et al. 1969).

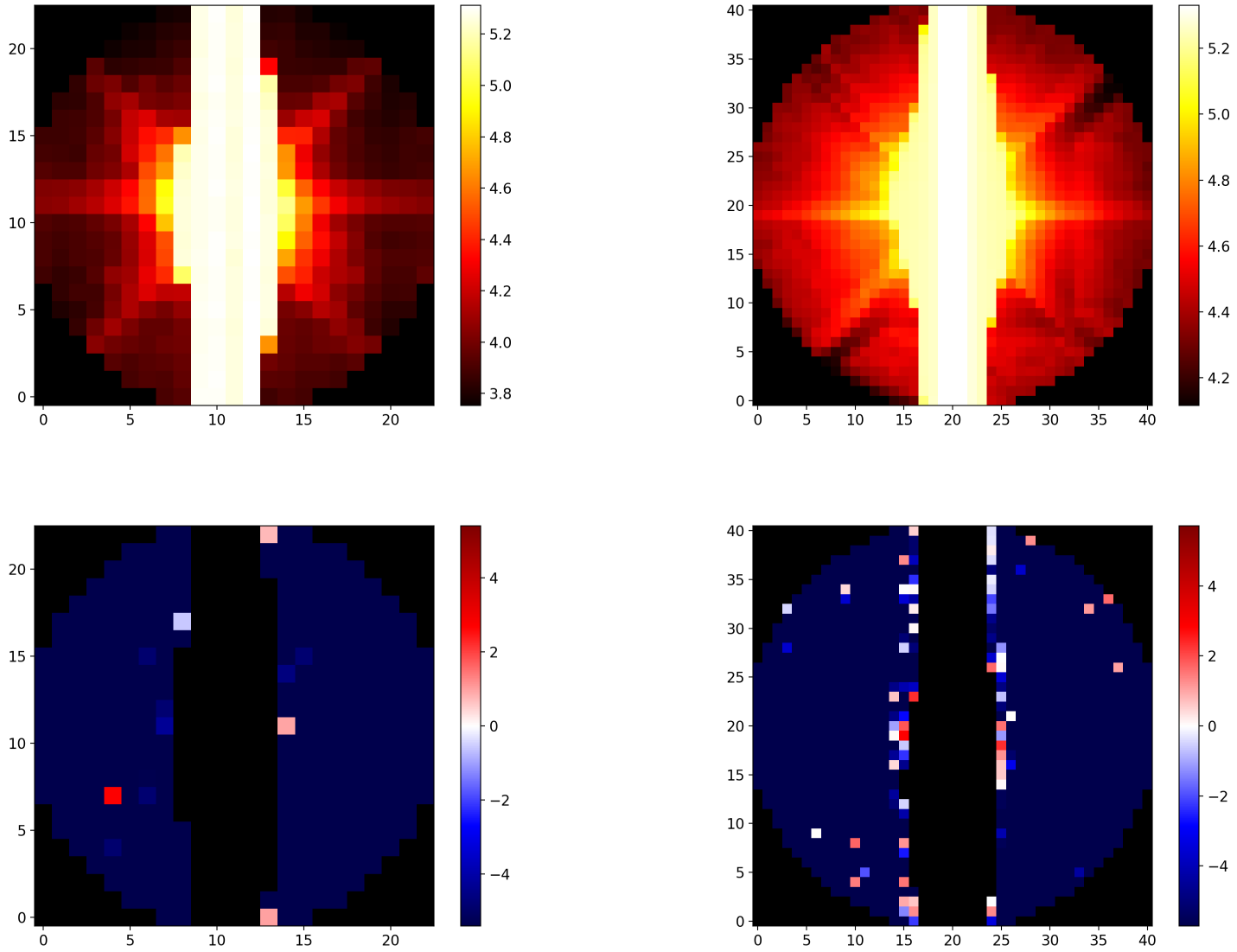

(a) P = 3.7 hours

(b) P = 4.17 hours

Figure 6.8: *Halophot* results for two β Cepheid variable stars EPIC 200128906 (left) and 200213067 (right).

6.2.3 Signal Injection

In order to examine how the distribution of the weights change with the period of the variability, I inject a variable signal into a target with no known variability (Figure 6.9). I choose the target EPIC 200213058 (HD 116831), a bright (V = 5.97) A8V star observed in Campaign 17. While a simple sinusoidal function can be injected, I use the implicit function below in order to more closely model the rapid increase and slow decrease in flux associated with δ Scuti variables,

$$y = sin\Big(\frac{2\,\pi t}{P} + \frac{y}{n}\Big),$$

where y is the fractional change in flux. This function is periodic but has a sharper increase in flux than decrease (Figure 6.10). I solve for the values of the function using *scipy.optimizer.fsolve* at each point of time t. I sample periods from 1 to 24 hours at 1 hour steps, as well as periods of 2, 5, 10, 15, 20, 25, 30, 35, and 40 days. The amplitude of the signal is sampled at 0.1%, 0.5%, 1%, and 10% of the pixel flux.

Figure 6.11 shows examples of weightmaps for periods of 1, 6, 24, and 240 hours at an amplitude of 1%. The weightmaps for 24 and 240 hours are qualitatively similar to the weightmap of the pre-injected target, suggesting the weightmaps stabilize at around 24 hours. I examine the distribution of the weights for different periods, as well as their mean value and standard deviations. The distribution for short periods are clustered at lower values than longer periods, suggesting that the weights in this scenario are dominated by a few outliers (Figure 6.12). Both the median weight value and standard deviation settle towards the values from the pre-injection image, although there is a strong dependence on the amplitude

of the signal (Figure 6.13). Larger amplitudes take longer to settle than smaller amplitudes. This is a result of the total variation being larger for a star with a larger amplitude signal. The results are consistent with what is seen with the weightmaps, as they become more and more similar to the pre-injected one as the period gets larger.

Next I examine whether the different distribution of weights results in different light curves. I test this by running the flattened light curves through BLS and comparing the periods returned with the periods injected. I find that I can recover periods for 121 of the 132 scenarios, defining a recovery to be when the injected period is within 10% of one of the four periods returned by BLS. Three of the failed recoveries occur for injected periods of 6 hours, the same period as the thruster firings. In all three cases, however, one of the best periods was 18 hours, an integer multiple of our period. Four more failures occured for a period of 40 days, which is the period which would not allow for the viewing of two complete cycles. Two more failures occurred at 35 days for amplitudes of 0.1% and 0.5%. The final two occurred for an amplitude of 0.1% at periods of 2 and 20 days.

I can also examine the amplitudes returned, by using the smoothed phase-folded light curves generated (colored curves plotted over the data). We can define the amplitude of the injected signal to be the semi-amplitude of this curve. Defining a successful recovery to be when the injected amplitude is within 10% of the semi-amplitude of the smoothed light curve, I can recover all amplitudes for injected periods of one day or less. I can recover amplitudes for 0.5%, 1%, and 10% for periods of 2 days. No amplitudes are recovered for periods longer than this. This makes sense because our flattening algorithm smooths out long term variability, meaning I suppress signal from longer period injections. If we want to consider long term stellar variability, we instead use a spline filter with large bins.

I examine the noise in the residuals after subtracting out the model signal (Figure 6.14). The precision is weakly dependent on the period of the injected signal and strongly dependent on the amplitude. For amplitudes up to 1%, the precision is within an order of magnitude of the pre-injected light curve

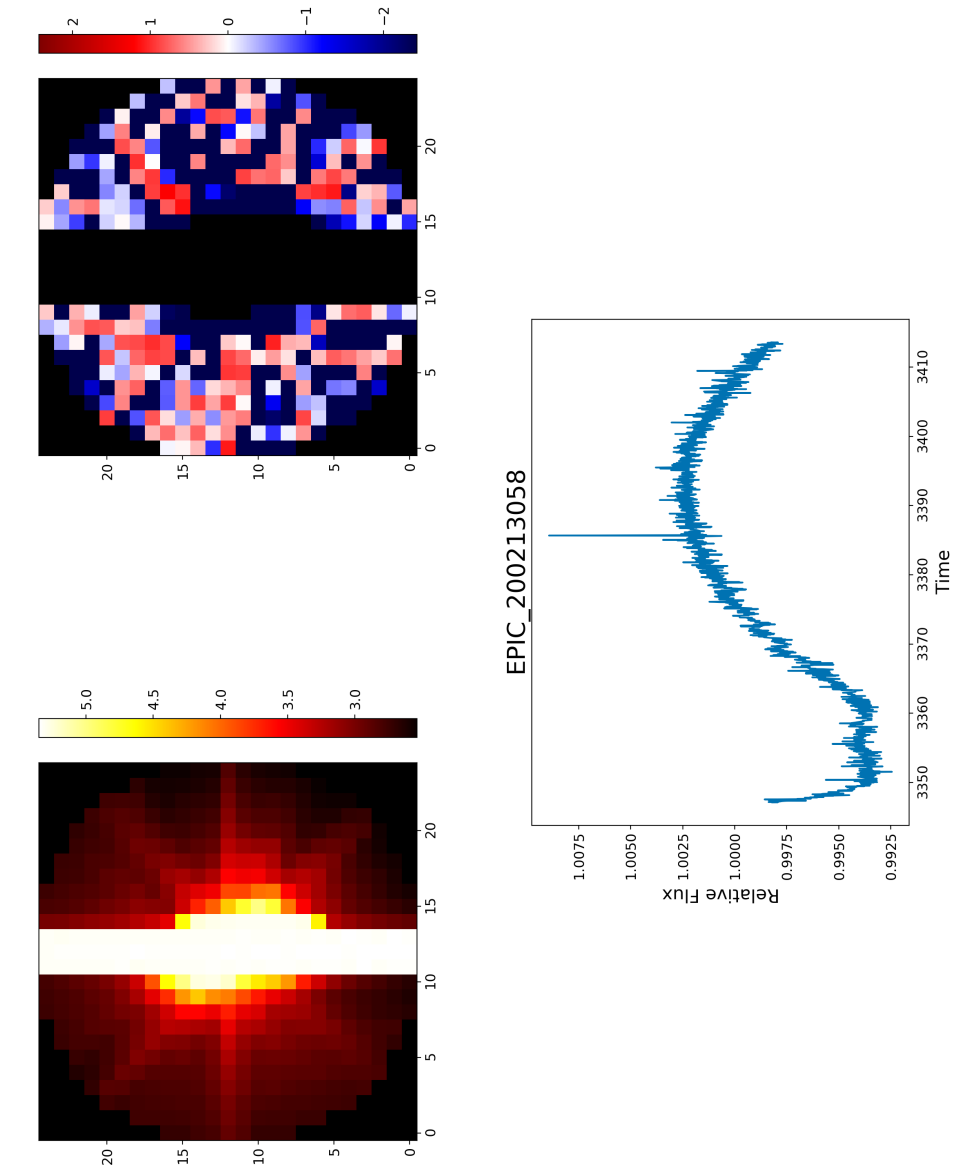

Figure 6.9: EPIC 200213058 flux map, weightmap, and unflattened light curve, pre-injection.

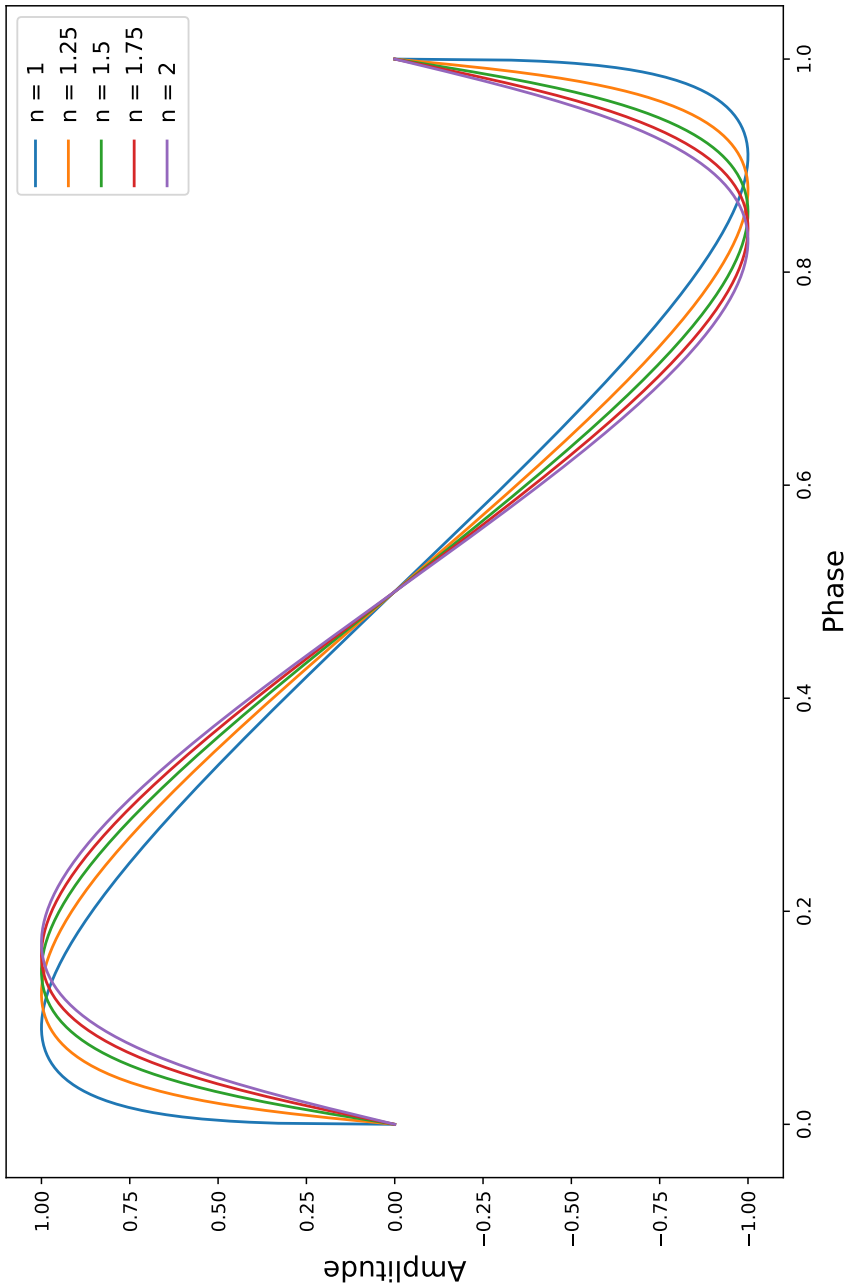

Figure 6.10: Model signal injected for various values of n. For values of n approaching 1, the function is multi-valued.

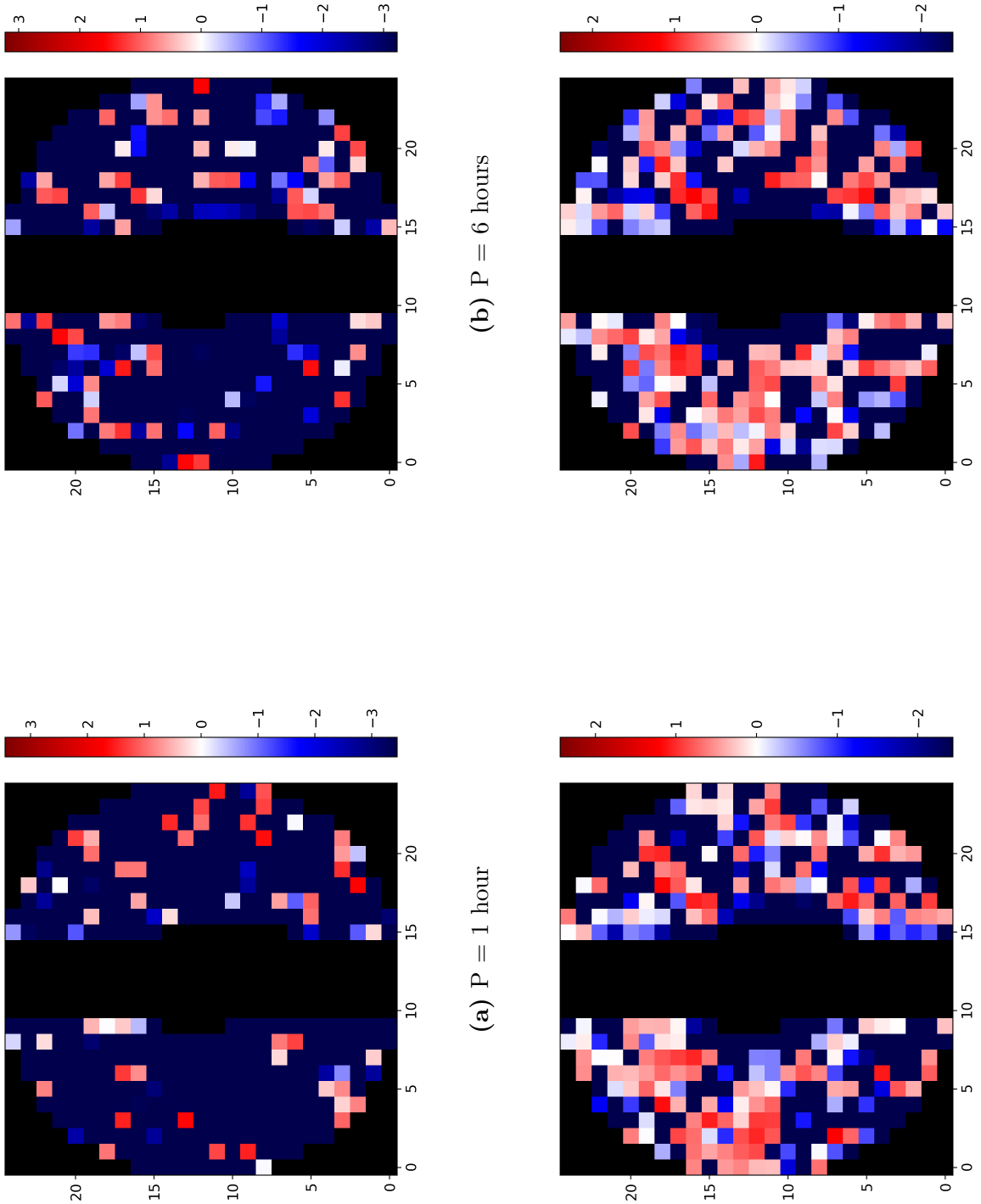

(a) P = 1 hour **(b)** P = 6 hours **(c)** P = 24 hours **(d)** P = 240 hours

Figure 6.11: Weightmaps for different injected periods for an amplitude of 0.01.

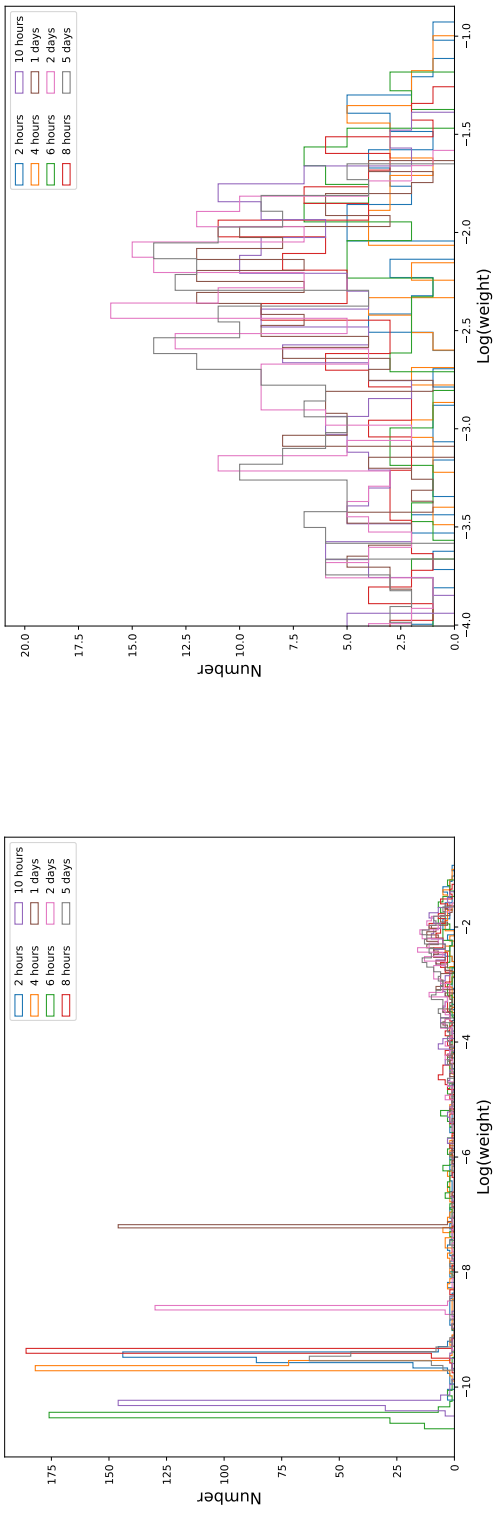

Figure 6.12: EPIC 200213058 weight histograms for selected periods and an amplitude of 1%. The histogram on the left covers the entire range of non-zero weights while on the right, we look at only the distribution of the largest weights.

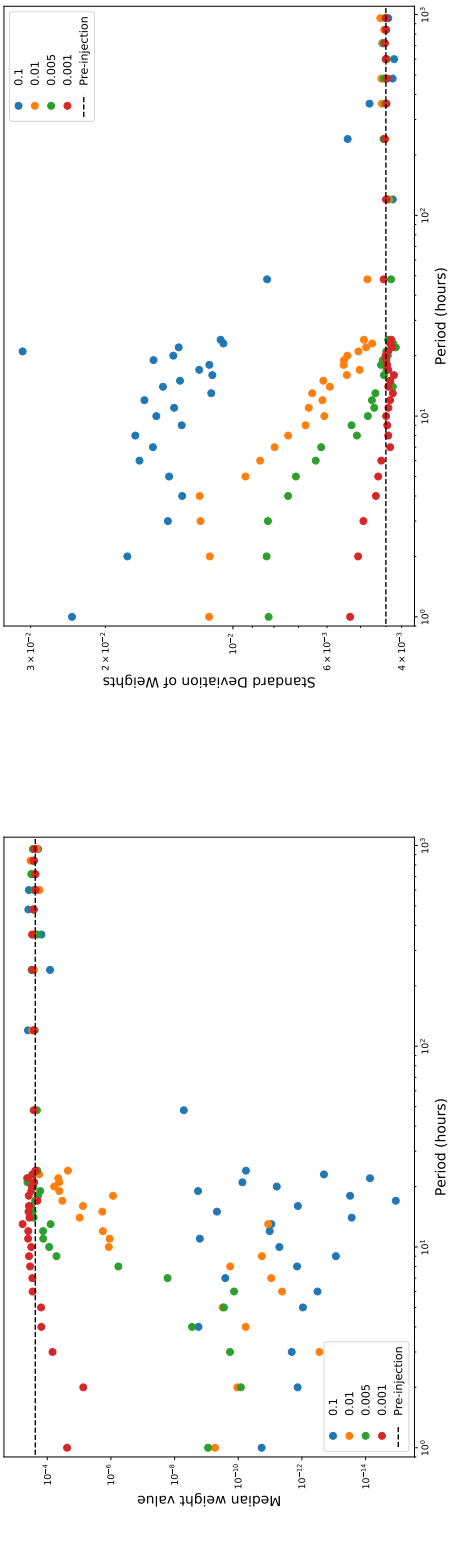

Figure 6.13: EPIC 200213058 signal injection median weight values (left) and standard deviation of the weight values (right). Values converge towards the preinjection values as the period of the injected signal increases, although smaller amplitude signals converge more quickly.

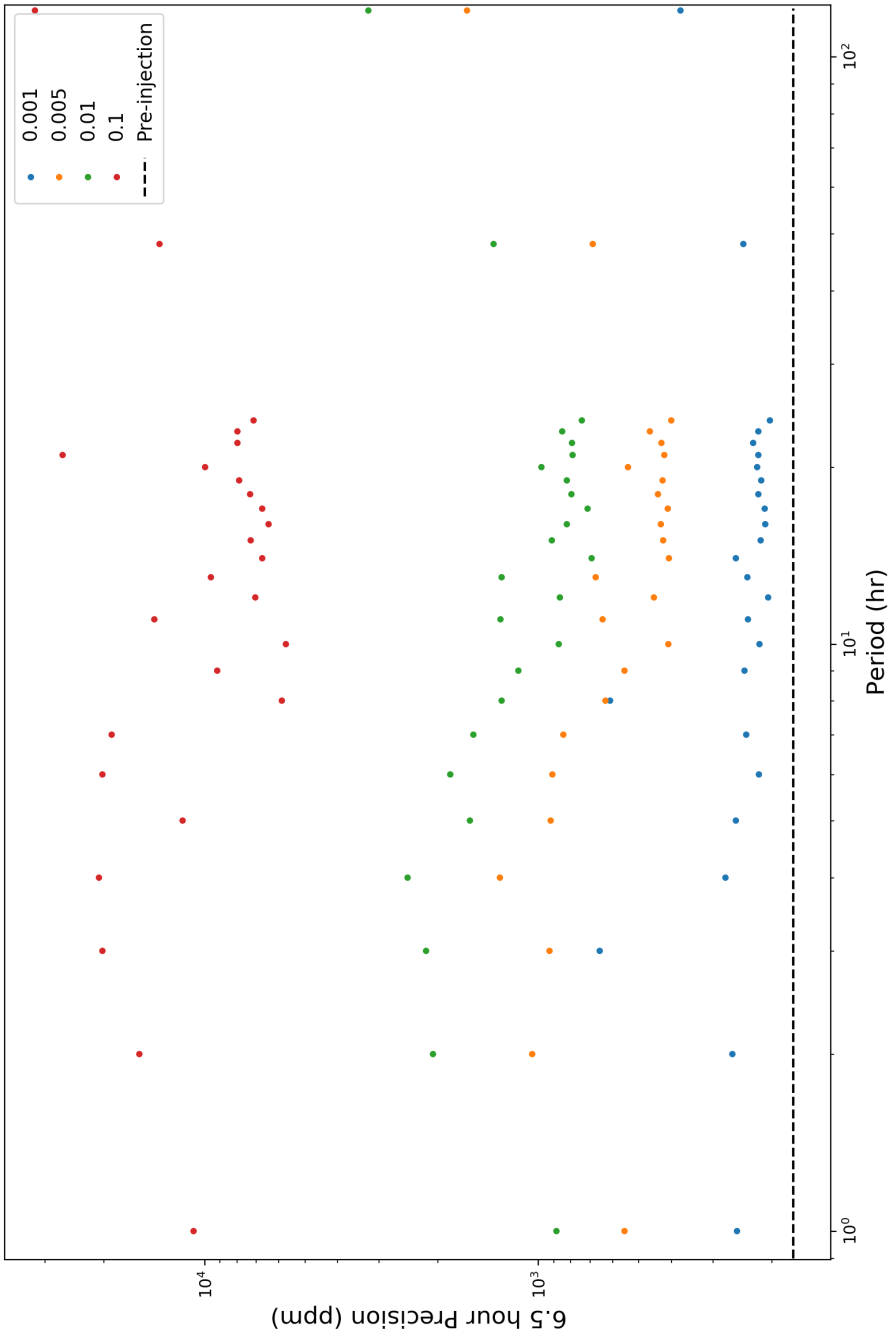

Figure 6.14: 6.5 hour precisions of various injection scenarios. The injected signal is removed by applying the same model used to generate it and the residuals are analyzed.

6.3 Contaminated Bright Stars

Halophot has proven very effective for uncontaminated bright stars, so long as any variability is not both strong and very short period. It is also effective for contaminated targets so along as there are only one or two faint field stars outside of the halo. Nonetheless, there are many scenarios where *halophot* and our PSF-removal algorithm are less effective, namely when there are either saturated field stars or a large number of fainter field stars in the field of view. Below I examine some of these cases, as well as examine the validity of using a two-dimensional Gaussian to model field stars.

6.3.1 EPIC 200173850

EPIC 200173850 (τ Tau) is a bright (V = 4.26) star that was observed in Campaign 13. As shown in Figure 6.15, there is a bright contaminating field star (V = 7.1) in the field of view. A two-dimensional Gaussian cannot be used to model the contaminating star due to the column bleeding, meaning the only way to attempt to extract the bright target's flux is to mask out the contaminating star. This can present a challenge, however, as there will be substantial blending of the flux from the two bright stars if they are close to one another. In the case of this target, the masking appears to be relatively effective in redistributing higher weights to the bright star, but many weights favor the remaining fainter field stars, which presents another issue.

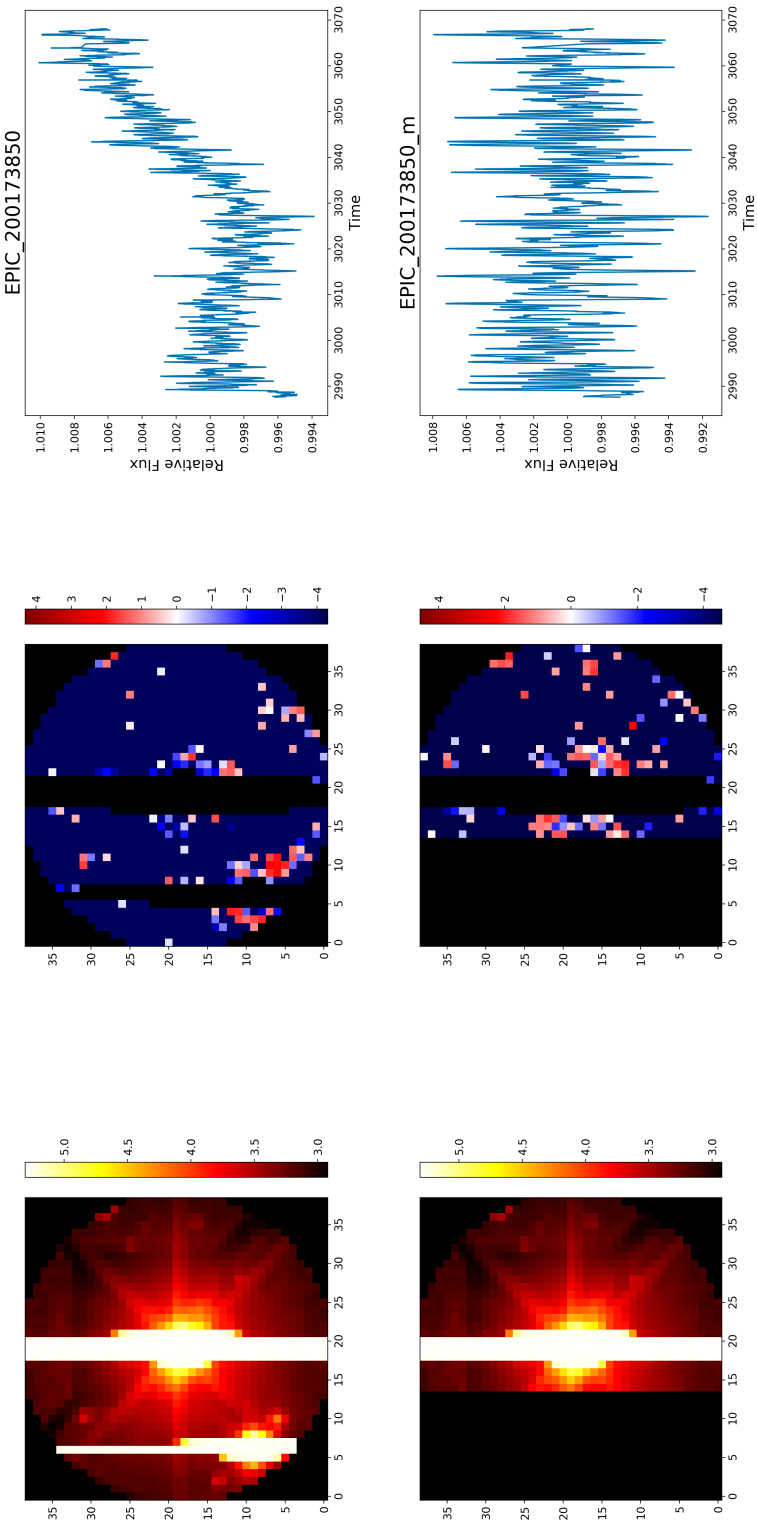

Figure 6.15: EPIC 200173850 flux map, weightmap, and unflattened light curve for original (top) and masked (bottom) images.

6.3.2 EPIC 200062584

When a bright target is contaminated by many field stars, it often becomes necessary to iteratively remove the stars until the the bright target's pixels are upweighted. In some cases, the large number of field stars makes this a very difficult task.

This is often the case for the bright targets observed in Campaign 7, which had *K2* pointing towards the galactic center. EPIC 200062584 (ψ Sgr) is a bright spectroscopic binary (V = 4.85) observed in this campaign. As can be seen in Figure 6.16, the star is contaminated by many faint field stars. Even after PSF-subtracting the three brightest field stars, the weights continue to favor the remaining field stars.

Bright targets from Campaign 7 may not be well-suited for this technique since they suffer from much greater contamination than targets from other campaigns. Iterative removal of field stars can eventually lead to a typical weightmap, but this iterative approach will result in the removal of a lot of the target's halo flux.

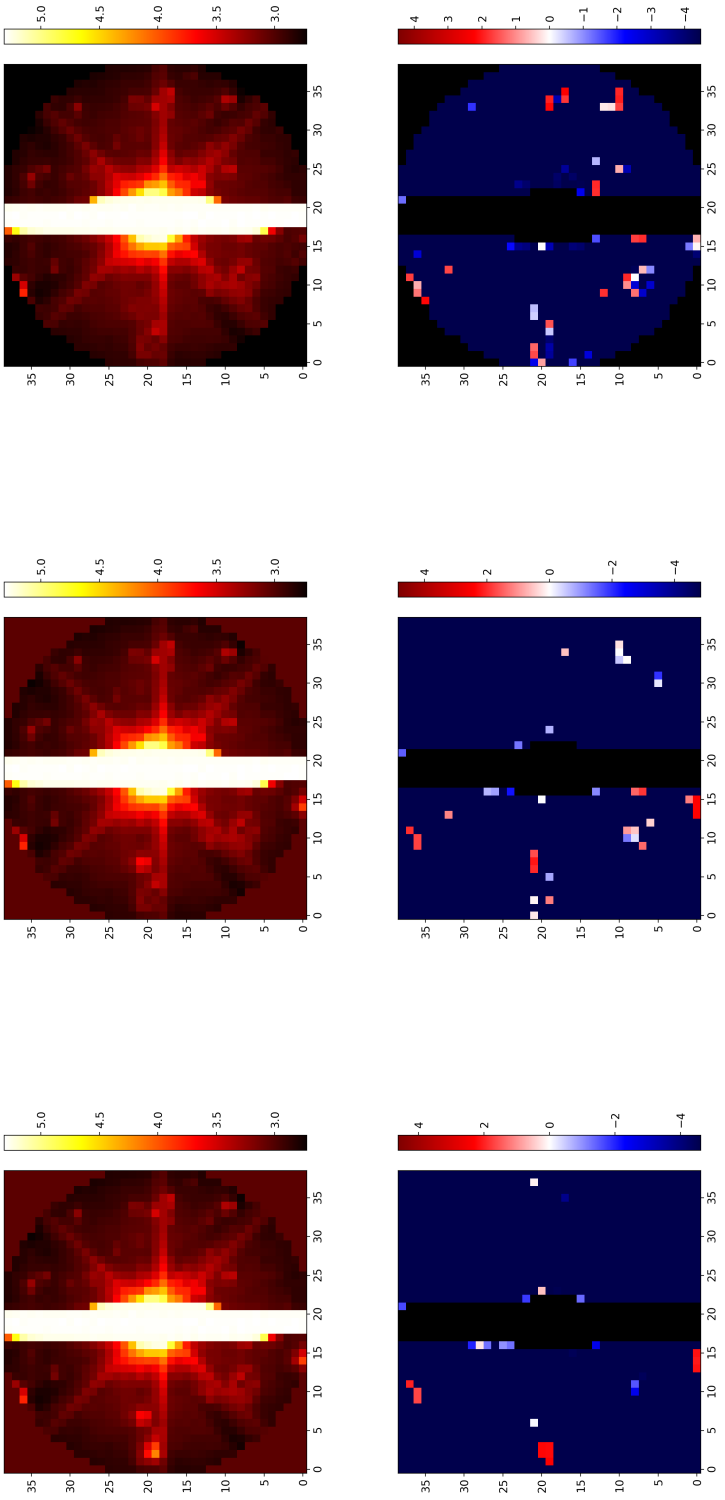

(a) Original **(b)** Brightest field star PSF-subtracted **(c)** Next two brightest stars PSF-subtracted

Figure 6.16: *Halophot* results for EPIC 200062584.

6.3.3 PSF Removal Issues

While a two-dimensional Gaussian can be used to successfully model a faint isolated star, it may not be well suited for other scenarios. One such scenario is a field star located in the halo of a bright star. Very faint stars can still impact the calculation of the weights, as can be seen for EPIC 204760247 (Section 5.2.2). The field star in the halo is not even visible in the flux map yet its effect can be seen in the PSF-subtracted weightmap. Since it blends with the halo, it cannot be modelled with a Gaussian. Even if a field star is substantially brighter than the halo, the flux in the halo falls off radially meaning the field star is not sitting on top of a constant background. This is more problematic for stars sitting on top of diffraction spikes, which have flux levels comparable to modestly bright field stars. Here, a Gaussian does not approximate the flux well and multiple iterations are needed to remove the field star. However, this iterative subtraction results in the removal of flux from the bright star, reducing the amount of signal.

I also study whether a two-dimensional Gaussian profile can correctly describe the PSF of brighter field stars. I have shown that for a faint (Kp = 15.733) white dwarf, I am able to recover the rotation period using the Gaussian model as our flux (Section 4.4.2). Here I look at four stars with Kp = 10, 12, 14, and 16 and determine the validity of a two-dimensional Gaussian PSF. In Figures 6.17 and 6.18, I show the Gaussian fit alongside the original data and the residuals. The Gaussian is generally a good fit for the center of the star, but can deviate from the edges. This is most apparent in the brighter targets. Thus, a two-dimensional Gaussian may not fully capture the PSF of bright field stars, meaning our removal of them will not be complete. As such, further work must be done to model these targets, whether it be with a modified version of our current fitting or a new PSF.

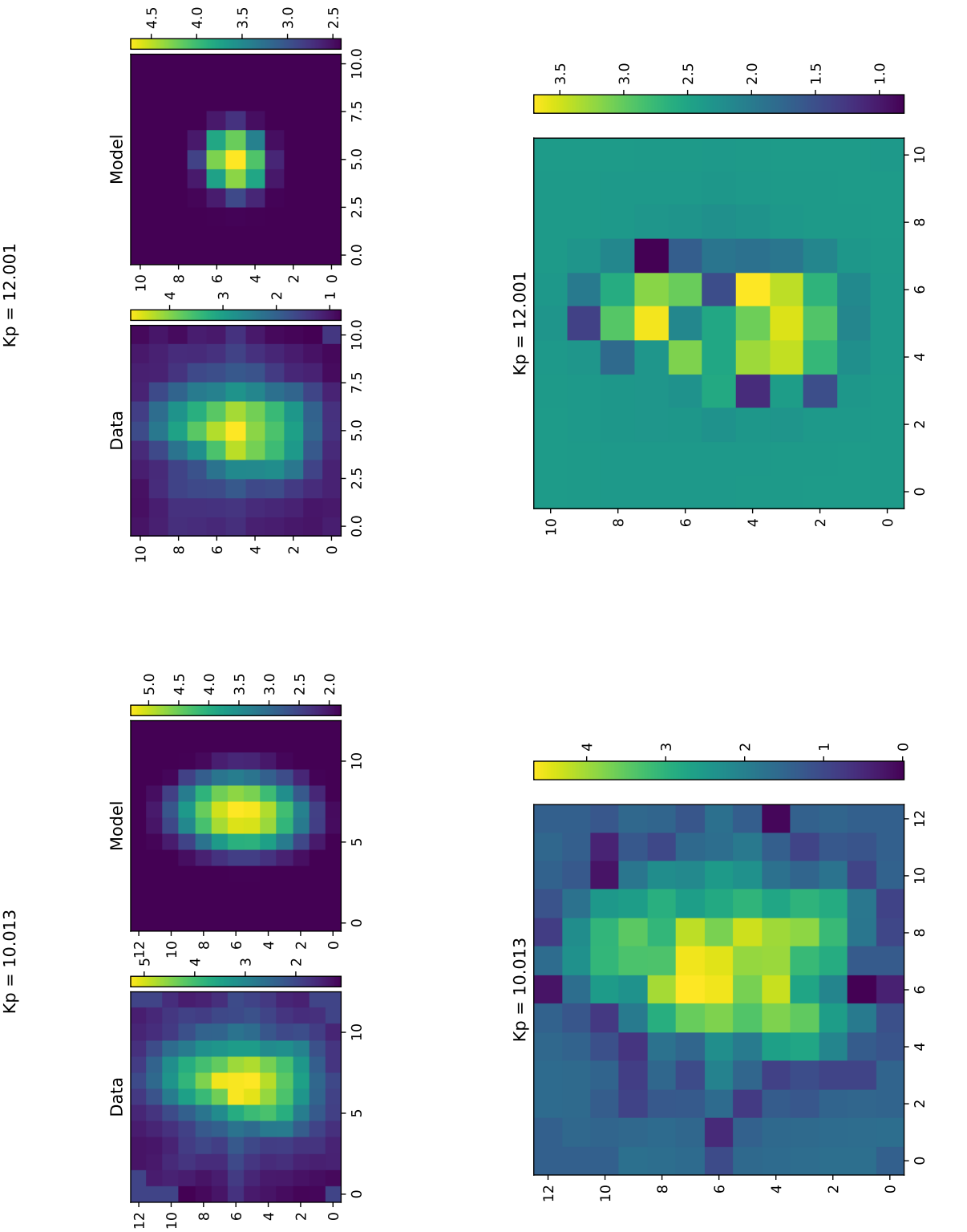

Figure 6.17: Flux maps for data and Gaussian fits (top) and residuals (bottom), in log scale.

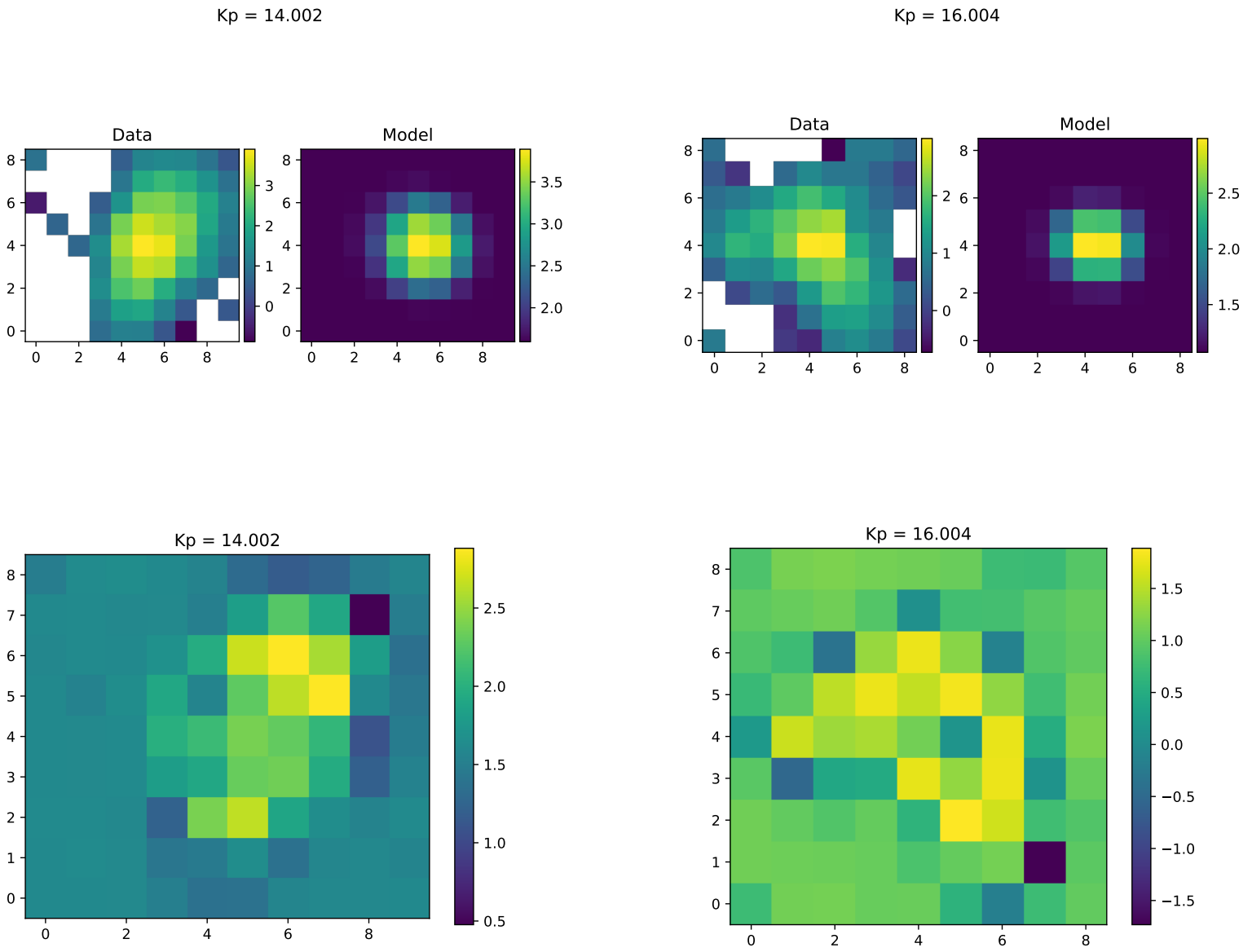

Figure 6.18: Flux maps for data and Gaussian fits (top) and residuals (bottom), in log scale. White pixels are pixels with negative flux and so cannot be expressed in log scale.

Chapter 7

Conclusion

7.1 A Brief Review

We do not detect any planets in the sample of 603 uncontaminated bright targets. This is not a deficiency of *halophot*, but an unfortunate combination of probability and biased sample. We show that injected transits can be consistently retrieved for $R_p/R_\star$ values as small as 0.03 and occasionally for values smaller. If there are any large planets in our remaining sample of 388 contaminated targets, they can be found.

This technique has been proven to be a very effective tool for studying stellar variability, and we show examples of that here with rotationally variable stars and an eclipsing binary. *Halophot* can also be used for variable stars with extremely short periods, such as β Cepheid and δ Scuti stars, but care has to be taken when considering the weights.

7.2 Future Work

There is still a large sample of contaminated bright targets to be studied, as well as many of their field stars. From the combined sample, there may be dozens of new planets waiting to be discovered. Before we can find them, we must continue to work on improving and automating the PSF fitting and removal of

field stars.

We show that a two-dimensional Gaussian is an effective PSF for faint, isolated stars, but it may not be the correct point-spread function for bright field stars or field stars in the halo. As a result, it is necessary to continue working on improving the modelling of the PSF, whether it be with a modified Gaussian or an entirely new model.

We show that this technique can be used to retrieve transit parameters for fainter targets with previously detected exoplanets. The parameters obtained using this technique are in good agreement with the results from the literature. An additional possible branching point of this project could be to run a modified version of *halophot* on fainter targets and search for planets around them.

7.3 Applications to *TESS*

Halophot looks to be a promising tool to use to process the brightest stars that will be observed by *TESS*. *TESS* is designed to observe brighter stars than *K2*, as it saturates at $I_C = 7.5$, compared to *K2*'s saturation limit of V = 11. The bright limit of *TESS* is listed as $I_C = 4$. In addition to being designed for brighter stars than *K2*, it is also designed to look at the nearest M dwarfs by having a bandpass sensitive to longer wavelengths than *Kepler* (Figure 7.1). All of the full frame images will be downloaded at cadences of 30 minutes. Nonetheless, like with *K2*, it can be useful for 2 minute cadences, which will be taken for only a limited number of stars. Similarly, there will be 20 second cadences for approximately 1000 of the brightest stars that will be observed by *TESS*.

In order to examine the possibility of applying *halophot* to *TESS* targets, I look at the target TIC 80466973 (omi02 CMa), a very bright (V = 3.02) B3Ia star.

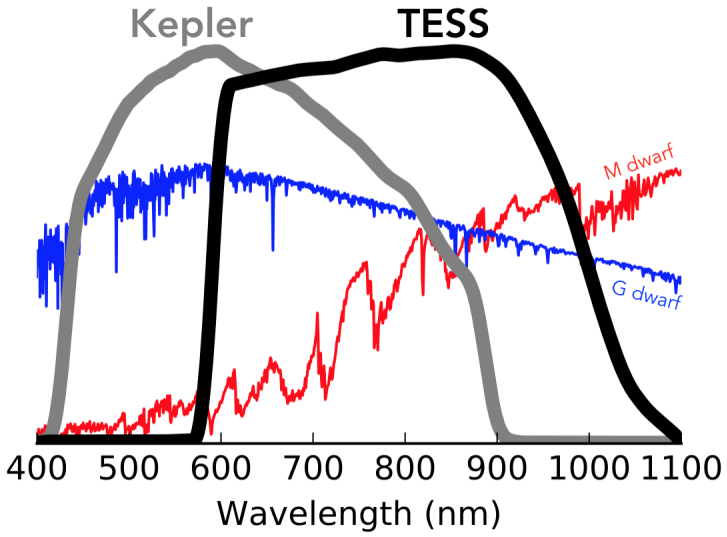

Figure 7.1: Comparison of *Kepler* and *TESS* bandpasses, with model stellar spectra plotted alongside. From `https://heasarc.gsfc.nasa.gov/docs/tess/the-tess-space-telescope.html`

As with most of the bright *K2* targets, the weights are distributed around the halo of the bright target. Additionally, some weights are distributed to contaminating field stars in the field of view (Figure 7.2). Nonetheless, the resulting light curve is very similar to the one generated by the *TESS* team (Figure 7.3).

TESS would provide an unprecedented opportunity to detect exoplanets around bright, later type stars and *halophot* will likely prove to be an invaluable tool. 14,688 targets will be observed with *TESS* magnitude brighter than the saturation limit of 6.5. The sample is similarly biased towards early type and evolved stars (Figure 7.4), but there are still many smaller stars. Of the 14688 with radius values listed, 1816 are smaller than 2 $R_{\odot}$ and 443 of those are 1 $R_{\odot}$ or smaller.

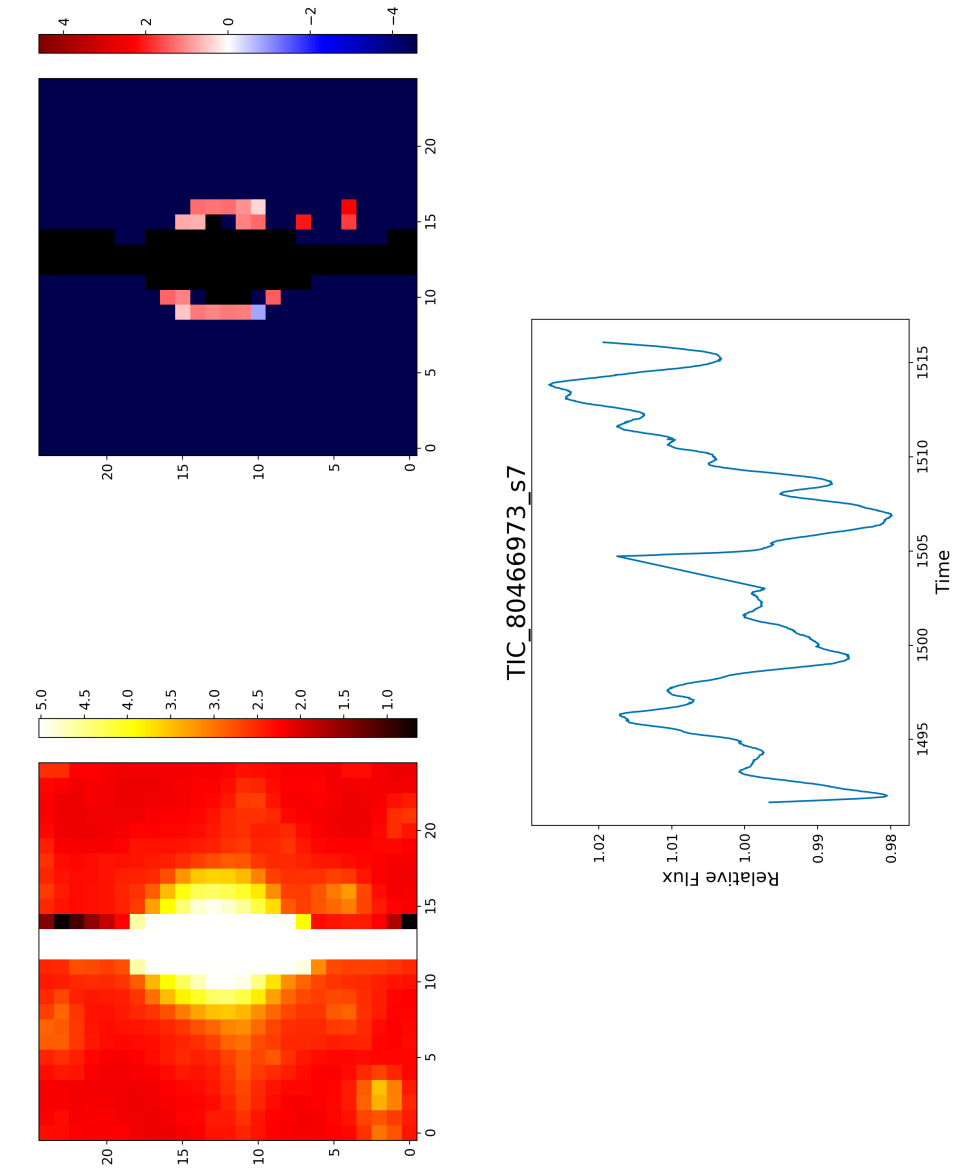

Figure 7.2: *Halophot* results for TIC 80466973

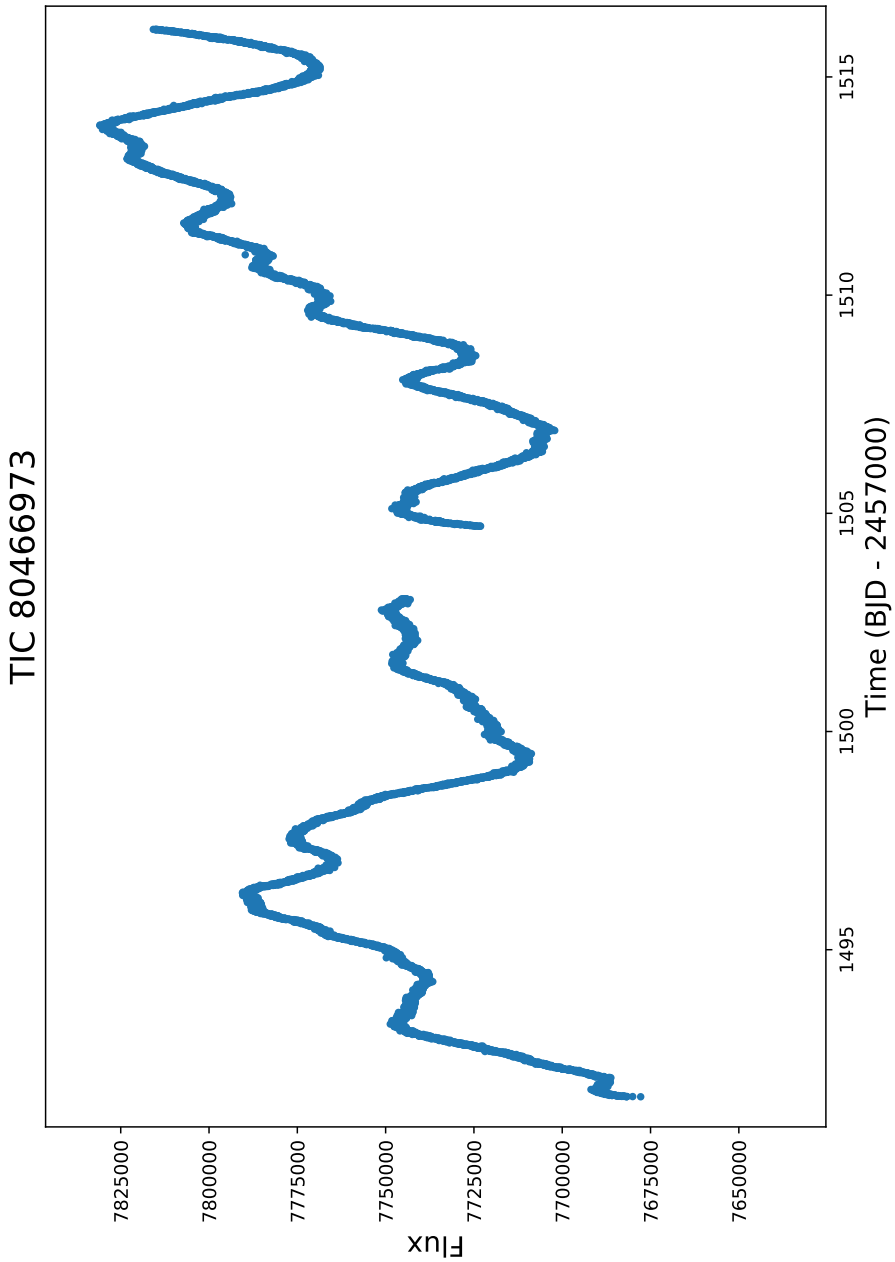

Figure 7.3: Light curve from *TESS*.

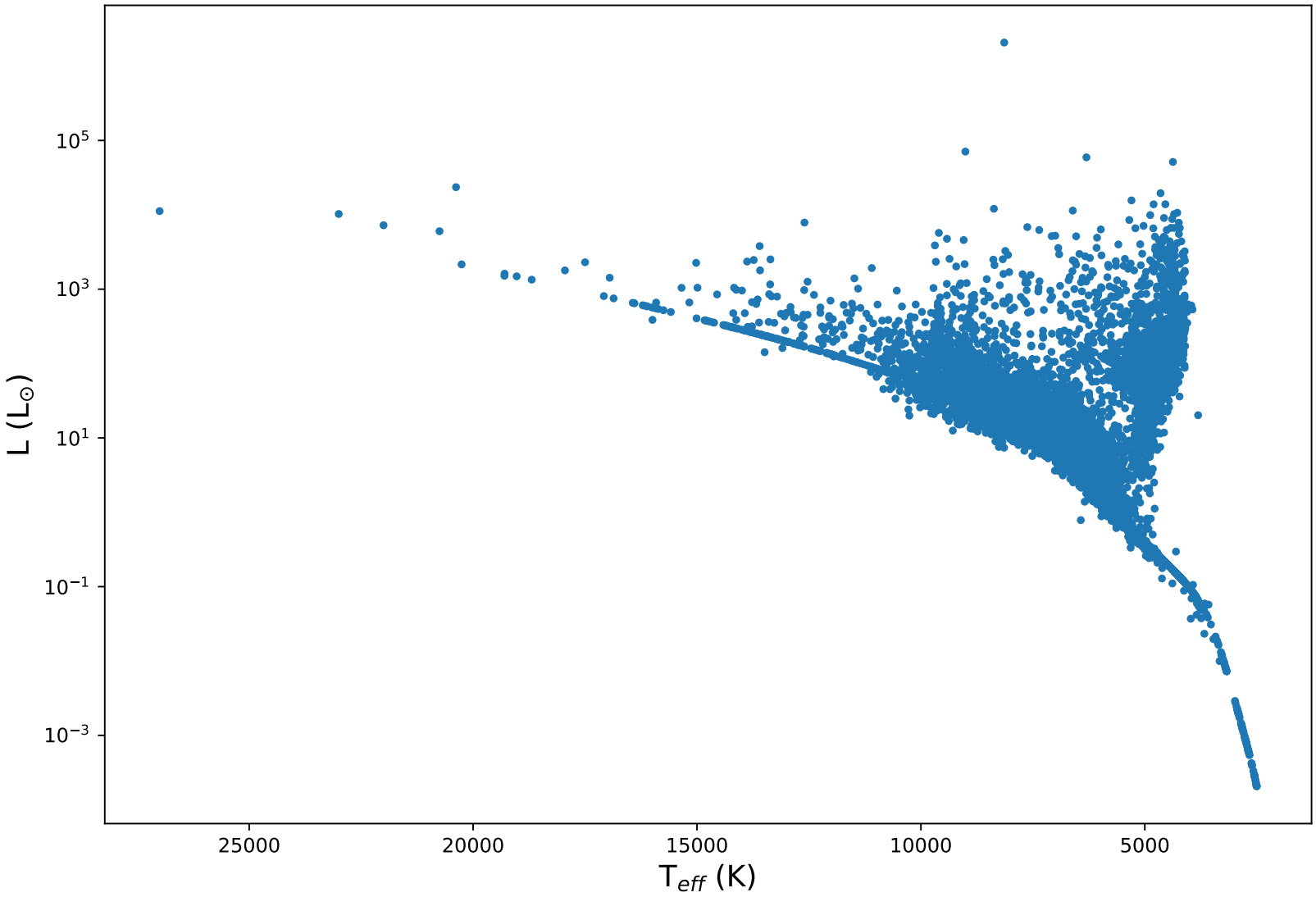

Figure 7.4: HR diagram for *TESS* targets brighter than *TESS* mag 6.5.

Bibliography

Aigrain, S., Parviainen, H., & Pope, B. J. S. 2016, *MNRAS*, 459, 2408.

Akeson, R. L., Chen, X., Ciardi, D., et al. 2013, *PASP*, 125, 989.

Albrecht, S., Winn, J. N., Johnson, J. A., et al. 2012, *ApJ*, 757, 18.

Andersen, J., & Nordstrom, B. 1977, Astronomy and Astrophysics Supplement Series, 29, 309.

Ansdell, M., Gaidos, E., Rappaport, S. A., et al. 2016, *ApJ*, 816, 69.

Aquilecchia, G. "Giordano Bruno" (2019). Encyclopdia Britannica

Arentoft, T., Grundahl, F., White, T. R., et al. 2019, *A&A*, 622, A190.

Armstrong, D. J., Kirk, J., Lam, K. W. F., et al. 2015, *A&A*, 579, A19.

Auvergne, M., Bodin, P., Boisnard, L., et al. 2009, *A&A*, 506, 411.

Bakos, G., Noyes, R. W., Kovács, G., et al. 2004, *PASP*, 116, 266.

Balona, L. A., Baran, A. S., Daszyńska-Daszkiewicz, J., et al. 2015, *MNRAS*, 451, 1445.

Barclay, T., Rowe, J. F., Lissauer, J. J., et al. 2013, *Nature*, 494, 452.

Barragán, O., Grziwa, S., Gandolfi, D., et al. 2016, *AJ*, 152, 193.

Barros, S. C. C., Demangeon, O., & Deleuil, M. 2016, *A&A*, 594, A100.

Boisse, I., Hartman, J. D., Bakos, G. Á., et al. 2013, *A&A*, 558, A86.

Borucki, W. J., Koch, D., Basri, G., et al. 2010, Science, 327, 977.

Brahm, R., Espinoza, N., Rabus, M., et al. 2019, *MNRAS*, 483, 1970.

Breger, M. 2000, Delta Scuti and Related Stars, 3.

Brinkworth, C. S., Burleigh, M. R., Lawrie, K., et al. 2013, *ApJ*, 773, 47.

Brown, T. M., Latham, D. W., Everett, M. E., et al. 2011, *AJ*, 142, 112.

Burke, C. J., McCullough, P. R., Valenti, J. A., et al. 2007, *ApJ*, 671, 2115.

Buysschaert, B., Aerts, C., Bloemen, S., et al. 2015, *MNRAS*, 453, 89.

Campbell, B., Walker, G. A. H., & Yang, S. 1988, *ApJ*, 331, 902.

Carleo, I., Sanna, N., Gratton, R., et al. 2016, Experimental Astronomy, 41, 351.

Charbonneau, D., Brown, T. M., Latham, D. W., et al. 2000, *ApJ*, 529, L45.

Charbonneau, D., Brown, T. M., Noyes, R. W., et al. 2002, *ApJ*, 568, 377.

Charbonneau, D., Allen, L. E., Megeath, S. T., et al. 2005, *ApJ*, 626, 523.

Collier Cameron, A., Guenther, E., Smalley, B., et al. 2010, *MNRAS*, 407, 507.

David, T. J., Hillenbrand, L. A., Gillen, E., et al. 2019, *ApJ*, 872, 161.

Farr, W. M., Pope, B. J. S., Davies, G. R., et al. 2018, *ApJ*, 865, L20.

Foreman-Mackey, D., Hogg, D. W., Lang, D., et al. 2013, Publications of the Astronomical Society of the Pacific, 125, 306.

Fressin, F., Torres, G., Charbonneau, D., et al. 2013, *ApJ*, 766, 81.

Gaia Collaboration, Prusti, T., de Bruijne, J. H. J., et al. 2016, *A&A*, 595, A1.

Gaia Collaboration, Brown, A. G. A., Vallenari, A., et al. 2018, *A&A*, 616, A1.

Gandolfi, D., Barragán, O., Livingston, J. H., et al. 2018, *A&A*, 619, L10.

Gatewood, G., & Eichhorn, H. 1973, *AJ*, 78, 769.

Gaudi, B. S., & Winn, J. N. 2007, *ApJ*, 655, 550.

Gaudi, B. S., Stassun, K. G., Collins, K. A., et al. 2017, *Nature*, 546, 514.

Gilliland, R. L., Jenkins, J. M., Borucki, W. J., et al. 2010, *ApJ*, 713, L160.

Grunblatt, S. K., Huber, D., Gaidos, E. J., et al. 2016, *AJ*, 152, 185.

Grunblatt, S. K., Huber, D., Gaidos, E., et al. 2017, *AJ*, 154, 254.

Hartman, J. D., Bakos, G. Á., Torres, G., et al. 2011, *ApJ*, 742, 59.

Hatzes, A. P., Cochran, W. D., Endl, M., et al. 2003, *ApJ*, 599, 1383.

Hellier, C., Anderson, D. R., Collier Cameron, A., et al. 2012, *MNRAS*, 426, 739.

Hermes, J. J., Gänsicke, B. T., Gentile Fusillo, N. P., et al. 2017, *MNRAS*, 468, 1946.

Hill, G. 1967, The Astrophysical Journal Supplement Series, 14, 263.

Huber, D., Silva Aguirre, V., Matthews, J. M., et al. 2014, The Astrophysical Journal Supplement Series, 211, 2.

Huber, D., Bryson, S. T., Haas, M. R., et al. 2016, The Astrophysical Journal Supplement Series, 224, 2.

Jensen, A. G., Redfield, S., Endl, M., et al. 2012, *ApJ*, 751, 86.

Johnson, J. A., Aller, K. M., Howard, A. W., et al. 2010, Publications of the Astronomical Society of the Pacific, 122, 905.

Johnson, M. C., Dai, F., Justesen, A. B., et al. 2018, *MNRAS*, 481, 596.

Jones, M. I., Brahm, R., Espinoza, N., et al. 2018, *A&A*, 613, A76.

Kempton, E. M.-R., Bean, J. L., Louie, D. R., et al. 2018, Publications of the Astronomical Society of the Pacific, 130, 114401.

Kerschbaum, F., & Maitzen, H. M. 1991, *A&A*, 246, 346.

Koch, D. G., Borucki, W. J., Basri, G., et al. 2010, *ApJ*, 713, L79.

Kovács, G., Zucker, S., & Mazeh, T. 2002, *A&A*, 391, 369.

Kreidberg, L., Bean, J. L., Désert, J.-M., et al. 2014, *Nature*, 505, 69.

Kreidberg, L. 2015, Publications of the Astronomical Society of the Pacific, 127, 1161.

Kreidl, T. J., & Schneider, H. 1989, Information Bulletin on Variable Stars, 3282, 1.

Léger, A., Rouan, D., Schneider, J., et al. 2009, *A&A*, 506, 287.

Léger, A., Grasset, O., Fegley, B., et al. 2011, *ICAR*, 213, 1.

Libralato, M., Bedin, L. R., Nardiello, D., et al. 2016, *MNRAS*, 456, 1137.

Libralato, M., Nardiello, D., Bedin, L. R., et al. 2016, *MNRAS*, 463, 1780.

Linsky, J. L., Yang, H., France, K., et al. 2010, *ApJ*, 717, 1291.

Lomb, N. R. 1978, *MNRAS*, 185, 325.

Luger, R., Agol, E., Kruse, E., et al. 2016, *AJ*, 152, 100.

Luger, R., Kruse, E., Foreman-Mackey, D., et al. 2018, *AJ*, 156, 99.

Lund, M. B., Rodriguez, J. E., Zhou, G., et al. 2017, *AJ*, 154, 194.

Madsen, S., Dravins, D., & Lindegren, L. 2002, *A&A*, 381, 446.

Mandel, K., & Agol, E. 2002, *ApJ*, 580, L171.

Marois, C., Macintosh, B., Barman, T., et al. 2008, Science, 322, 1348.

Maxted, P. F. L., & Hutcheon, R. J. 2018, *A&A*, 616, A38.

Mayor, M., & Queloz, D. 1995, *Nature*, 378, 355.

Molnár, L., Pál, A., Plachy, E., et al. 2015, *ApJ*, 812, 2.

Moskalik, P., & Dziembowski, W. A. 1992, *A&A*, 256, L5.

Moutou, C., Deleuil, M., Guillot, T., et al. 2013, *ICAR*, 226, 1625.

Mulders, G. D., Pascucci, I., & Apai, D. 2015, *ApJ*, 798, 112.

Muthsam, H., & Stepien, K. 1980, *A&A*, 86, 240.

Nardiello, D., Libralato, M., Bedin, L. R., et al. 2016, *MNRAS*, 463, 1831.

Niraula, P., Redfield, S., Dai, F., et al. 2017, *AJ*, 154, 266.

Niraula, P. "Planet Hunting and Characterization with K2" (2018). Masters Theses, Wesleyan University 201.

Paunzen, E., Hümmerich, S., Bernhard, K., et al. 2017, *MNRAS*, 468, 2017.

Pepper, J., Pogge, R. W., DePoy, D. L., et al. 2007, Publications of the Astronomical Society of the Pacific, 119, 923.

Plavchan, P., Latham, D., Gaudi, S., et al. 2015, arXiv e-prints , arXiv:1503.01770.

Pope, B. J. S., White, T. R., Huber, D., et al. 2016, *MNRAS*, 455, L36.

Rakos, K. D. 1962, Lowell Observatory Bulletin, 5, 227.

Rebull, L. M., Stauffer, J. R., Hillenbrand, L. A., et al. 2017, *ApJ*, 839, 92.

Rebull, L. M., Stauffer, J. R., Cody, A. M., et al. 2018, *AJ*, 155, 196.

Ribas, I., Tuomi, M., Reiners, A., et al. 2018, *Nature*, 563, 365.

Ricker, G. R., Winn, J. N., Vanderspek, R., et al. 2014, Space Telescopes and Instrumentation 2014: Optical, Infrared, and Millimeter Wave, 914320.

Rizzuto, A. C., Mann, A. W., Vanderburg, A., et al. 2017, *AJ*, 154, 224.

Rodriguez, J. E., Zhou, G., Vanderburg, A., et al. 2017, *AJ*, 153, 256.

Samus', N. N., Kazarovets, E. V., Durlevich, O. V., et al. 2017, Astronomy Reports, 61, 80.

Shobbrook, R. R., Herbison-Evans, D., Johnston, I. D., et al. 1969, *MNRAS*, 145, 131.

Sing, D. K. 2010, *A&A*, 510, A21.

Struve, O. 1952, The Observatory, 72, 199.

Swain, M. R., Vasisht, G., & Tinetti, G. 2008, *Nature*, 452, 329.

Tinetti, G., Vidal-Madjar, A., Liang, M.-C., et al. 2007, *Nature*, 448, 169.

Udry, S., & Santos, N. C. 2007, *ARA&A*, 45, 397.

Uytterhoeven, K., Moya, A., Grigahcène, A., et al. 2011, *A&A*, 534, A125.

Van Cleve, J. E., Howell, S. B., Smith, J. C., et al. 2016, Publications of the Astronomical Society of the Pacific, 128, 75002.

van de Kamp, P. 1963, *AJ*, 68, 515.

Van Eylen, V., Nowak, G., Albrecht, S., et al. 2016, *ApJ*, 820, 56.

van Genderen, A. M. 1971, *A&A*, 14, 48.

van Hoof, A. 1957, *PASP*, 69, 179.

Vanderburg, A., & Johnson, J. A. 2014, Publications of the Astronomical Society of the Pacific, 126, 948.

Vanderburg, A., Latham, D. W., Buchhave, L. A., et al. 2016, The Astrophysical Journal Supplement Series, 222, 14.

Vidal-Madjar, A., Lecavelier des Etangs, A., Désert, J.-M., et al. 2003, *Nature*, 422, 143.

White, T. R., Pope, B. J. S., Antoci, V., et al. 2017, *MNRAS*, 471, 2882.

Winn, J. N. 2010, Exoplanets, 55.

Winn, J. N., Matthews, J. M., Dawson, R. I., et al. 2011, *ApJ*, 737, L18.

Wolszczan, A., & Frail, D. A. 1992, *Nature*, 355, 145.

Wraight, K. T., White, G. J., Bewsher, D., et al. 2011, *MNRAS*, 416, 2477.